PONTIFICIA UNIVERSIDAD CATOLICA DE CHILE
ESCUELA DE INGENIERIA

ROLE OF THE SUBDUCTION CHANNEL IN THE EMPLACEMENT OF ULTRAMAFIC BODIES WITHIN ACCRETIONARY PRISMS: CASE STUDY IN LA CABAÑA MASSIF

JORGE SANHUEZA SOTO

Thesis submitted to the Office of Research and Graduate Studies in partial fulfillment of the requirements for the Degree of Master of Science in Engineering

Advisor:
GONZALO YÁÑEZ C.

Santiago de Chile, (October, 2019)

PONTIFICIA UNIVERSIDAD CATOLICA DE CHILE
ESCUELA DE INGENIERIA

ROLE OF THE SUBDUCTION CHANNEL IN THE EMPLACEMENT OF ULTRAMAFIC BODIES WITHIN ACCRETIONARY PRISMS: CASE STUDY IN LA CABAÑA MASSIF

JORGE SANHUEZA SOTO

Members of the Committee:

GONZALO YÁÑEZ C.

ESTEBAN SÁEZ R.

CARLOS MARQUADT R.

FERNANDO BARRA P.

DOMINGO MERY Q.

Thesis submitted to the Office of Research and Graduate Studies in partial fulfillment of the requirements for the Degree of Master of Science in Engineering

Santiago de Chile, (October, 2019)

"*To succeed, planning alone is insufficient. One must improvise as well"*

Isaac Asimov

ACKNOWLEDGMENTS

First, I want to thank my family: my mom, my dad and my brother. You have given me a lot of things during my life and I am sure you will still be doing it; however, the most important things are given daily: your presence and unconditional love and support. You taught me how to walk but now I am going to fly. Never forget that I love you all.

To my advisor, Gonzalo, who always knew I could achieve this goal from the beginning, even when I did not. I finished this thesis because I saw my very same motivation in you. Moreover, but not least, even when you were far, I never felt alone doing this research. Thank you for teaching me how to think as a geoscientist and also developing my human skills, which is equally important in my opinion.

Thanks to the members of the committee, for further improving the quality of this research by their constructive feedback. Also, to Jaime Araya and Giovani Menanno for contributing my path through the world of geophysics.

To the aquatic world of "*la pecera*" and their associates: Sebastián, José, Pablo, Sofía, Juan Pablo, Ramón, Rocío, Javiera and Ronny. I am certain that I could have finished my thesis way before (a couple of semesters to be honest). But all the coffee breaks, desserts (Worms & Age), beers and miscellaneous conversations were all worth it.

To my lifetime friends, Heinz, Claudio and Sebastián, for all the years passed by and the coming ones. This friendship transcended time and distance.

I am grateful to the Canarios family in Carahue, who did not doubt to help us in difficult situations during field campaigns. Also, to their positive attitude to contribute to this work.

I want to thank the "Núcleo Milenio Trazadores de Metales" for the funding of this thesis and field campaigns. Also, GFDas SpA and DICTUC for providing the drones and equipments.

Big shout-out to the music, vital part of my life. Especially the bands/artist who provided a nice atmosphere: Radiohead, 2Pac, Soundgarden, Nujabes, Björk, Frank Sinatra, REM, Nirvana, Queen, Herbie Hancock and György Ligeti.

All the work presented here is dedicated in memory of Ida Cárcamo Soto and José Tomás Camacho, people only die when they are forgotten.

GENERAL INDEX

Page

LIST OF TABLES

Page

LIST OF FIGURES

Page

RESUMEN

El emplazamiento de rocas ultramáficas en prismas de acreción plantea problemas geodinámicos principalmente por tener fuerzas de flotabilidad negativa. El objetivo de esta tesis es investigar escenarios tectónicos favorables para responder a la geología observada, para esto se utiliza el concepto de flujo de retorno generado en el canal de subducción. Las simulaciones numéricas realizadas fueron acotadas con las evidencias en el sector de La Cabaña. Esta área de estudio está ubicada en la Cordillera de la Costa de la parte centro-sur de Chile, en donde numerosas ocurrencias de cuerpos ultramáficos y serpentinitas se han identificado dentro del prisma de acreción. Sin embargo, pocos estudios han sido realizados en torno a la petrofísica y el tamaño de los cuerpos ultramáficos. Debido a esto, para la estimación del tamaño se utiliza el método geofísico magnético, además de tomografías eléctricas de resistividad para complementar mapeos en detalle. Los resultados de la inversión muestran un cuerpo elongado de 3 km de largo y 1.5 km de ancho, alcanzando profundidades de 1.5 km. Con esta estimación de tamaño, las simulaciones numéricas realizadas permiten probar diversos escenarios tectónicos. Estas variaciones corresponden al cambio del ángulo y velocidad de subducción y la geometría del canal de subducción. Los resultados obtenidos muestran rápidas tasas de ascenso tan altas como el 40% de la velocidad de convergencia para las condiciones más favorables (alto ángulo de subducción y un canal de subducción ancho). Bajas tasas de exhumación o incluso estancamiento en el fondo del canal de subducción se produjeron en los casos opuestos. Finalmente, las modelaciones numéricas pudieron replicar las observaciones petrofísicas en La Cabaña y además el tamaño mapeado, por lo que se puede inferir un escenario tectónico para el emplazamiento. Bajo esta lógica, el tamaño de las rocas ultramáficas en prismas de acreción puede ser usado como un indicador de una configuración tectónica que favorece su ascenso.

Palabras Claves: canal de subducción, exhumación, rocas ultramáficas, prospecciones geofísicas

ABSTRACT

The emplacement of ultramafic bodies outcropping at accretionary prisms pose geodynamic problems due to their negative buoyancy force. The scope of this research is to explore plausible scenarios to explain these geological observations using the concept of the return flow generated in the subduction channel. Our simulations were constrained with the evidences in La Cabaña area, located in the Coastal Cordillera of south-central Chile, that record several ultramafic bodies, serpentinites and mica schist host rocks within the accretionary prism. However, there were scarce studies regarding the size and petrophysics of ultramafic bodies and country rocks. To estimate the size and depth of the ultramafic bodies, we deployed geophysical campaigns of magnetic airborne surveys via unmanned aerial vehicles (UAV) and electric resistivity tomography (ERT) to complement detailed mapping. Inversion results showed a horizontal elongated body of 3 km and 1.5 km in the NS and EW respectively and a depth extent of 1.5 km. Magnetic susceptibility in the inversions were performed considering our in-situ measurements of the different domains in La Cabaña. Using this size constrain in our simulations, we tested several tectonic scenarios, varying the subduction angle dip and velocity and the subduction channel geometry. Model results obtained showed fast exhumation rates as high as 40% of the convergence velocity for favorable conditions (steep subduction angle and wide subduction channel) and slow rates or even stagnation at the bottom of the subduction channel for the opposite cases. Finally, our simulations accounted several petrophysical observations in La Cabaña and the size observed, suggesting a specific tectonic scenario for the emplacement. In this manner, the size of ultramafic rocks within accretionary prism can be used as an indicator of the tectonic configuration in the emplacement.

Keywords: subduction channel, exhumation, ultramafic rocks, geophysical surveys.

1. INTRODUCTION

1.1 Geological Context

Plate tectonics theory represents the outer shell of the Earth as a finite number of rigid plates, which are floating over the asthenosphere. These rigid plates are continually created and consumed. At spreading ridges, two plates diverge from each other in a process known as seafloor spreading. In contrast, there is a place where two plates collide each other, which are the ocean trenches. Generally, ocean plates such as the Nazca Plate, bend and descend into the interior of the Earth in a process known as subduction. Such a process is driven by density contrast between the colliding plates (Turcotte and Schubert, 2014). A cross section illustrating both processes is shown in Figure 1-1. Where the lithosphere is composed by the plate tectonics and part of the upper mantle, which are cold and rigid and do not deform significantly. On the other hand, the rocks beneath this domain are sufficiently hot to behave as fluid for plate tectonic strain-rates; this domain is denoted as the asthenosphere. As a whole, plate divergence at spreading ridges and convergence at subduction zones are commonly denominated the Wilson-Cycle (Turcotte and Schubert, 2014).

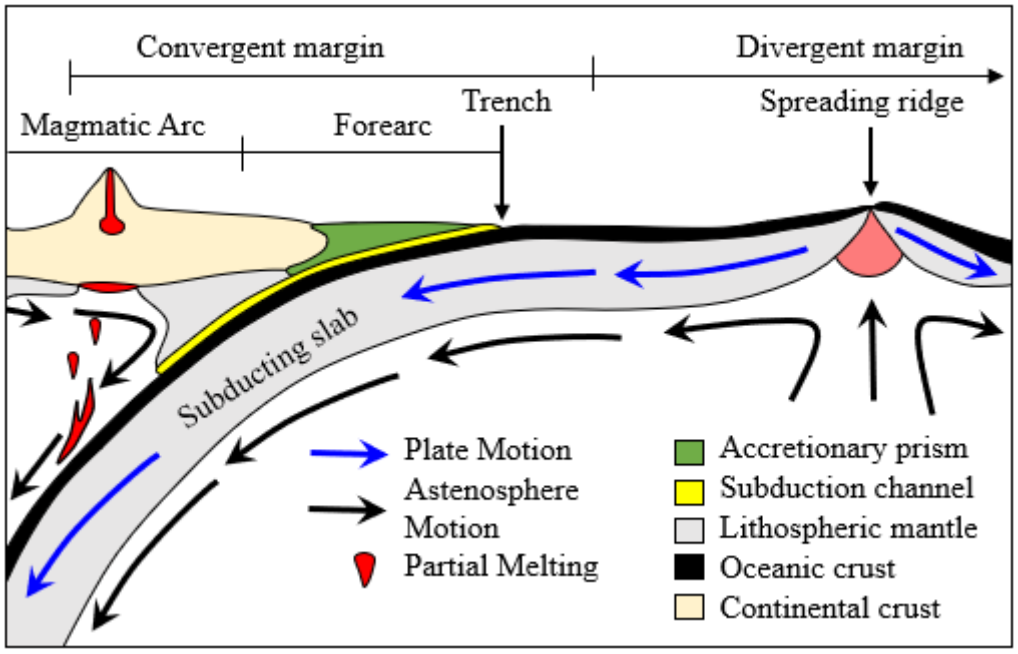

Figure 1-1: Schematic section of a subduction zone and their processes and a spreading ridge. White color in the background beneath the plates represent the asthenosphere. Arrows indicate motion of the plate and the asthenosphere (Modified from Stern, 2002).

Within this general tectonic context, the focus of this thesis involves subduction zones environment. First order geomorphological elements at subduction zone include a magmatic arc and a forearc region (Figure 1-1). The first one is characterized by a chain of volcanoes on top of the overriding plate, at a distance of ~ 100-200 km from the trench. The origin of these volcanoes is linked to the rise of magma through partial melting of the subducting slab due to dehydration processes (e.g. Stern, 2002). This magmatism may contribute to volcanism and/or become stalled at depth as plutonic bodies (e.g. Schubert, 2015).

The second one, the forearc, is located between the magmatic arc and the trench. Mainly composed by continental crust, the accretionary prism, and the concept of

subduction channel (Figure 1-1). The work developed in this thesis is within this domain, so further details of each will be explained in the next section in order to gain some insights on the processes involved.

1.1.1 Accretionary prism

The accretionary prism at the forearc region, is built by the addition and imbrication of sediments from the trench region. This process depends on the sediment supply in the area, which can be derived from the erosion of the continental crust and/or oceanic sediments. High sediment supply grows thick forearc regions by frontal accretion, as sediment is "bulldozed" against the continent to form the accretionary prism or wedge, growing in the trench direction (Stern, 2002). Nevertheless, the accretionary prism can also grow by basal accretion of subducted sediments coming from the subduction channel (Cloos and Shreve, 1988; Stern, 2002). In this case, the accretionary prism thickens from below. Figure 1-2 illustrate both processes.

1.1.2 Ultramafic rocks within accretionary prisms

The accretionary prism is mainly composed by meta-sedimentary rocks that undergo high pressure processes (frontal and basal accretion). Moreover, the temperatures recorded in this region are typically < 600°C (Davies and Stevenson, 1992) which are related to low heat flow (25 – 50 mWm^{-2}; Peacock, 1996). Both, high pressure and low temperature are recorded in the metamorphic peak conditions of the meta-sedimentary rocks comprising the accretionary prism.

However, several accretionary prisms also record the occurrence of ultramafic rocks, which are composed by dense ferromagnesian minerals associated to the shallow mantle (Anderson, 1989) and share the same pressure and temperature conditions of the meta-sedimentary rocks (Ernst, 2006). These occurrences are the geological evidences of the exhumation of ultramafic rocks with a deep origin and later uplifted to surface levels. In addition, only 50% of the incoming sediments go into the prism-forming process, the remaining 50% bypasses these processes and is subducted to deeper levels (von Huene and Scholl, 1991). The mechanism to explain the growing of the accretionary prism, sediment subduction and exhumation of ultramafic rocks is provided by the concept of the subduction channel, described in the next section, which is located between the subducted slab and the continental block (Figure 1-1 and 1-2).

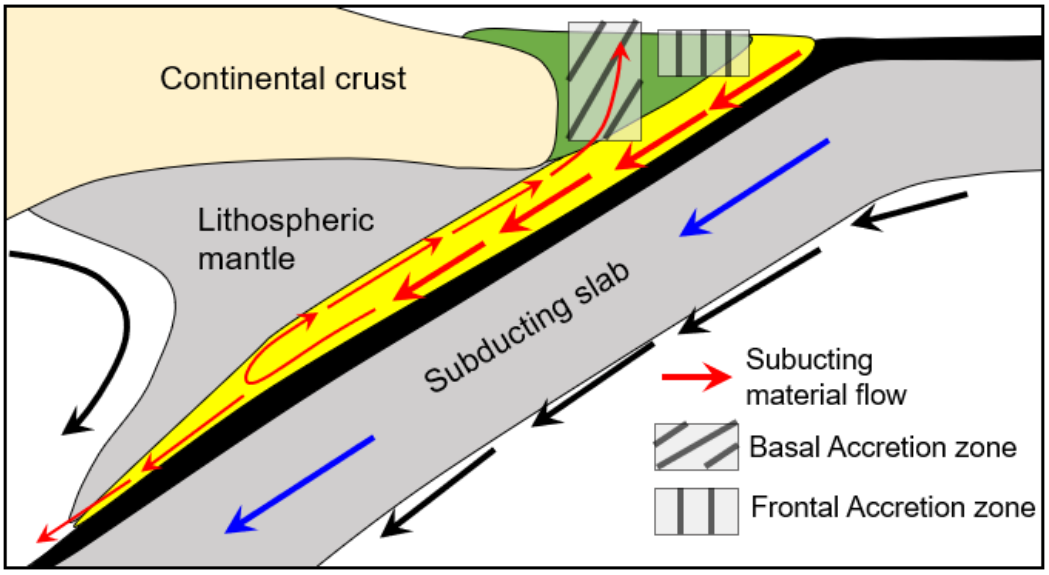

Figure 1-2: Schematic section of the forearc region between an oceanic subducting slab and a continental plate. Color are the same used in Figure 1-1. (Modified from Cloos and Shreve, 1988; Stern, 2002).

1.1.3 Subduction channel concept

This concept was introduced by Cloos and Shreve (1988), to explain the following observations: (a) the presence of sedimentary components in the geochemical signature of several magmatic arcs (Hole et al., 1984; Myers et al., 1986); (b) the exhumation from great depths (~ 100 km) to surface levels of kilometers-size blocks (Shreve and Cloos, 1986); and (c), the presence of ultramafic rocks within accretionary prisms (Agard et al., 2008; Guillot et al., 2009). These observations allowed to confirm two processes: (1) the great burial of subducting sediments which are recorded in several magmatic arcs and (2) the return flow that provide a driving mechanism for the emplacement of high pressure and ultrahigh pressure metamorphic and ultramafic rocks. Both processes are illustrated in Figure 1-2.

Even though the subduction channel concept has been tested from different perspectives in the last decades (direct and indirect observations, analytically, and modelling; Cloos and Shreve (1988), Gerya et al., (2002)), several questions regarding this uplifting mechanism are still unsolved. In specific: how subduction channel geometry and plate kinematics affect the return flow strength? And how this can be related to the size of the ultramafic rocks in surface levels? In this thesis, the effort is focused to constrain these parameters through direct and indirect observations and numerical simulations.

1.2 Statement of the problem

Metamorphic rocks, including ultramafic rocks, affected by high pressure and ultrahigh-pressure processes have been recorded in accretionary prisms (e.g. Ernst et al., 1999; Ernst, 2006). These authors propose that the origin of these rocks was initially within shallow levels (< 10 km), where they were subducted into great depths (50 - 100 km) due to subduction processes. Finally, they were exhumed and emplaced into the accretionary prism into shallow levels again (< 10 km or even the surface).

The main geodynamic problem is that the emplacement of dense ultramafic rocks cannot rely on buoyancy, thus, an additional mechanism must override the negative buoyancy force to uplift them. In this research, we explore a likely mechanism of emplacement considering the concept of subduction channel developed originally by Shreve and Cloos (1986).

1.3 Objectives

The primary aim of this thesis is to determine favorable tectonic and petrophysics scenarios to allow the development of a return flow within the subducting channel flow strong enough to ensure the upwelling of ultramafic rocks in accretionary prisms.

The secondary objective is to determine the critical conditions, size, shape, orientation, by which uplifted ultramafic bodies can reach the surface throughout the subduction channel.

1.4 Hypothesis

The exhumation of ultramafic bodies into shallow levels is controlled by the geometry of the subduction channel and plate kinematics. Where the return flow strength that allows the upwelling, is primarily controlled by the width of the subduction channel and the down going slab dip and velocity. The subduction channel width also controls the maximum size of the ultramafic rocks exhumed through this mechanism.

1.5 Methodology

In order to understand how the return flow in the subduction channel works, a combined methodology of geology, geophysics and numerical modelling is proposed. The accretionary prism of south-central Chile records several ultramafic bodies (Hervé 1988; Barra et al., 1998), which provide a natural laboratory setup to study the subduction channel. In particular, a case study of La Cabaña is used.

However, the size of these bodies remains unknown due to the development of a dense rainforest in the area, where the best approach is using indirect geophysical methods to perform this task. Finally, with the geology and geophysical constrains, numerical simulations allow us to build realistic tectonic scenarios to study the return flow in the subduction channel. Details of the geological context, geophysical tools, and numerical approach is described in the following subsections.

1.5.1 Geological framework

The south-central part of Chile is composed by two metamorphic belts: The Western Series and the Eastern Series. These are part of the Coastal Cordillera along with a basement composed by granitoids (Hervé 1988). Both metamorphic belts comprise the paleo-accretionary prism formed during Late Paleozoic times (Aguirre et al., 1972; Figure 1.3). At that time this margin was settled within the Pacific margin of Gondwana where subduction zone processes are inferred (frontal and basal accretion).

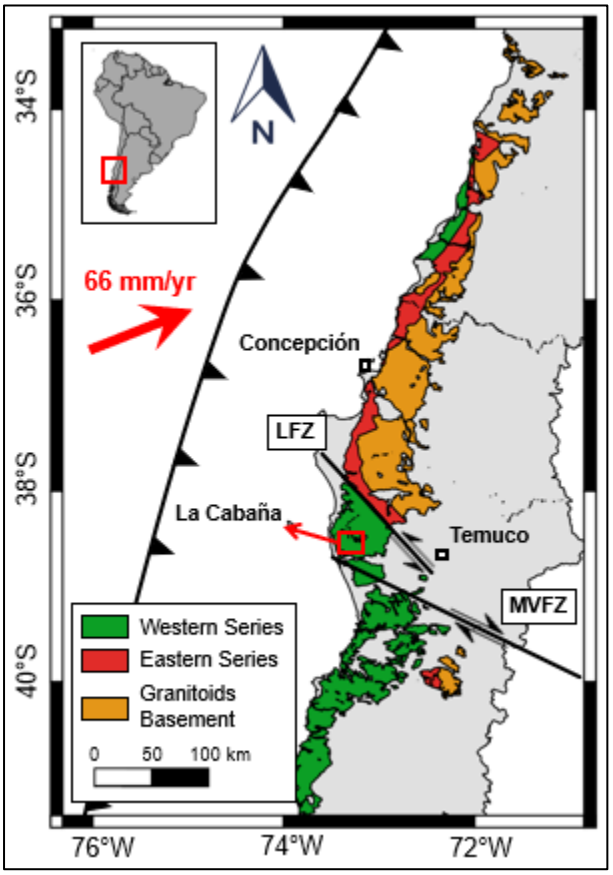

Figure 1-3: Major geological units of Coastal Cordillera at south-central Chile (modified from SERNAGEOMIN, 2003). Geological faults: Lanalhue Fault Zone (LFZ; Glodny et al., 2008), Mocha-Villarrica Fault Zone (MVFZ; Melnick and Echtler, 2006). Convergence velocity vector by Angermann et al. (1999).

The metamorphic belts suffered different processes: The Eastern Series, composed by metasedimentary rocks, was affected by high-temperature and low-pressure metamorphism associated with frontal accretion processes during the development of the accretionary prism (González-Bonorino 1971; Willner, 2005). In contrast, the Western Series, composed by micaceus schist of continental origin, metabasites (metagabbros and metavolcanic rocks) and highly serpentinized ultramafic rocks

scattered along this unit (Hervé 1988; Barra et al., 1998; González-Jiménez et al., 2014). The exhumation of the Western Series is associated to basal accretion processes (Willner, 2005, Glodny et al., 2005), where high pressures and low temperatures were achieved (7 – 9.3 kbar and 380°-400°C; González-Jiménez et al., 2016).

Our case study is within the Western Series in La Cabaña area, which is located 60 km northwest of the city of Temuco (Figure 1-4). Several ultramafic bodies have been identified and are the largest known cromitites bodies in the paleo-accretionary complex of the southern Coastal Cordillera (Barra et al., 1998; Höfer et al., 2001).

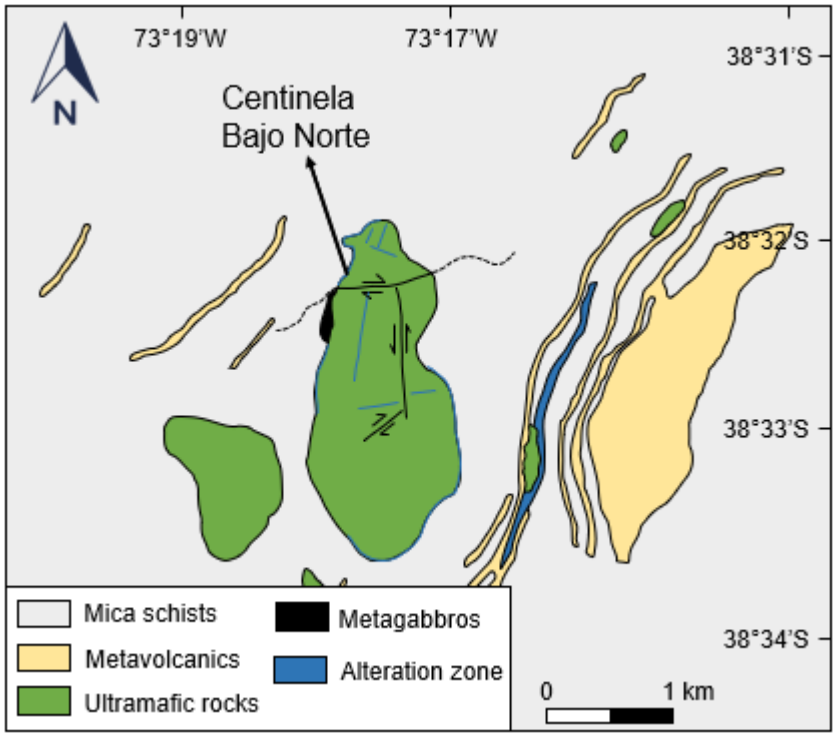

Figure 1-4: Local geological map in La Cabaña (modified from Höfer et al., 2001; Romero et al., 2017)

The recorded ultramafic rocks within the Western Series experienced slightly similar conditions, where higher pressure processes were achieved (between 1.6 and 3.2 GPa and ~ 400°C; González-Jiménez et al., 2016). However, some serpentinites could have formed deeper with the highest pressures in the Western Series (450°C < T < 650°C and 15 kbar < P < 26 kbar; Plissart et al., 2019). These observations suggest an already cooled subduction system and that the La Cabaña ultramafic bodies represent the uppermost part of the mantle corner before being captured by the subduction channel (Plissart et al., 2019).

1.5.2 Geophysical surveys

To acknowledge the size and depth extent of the ultramafic bodies in La Cabaña, geophysical methods are the best approach since a dense forest is present, preventing direct geological mapping. Moreover, the ultramafic rocks located at the study area have optimum petrological properties (magnetic susceptibility and resistivity) to estimate without ambiguity the size and emplacement geometry of La Cabaña ultramafic bodies within the metasedimentary rocks.

1.5.2.1 Magnetic survey and inversion

The equipment used in this survey were a three-axis fluxgate magnetometer (Bartington Mag-03 Three-axis) installed in the UAV and a vapor cesium magnetometer for the base station (Geometrics 858).

The airborne magnetic survey was deployed over La Cabaña ultramafic bodies (red frame in Figure 1-4). The whole survey covered 91 km of magnetic profile data

through EW flight lines spaced ~200m apart. For safety purposes, the flights were done along flat barometric altitudes of 768m and 853m which caused a topographic distortion of the data because every point had a variable distance relative to the magnetic source.

For further understanding this geophysical method, Appendix A gives a theorical outline and explains the magnetic anomalies within the Earth and how the distance relative to the magnetic source affect the signal. The rough topography of the study area requires a data correction to equalize the source-observation distance. In order to perform that task I develop a continuation algorithm, described in detail in Appendix B.

After the data correction, the 3D inversion was performed using the code from the University of British Columbia-Geophysical Inversion Facility's (UBC-GIF) Mag3D (Li and Oldenburg, 1996). This let us to estimate the size of the biggest ultramafic body in La Cabaña. Inversion results are shown in chapter 2 and in Appendix A.3.

1.5.2.2 Electric resistivity tomography (ERT) survey and inversion

The instrument used for ERT data acquisition was the ABEM Terrameter LS2 with 48 electrode arrays and 20 m dipole spacing. Every data point was measured 4 times to improve data quality and a threshold of 10% standard deviation was set to reduce noisy data. We used a dipole-dipole configuration, since this array is the most effective for vertical structures with good horizontal and depth coverage (Sharma and Verma, 2015).

A complete theory of this geophysical method and the implementation during fieldwork is outlined in Appendix C.

For the 2D inversion, the software ZondRes2D was used and a sensibility analysis was also done to ensure that the inversion is generated by geological sources (see Appendix C.4). This inversion allowed a detailed mapping of the geological units in La Cabaña, which are also related to the magnetic inversion.

The inversion results are displayed Chapter 2 (paper section). Meanwhile, in Appendix A.2 and C.4 supplementary inversion results are shown with the inversion procedure for both geophysical methods.

1.5.3 Numerical modelling

1.5.3.1 Main equations

The main physics equations used to represent the return flow in the subduction channel are the Stokes equations of motion.

$$\nabla^2(\eta \boldsymbol{u}) - \nabla p + \rho \boldsymbol{g} = 0$$

$$\nabla \cdot (\rho \boldsymbol{u}) = 0$$

where $\boldsymbol{u}$ is the velocity vector in $m \cdot s^{-1}$, p the pressure in Pa, ρ the density in $kg \cdot m^{-3}$, η the effective viscosity in $Pa \cdot s$ and $\boldsymbol{g}$ the vector of acceleration within the gravity field, 9.81 $m \cdot s^{-2}$.

Calculation of the pressure and velocity fields for every iteration was performed using the penalty method for the continuity equation (Cuvelier et al., 1986; Gerya et

al., 2000; Daniel et al., 2001). The derivation from the Navier-Stokes equations and the penalty method technique is found in Appendix D.

1.5.3.2 Viscosity in geologic domains

The effective viscosity is the parameters that will retain the geological domains present in the case study (micaschist, serpentinites and peridotites) depending of the strain rate $\dot{\varepsilon}$. We assume that the channel walls (downgoing slab and hanging wall) are rigid plates.

For materials undergoing deformation by creep, their strength is predicted by experimental flow laws of the power law type (Ranalli, 1995). Under this rheological behavior the effective viscosity is expressed as:

$$\eta_{eff} = \frac{\dot{\varepsilon}^{(1/n-1)}}{A_D^{1/n}} \exp\left(\frac{E}{nRT}\right)$$

where $\dot{\varepsilon}$ is the strain rate in s^{-1}, E is the creep activation energy in $kJ \cdot mol^{-1}$, A_D is the Dorn parameter in $Pa^{-n} \cdot s^{-1}$, n the stress exponent, T the temperature in K and R is the gas constant.

Rheological parameters (E,A_D and n), were chosen considering the geological domains described and experimental studies for these lithologies found in the literature.

The boundary conditions were chosen considering a wide variety of tectonic scenarios. The parameters in the sensibility analysis were the width of the subduction channel, the convergence velocity and dip of the down going slab. The size of the ultramafic body was also explored and constrained by the geophysical

results (section 1.5.2). Finally, model results are shown and interpreted is Chapter 2 (paper section) and in Appendix D for further description of some boundary conditions.

The rest of the document is composed by the research article (Chapter 2) and the appendixes. The research paper has been submitted to the journal *Geochemistry, Geophysics, Geosystems,* while the material described in the appendixes provide additional theory and information about the geophysical methods, inversion procedures, numerical modelling and further results.

2. ROLE OF THE SUBDUCTION CHANNEL IN THE EMPLACEMENT OF ULTRAMAFIC BODIES IN CONVERGENT MARGINS: INSIGHTS FROM PALEOZOIC METAPERIDOTITES IN THE COASTAL CORDILLERA OF SOUTH-CENTRAL CHILE

2.1 Introduction

High- and ultrahigh-pressure metamorphic rocks, as well as ultramafic rocks, are common lithologies in accretionary complexes (e.g., Ernst et al., 1999; Ernst, 2006). These rocks usually present a counterclockwise pressure-temperature (P-T) path, which implies a shallow origin, a deep burial, and later exhumation (Frost & Frost, 2013). However, the emplacement of dense peridotites cannot involve buoyancy in such a cold tectonic environment, and, other mechanisms must therefore act to overcome the negative buoyancy of these rocks. Here, we explore a possible emplacement mechanism for ultramafic rocks involving upwelling along the subduction channel.

The subduction channel (Shreve & Cloos, 1986; Cloos & Shreve 1988) is a zone of strong shearing containing weak material between the subducted slab and the overriding block. In general, the subduction channel mainly comprises oceanic and continental sediments; these are transported down into the asthenosphere and later returned to the upper crust as high-pressure metamorphic rocks (Shreve & Cloos, 1986; Cloos & Shreve, 1988).

The subduction channel model supports the presence of a sedimentary component in the geochemical signature of several volcanic arcs (Hole et al., 1984; Myers et al., 1986), the presence of blueschist-facies terranes in the Franciscan subduction complex (Shreve & Cloos, 1986), and the occurrence of massive oceanic eclogite lenses in serpentinite host rocks in accretionary complexes (Agard et al., 2008; Guillot et al., 2009), implying a deep origin of ultramafic rocks in the upper mantle. These observations support the idea that subducting material in oceanic and continental subduction zones can reach great depths before being exhumed. The exhumation process is triggered by return flow produced near the hanging wall of the subduction channel (Shreve & Cloos, 1986; Cloos & Shreve, 1988; Gerya et al., 2002; Beaumont et al., 2009).

The subduction channel model has also been successfully validated by several numerical simulations (Beaumont et al., 2009; Gerya et al., 2002; Angiboust et al., 2012; Wang et al., 2019) and the reconstructed P-T trajectories in these simulations are in good agreement with the retrograde metamorphic conditions during exhumation (Gerya et al., 2002; Beaumont et al., 2009). The pattern and magnitude of the return flow is primary controlled by the rheology, temperature field, and geometry of the subduction channel and by the velocity and dip of the downgoing slab (Gerya et al., 2002; Wang et al., 2019) (Figure 2-1). Consequently, the pattern/magnitude of the channel flow controls the size (and weight) of the uplifted ultramafic block(s) and the main driving force if produced by the buoyancy of sediments in the system and the motion of the downgoing slab (Shreve & Cloos,

1986). In terms of lithology, the subduction channel is generally composed of subducting sediments, serpentinites, and peridotites (Cloos & Shreve, 1988). The subducting sediments and serpentinites have positive buoyancy and low viscosity, which allows the growth of subduction-channel return flow, thus providing the driving force for the exhumation of peridotites.

The geometry and especially the width of the subduction channel progressively evolves due to hydration of the hanging wall (Gerya et al., 2002; Plissart et al., 2019). The width of the subduction channel varies from 5 to 10 km of hydrated material on the upper part of the slab (Abers et al., 2006). Recent studies using numerical simulations (Wang et al., 2019) concluded that low-viscosity serpentinites play a key role in the exhumation of ultramafic rocks since they can carry dense lenses or even blocks into the return flow. These results were obtained for accretionary complexes, where serpentinites are host rocks for ultramafic bodies and share the same deformational history as the accretionary prism (Plissart et al., 2019). This geological process is the main mechanism for exhumation from depths greater than 100 km to shallow levels or even the surface (e.g. Cloos & Shreve, 1988; Bonnet et al., 2018; Cooperdock et al., 2018).

The purpose of this work was to determine tectonic/petrophysical scenarios under which the subduction-channel flow can effectively transport ultramafic blocks from depth to shallow levels in the crust and emplace them in the Paleozoic accretionary complex of south-central Chile.

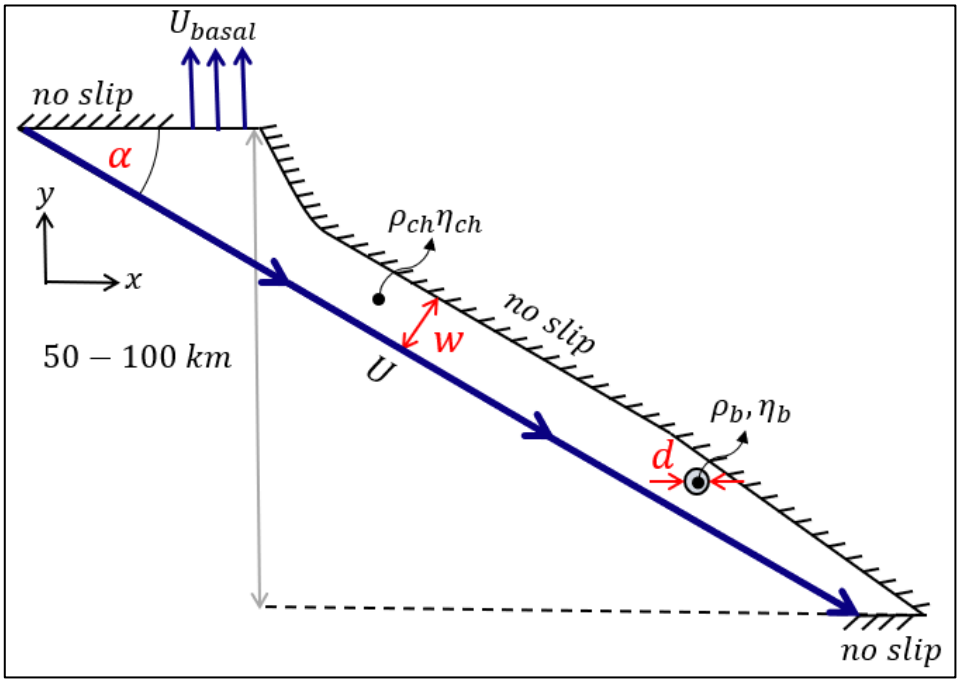

Figure 2-1: Schematic model of the subduction channel. Depth estimates depend on oceanic (< 50 km) or continental (~ 100 km) tectonic configuration. Geometrical parameters are indicated in red: dip of the downgoing slab (α), channel width (w), and body diameter (d). Velocity boundary conditions are indicated in blue: velocity of the downgoing slab (U), basal accretion rate (U_{basal}), and no-slip conditions for the remaining boundaries (further discussed in Section 2.4). Rheological parameters (density ρ and viscosity η) are assigned to two domains: the subduction channel (ch subscript) and the ultramafic body (b subscript). Estimations of effective viscosity are detailed in Section 2.3.2, and densities are assumed to be constant with values of ρ_{ch}=2.6 gr/cm^3 and ρ_b=2.8 gr/cm^3. The bottom wedge of the subduction channel is neglected in the model since the corner flow is already achieved with the present geometry.

2.2 Geological Setting

2.1 Metamorphic complex of the Coastal Cordillera of south-central Chile

The Coastal Cordillera of south-central Chile, which extends between 32°-43°S latitude, is composed of two parallel NS oriented metamorphic belts, i.e., the Western and Eastern Series. Both series represent the accretionary complex at the continental paleo-Pacific margin of Gondwana during the Late Paleozoic (Aguirre et al., 1972; Figure 2-2).

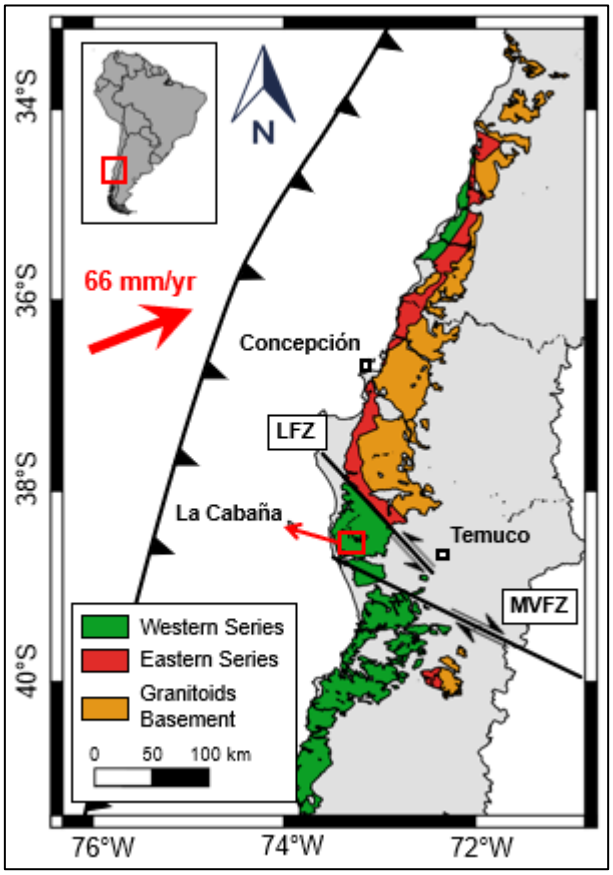

Figure 2-2: Major geological units of the Coastal Cordillera of south-central Chile (modified from Romero et al., 2019). Geological faults: Lanalhue Fault Zone (LFZ; Glodny et al., 2008), Mocha-Villarrica Fault Zone (MVFZ; Melnick & Echtler, 2006). Convergence velocity vector from Angermann et al. (1999).

The Eastern Series consists of slightly deformed metasedimentary rocks affected by high-temperature and low-pressure metamorphism associated with frontal accretion processes (González-Bonorino, 1971; Willner, 2005). The Western Series comprises mica schist of continental origin, metabasites (metagabbros and metavolcanic rocks), and peridotites with variable degrees of serpentinization (Barra et al., 1998,; 2014) scattered along this unit which have been interpreted as an

ophiolite complex (Hervé, 1988; Barra et al., 1998; González-Jiménez et al., 2014). The Western Series (WS) is related to basal accretion processes (Willner, 2005,; Glodny et al., 2005) and is characterized by greenschist-facies conditions (7–-9.3 kbar and 380–°-400 °C; González-Jiménez et al., 2016); however, some isolated blocks record blueschist metamorphic conditions (9.5–-10.7 kbar and 350–°-385 °C; Willner, 2005; González-Jiménez et al., 2017).

The geotectonic significance of this ophiolite complex is still under debate; various models have been proposed, varying from fore-arc (Hervé et al., 1976; Godoy, 1979), back-arc (Frutos & Alfaro, 1987; Höfer et al., 2001) and intra-arc (Barra et al., 1988; González-Jiménez et al., 2014) models.

Here we focus on the La Cabaña metaperidotite massif within the Western Series of the metamorphic complex. La Cabaña area is located 60 km northwest of the city of Temuco (Figure 2-2) and hosts the largest serpentinized peridotite body recognized so far in the Coastal Cordillera. Additionally, it is the only location within the Western Series where chromitite bodies have been identified (Barra et al., 1998; 2014; Höfer et al., 2001).

2.2 La Cabaña ultramafic bodies

The largest ultramafic body in La Cabaña is Centinela Bajo Norte (Figure 2-3a), which is a serpentinized peridotite with chromite lenses and pods embedded in a mica schist host rock (Barra et al., 1998, 2014; Höfer et al., 2001). Figure 2-3b shows the results of in-situ measurements of the magnetic susceptibility of various

rock types in the area. Due to the presence of dense rainforest, the precise dimensions of the Centinela Bajo Norte body remain unknown.

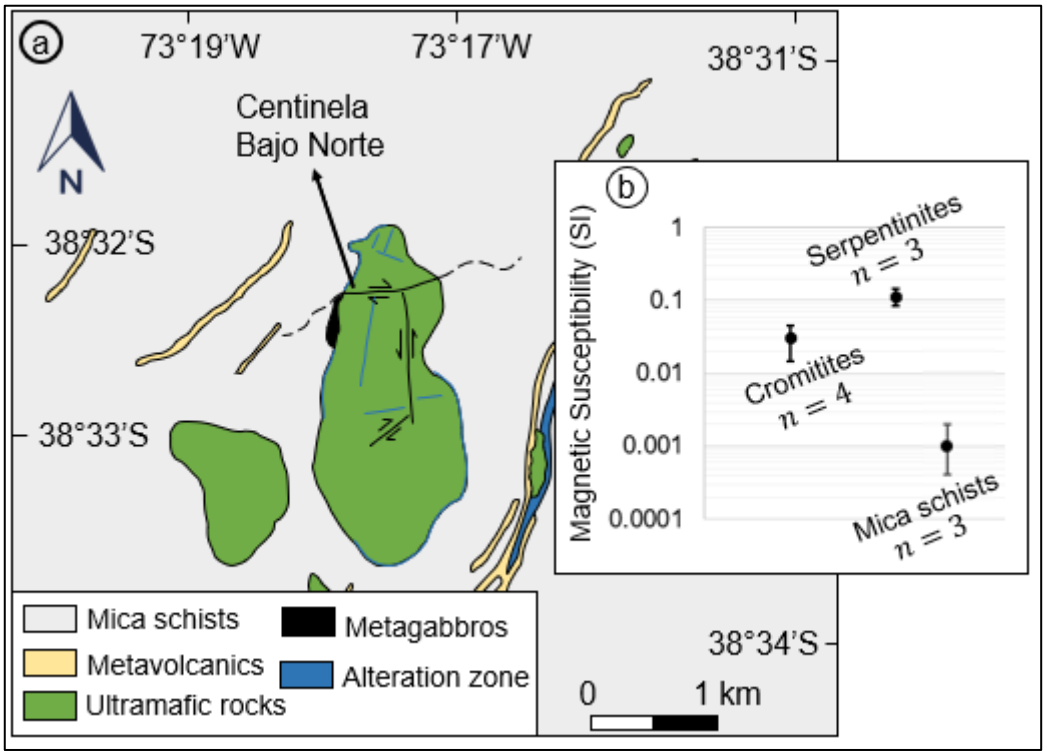

Figure 2-3: a) Local geological map in La Cabaña area (modified from Höfer et al., 2001; Romero et al., 2017) b) Magnetic susceptibility measurements of rock samples (n) in La Cabaña area.

Previous studies concluded that these ultramafic rocks experienced hydration at relatively high P-T conditions (1.6–3.2 GPa, <400 °C; González-Jiménez et al., 2016) and that serpentinization occurred at even higher P-T conditions (15–26 kbar, 450–650 °C) in an already cooled subduction system (Plissart et al., 2019). The available geological evidence confirms that La Cabaña ultramafic rocks recorded the evolution of the uppermost part of the mantle corner before being captured by the subduction channel (Plissart et al., 2019).

Furthermore, geochemical studies concluded that these ultramafic bodies have an island-arc geochemical signature (Barra et al., 1998; González-Jiménez et al., 2014), and that peridotites and metavolcanic rocks in the La Cabaña area formed during the Devonian (Romero et al., 2017) in a marginal basin associated with a suprasubduction zone that included a subduction channel process (González-Jiménez et al., 2014). These authors also provided geochronological constraints for the timing of the tectonic emplacement of ultramafic rocks into the accretionary prism within a time interval of less than 40 Ma during the Permian, coeval with the northernmost outcrop of the Western Series (Romero et al., 2017; Romero et al., 2019).

2.3 Methods and Results

We performed numerical modeling of the La Cabaña massif, which is located in the Paleozoic accretionary prism of south-central Chile (Hervé et al., 1988). In order to perform these simulations, we first determined the size and petrophysical characteristics of the ultramafic body via an airborne magnetic survey using an unmanned airborne vehicles (UAV) and electrical resistivity tomography (ERT). These surveys allowed us to clearly outline the Centinela Bajo serpentinized peridotite due to its high electrical conductivity and magnetization. In contrast, the mica schist host rocks have a low magnetization and low electrical conductivity since they are mainly composed of metamorphosed subducted sediments.

The densities of the serpentinized peridotites and the host rocks were directly determined from rock samples. We then used the size estimated and densities for

the computation of possible scenarios for the subduction-channel flow. In our models, we assumed the steady-state flow of a viscous incompressible Newtonian fluid at very low Reynolds numbers, where the dynamic Navier–Stokes equations are reduced to the Stokes approximation. This simplification is a standard procedure for geodynamic problems (Turcotte & Schubert, 2014). The results of the modeling are discussed in the geodynamic context of a long-term subduction process at convergent margins.

To further model the emplacement mechanism of ultramafic rocks, it is necessary to quantify the strength of the rocks which undergo long-term deformation in the subduction channel. Assuming a power law rheology, the effective viscosity (η) can be used to predict the rock strength under creep conditions using experimental flow (Ranalli, 1995). However, the effective viscosity is strongly influenced by the subduction-zone dynamics at all time scales (e.g., Gerya et al., 2002; Yáñez & Cembrano, 2003; Beaumont et al., 2009; Angiboust et al., 2012). Therefore, appropriate pressure and temperature conditions must be considered along subduction zones, which are characterized by cold isotherms (<600 °C; Davies & Stevenson, 1992) and medium-to-high pressures (0–2 GPa) in various tectonic settings (Stern, 2002). These pressure and temperature conditions have been reproduced for multiple lithologies that are present in the subduction channel (Shea & Kronenberg, 1992; Karato & Jung, 2003; Hilairet et al., 2007). The specific parameters used for the estimation of the effective viscosity will be discussed in Section 2.3.2.2.

2.3.1. Geophysical Survey

In order to model the emplacement of the ultramafic rocks in the accretionary prism, we first determined the size, mass, and petrophysical characteristics of these bodies. Since the dense forest cover in the study area precluded detailed geological mapping, we used indirect geophysical methods to better constrain these parameters.

2.3.1.1 Magnetic survey and 3D model inversion

We deployed an airborne magnetic survey over La Cabaña ultramafic bodies using an UAV system. The survey covered a total distance of 91 km, and consisted of EW flights lines with a spacing of ~200 m at two barometric altitudes, i.e., 768 and 853 m (Figure 2-4). The survey was conducted using a Mag-03 Three-axis fluxgate magnetometer (Bartington Instruments Ltd., Oxon, UK), which was installed in the UAV, and a Geometrics 858 vapor cesium magnetometer, which was installed at the base station (Geometrics, San Jose, CA, USA).

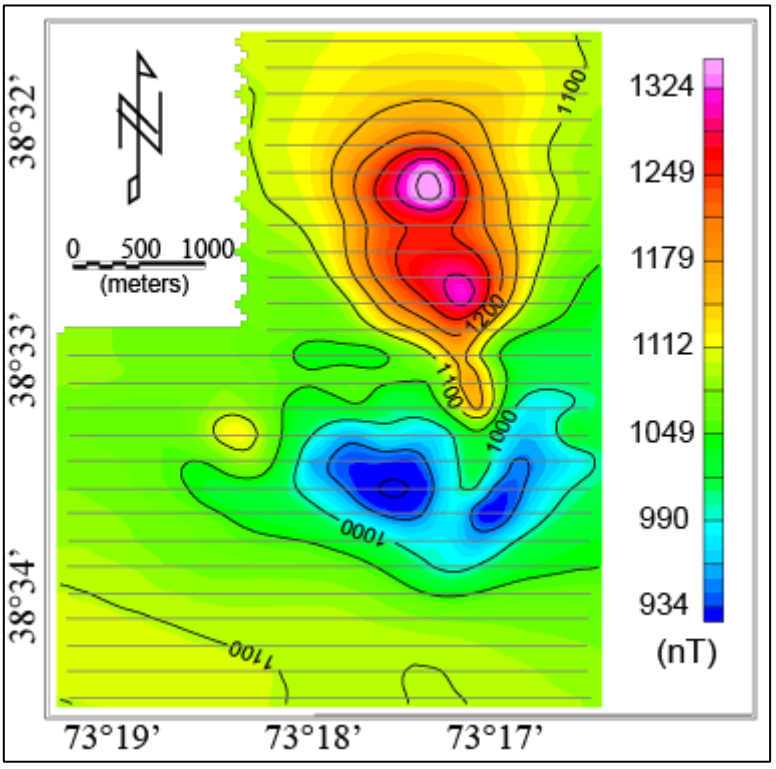

Figure 2-4: Map showing the measured raw total magnetic intensity of the La Cabaña ultramafic bodies acquired via an UAV based airborne magnetic survey. Horizontal gray lines show the flight paths of the UAV. Contour increments are 50 nT.

Data reduction involved the standard diurnal variation and IGRF removal (Telford & Sheriff, 1990). However, the most significant data correction which was applied was the topographic correction. This correction was performed to account for: (1) two data subsets with different flight altitudes; and (2) the large topographic reliefs in the study area in both data subsets (±200 m from the mean altitude above sea level). In order to reduce the topographic distortion, we implemented the 2D continuation algorithm of Hansen & Miyazaki (1984) to perform upward and downward continuations to an arbitrary surface parallel to the ground level.

After performing the continuation to a surface that is parallel to and 200 m above the topography, we carried out a 3D inversion over the filtered data using the reduction to the magnetic pole (RTP) grid (Figure 2-5a). To perform this task, we used the MAG3D software from the University of British Columbia-Geophysical Inversion Facility (UBC-GIF; Li & Oldenburg, 1996). Mesh generation and inversion parameters such as depth weighting ($\beta=3$; $z_0=0$) and reference model (0.001 SI) were determined following the software guidelines. The susceptibility values were set from 0.001 to 0.1 SI, consistent with our measurements in the La Cabaña area for the three geological domains (see Figure 2-3b). A mean uncertainty of 1.15% in the discrete inversion results (Figure 2-5b,c) was achieved using these parameters.

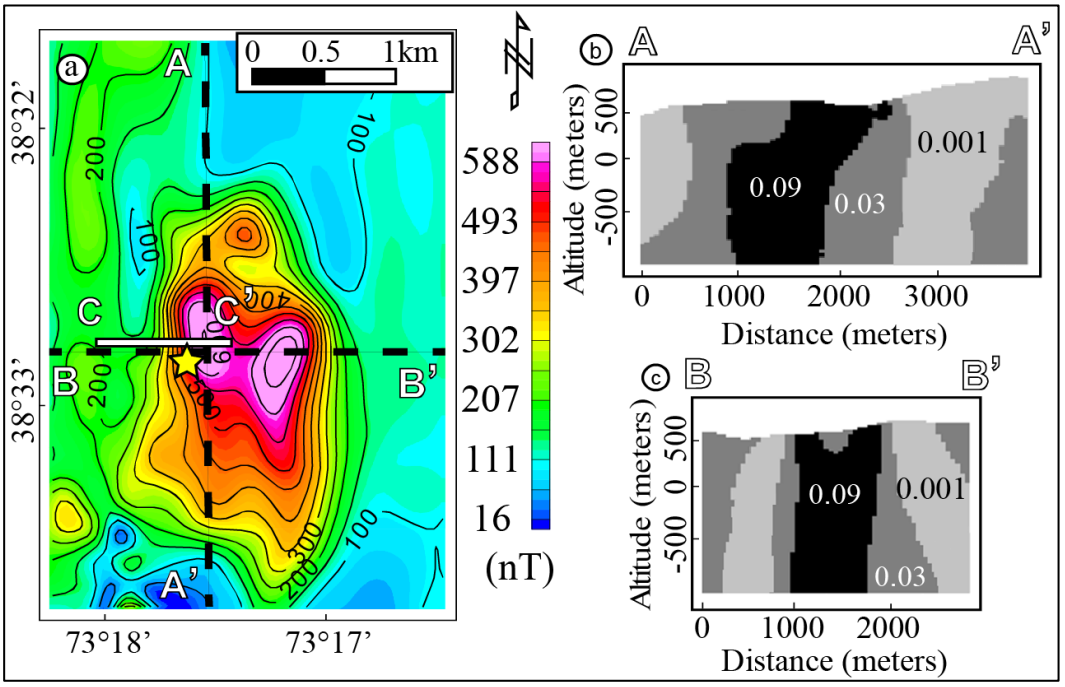

Figure 2-5: a) Reduction to the magnetic pole after data reduction and continuation to a common arbitrary surface that is parallel to and 200 m above the topography. Sections A-A' and B-B' correspond to magnetic inversion cross-sections, and section C-C' corresponds to an electrical resistivity tomography survey and later inversion cross-section. Contour increments are 50 nT. (b) NS cross section of the 3D magnetic inversion. (c) EW cross section of the 3D magnetic inversion, magnetic susceptibility values inverted are indicated in the figure.

The RTP signal obtained in the study area has similar wavelengths (2–3 km) to the Centinela Bajo Norte ultramafic body in the same area, reaching amplitudes of 300 nT with peaks >500 nT (Figure 2-5a). These peaks are directly correlated with two main features: (1) serpentinite outcrops in which we performed in-situ measurement of magnetic susceptibility (yellow star in Figure 2-5a); and (2) the shallowest part of the highly magnetized body (0.09 SI in Figure 2-5b,c) that was suggested by our

inversion results. On the other hand, mica schist host rocks are almost non-magnetized and are represented by low amplitudes in the RTP map (<100 nT). It is important to mention that the RTP signal after the continuation is not directly correlated with the topography; this suggests that the main magnetic anomaly is produced by subsurface geological features that are not correlated with large topographic reliefs produced by the continuation algorithm (e.g., Yáñez et al., 2017). The inversion results correctly account for the high contrast in susceptibility between the host rocks and the peridotites/serpentinites. Furthermore, the magnetic susceptibility recovered by our models correlates well with our in-situ measurements (Figure 2-3b). Chromitite pods are embedded in the peridotites/serpentinites, however these cannot be discriminated from the ultramafic rocks as they have a similar magnetic susceptibility.

2.3.1.2 Electric resistivity tomography survey and inversion

Potential-field methods have a poor resolution to resolve vertical contacts. Hence, we performed an electrical geophysical campaign to correctly account these possible structures and contacts. The instrument used for ERT data acquisition was the ABEM Terrameter LS2 with 48 electrode arrays and 20 m dipole spacing. To improve the data quality, we used 4 stacking for each quadripole and a threshold of 10% standard deviation for every data point to reduce noisy measurements in the pseudosection. We used a dipole-dipole configuration, because this array is the most effective for vertical structures with good horizontal and depth coverage (Sharma & Verma, 2015). During fieldwork, we made several profiles in La Cabaña area but

only one was reliable for geologic interpretations in the context of the present research (Figure 2-5a; C-C' cross section).

For the 2D inversion of the pseudosection, we used the ZondRes2D software. We tested multiple initial background models and inversion methods with a minimum and maximum resistivity of 1 and 10000 Ω-m, respectively, as the inverse problem for ERT data is a nonlinear problem. For the inversion, we used 539 of the 605 datapoints measured. We chose the inversion with the best fit considering geological constrains and the magnetic results. A mean error of 4.9% was determined in the inversion (Figure 2-6).

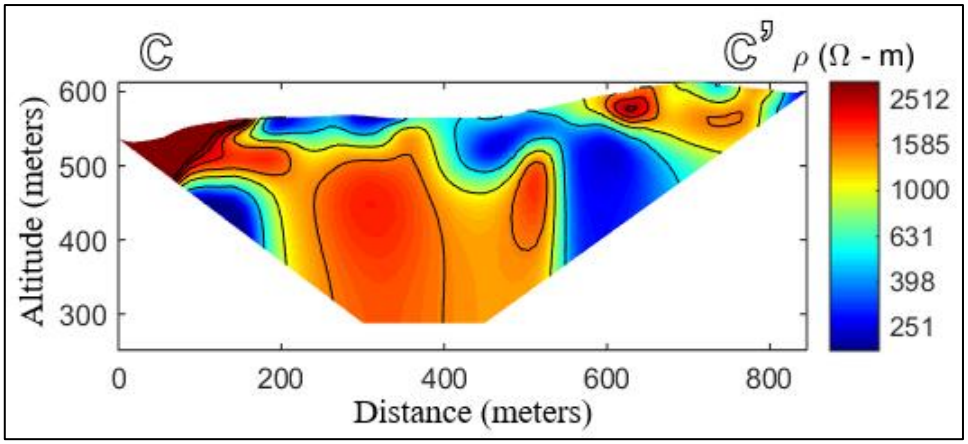

Figure 2-6: Electrical resistivity tomography (ERT) inversion after the filtering of noisy data. Contour increments are 500 Ω-m.

Based on the ERT inversion, the contact between the two resistivity domains seems to be sub-vertical, which is in good agreement with the results of the magnetic inversions (Figure 2-5b) and the inferred contact between the ultramafic rocks and the mica schists (González-Jiménez et al., 2016).

In the inverted ERT section (Figure 2-6), we identified a high-resistivity (>1000 **Ω**-m) and a medium-to-low resistivity domain (<400 **Ω**-m). The first domain is likely to correspond to schists, which have a high resistivity (White & Beamish, 2014) and are spatially correlated with the mica schist host rock and the low RTP signal in the La Cabaña area. The second (medium-to-low) resistivity domain is likely to correspond to interconnected magnetite in the ultramafic rocks (Stesky & Brace, 1973), which is also the source of the high RTP signal (e.g., Hyndman & Peacock, 2003).

Both geophysical inversions (Figure 2-5b,c and Figure 2-6) were used to constrain the dimensions of the Centinela Bajo ultramafic body, and confirmed its vertical contact with the host rocks. Based on these inversions, the Centinela Bajo body was determined to be an elongated body with a length of 3 km in the north direction, a width of 1.5 km, and a depth of about 1.5 km. These values were used as constraints in the channel flow numerical modeling.

2.3.2. Numerical modelling of the subduction channel flow

2.3.2.1 Governing Equations

To model the return flow in the subduction channel, we adopted a slow viscous approach using the Stokes and continuity equations:

$$\nabla^2(\eta \boldsymbol{u}) - \nabla p + \rho \boldsymbol{g} = 0$$

$$\nabla \cdot (\rho \boldsymbol{u}) = 0$$

where $\boldsymbol{u}$ is the velocity vector in $m \cdot s^{-1}$, p is the pressure in Pa, ρ is the density in $kg \cdot m^{-3}$, η is the effective viscosity in $Pa \cdot s$ and $\boldsymbol{g}$ is the vector of acceleration within the gravity field, 9.81 $m \cdot s^{-2}$.

These set of equations approximate the Navier-Stokes equations for viscous flow at very low Reynolds number, which is achieved if $\boldsymbol{u}$ is sufficiently small compared to the effective viscosity η and considering a steady-state case for an incompressible fluid (Turcotte & Schubert, 2014). The pressure and velocity fields were calculated for every iteration using the penalty method for the continuity equation (Cuvelier et al., 1986; Gerya et al., 2000; Daniel et al., 2001).

2.3.2.2 Viscous domains

In order to represent the units in the La Cabaña area, we defined three viscous domains associated with the following lithologies: (1) mica schist; (2) serpentinite; and (3) peridotite. We assumed that the channel walls (downgoing slab and hanging wall) are rigid plates and thus only kinematic boundary conditions were included (see Section 2.3.3.3.).

The strength of materials undergoing deformation by creep is predicted using experimental flow laws of the power-law type (Ranalli, 1995). Under this rheological behavior, the effective viscosity is expressed as:

$$\eta_{eff} = \frac{\dot{\varepsilon}^{(1/n-1)}}{A_D^{1/n}} \exp\left(\frac{E}{nRT}\right)$$

where $\dot{\varepsilon}$ is the strain rate in s^{-1}, E is the creep activation energy in $kJ \cdot mol^{-1}$, A_D is the Dorn parameter in $Pa^{-n} \cdot s^{-1}$, n is the stress exponent, T is the temperature in K and R is $8.314\ J \cdot K^{-1} \cdot mol^{-1}$, the gas constant.

Rheological parameters (E,A_D and n) were chosen considering the geological domains described and experimental studies for these lithologies. For instance, host rocks composed by mica schist are given by experimental data (Shea and Kronenberg, 1992). For the ultramafic body, we estimated a composition of 25% peridotites (wet olivine; Karato and Jung, 2003) and 75% serpentinites (Hilairet et al., 2007). The temperature field was obtained by coupled thermo-mechanical simulations for a steep angle dip between oceanic plates obtained by Gerya et al. (2002). This specific tectonic environment was chosen based on the island-arc geochemical signature in La Cabaña ultramafic bodies (Barra et al., 1998; González-Jiménez et al., 2014).

To ensure the simplicity of our model, we included the strain rate ($\dot{\varepsilon}$) in the flow power-law with a prescribed approach in which we defined three domains, each with a fixed strain rate, namely, the downgoing slab, the return flow, and the hanging wall. Each domain was computed with an initial guess of a constant viscosity of $10^{19}\ Pa \cdot s$. After a few iterations of updating the viscosity, we set the width and the strain rate of each domain until the viscosity values remained unchanged; these values were used as the effective viscosity for each of the three geological domains. Specifically, $0.4 \cdot 10^{19}\ Pa \cdot s$ for the downgoing slab, $2.4 \cdot 10^{19}\ Pa \cdot s$ for the return flow, and $0.6 \cdot 10^{19}\ Pa \cdot s$ for the hanging wall (Figure 2-7).

The channel effective viscosity (η_{ch}) was estimated using the rheological parameters of the mica schist, with values between $0.4 - 2.4 \cdot 10^{19}\ Pa \cdot s$ depending on the strain rate domain (Figure 2-7). Similar values of effective viscosity for this weak layer have been used in previous studies (e.g., Daniel et al., 2001; Gerya et al., 2002; Yáñez & Cembrano, 2003). The ultramafic body comprises both serpentinite and peridotite rheological parameters, and hence we tested the following two end-member scenarios: (1) a body with high effective viscosity dominated by the peridotite flow law; and (2) a body with low effective viscosity controlled by the serpentinite flow law. Thus, the effective viscosity of the ultramafic body, η_b, varied from $10^{20}\ Pa \cdot s$ for a weak rheology to $10^{23}\ Pa \cdot s$ for a strong rheology, which is consistent with maximum lithosphere viscosities (e.g., Yáñez & Cembrano, 2003; Daniel et al., 2001).

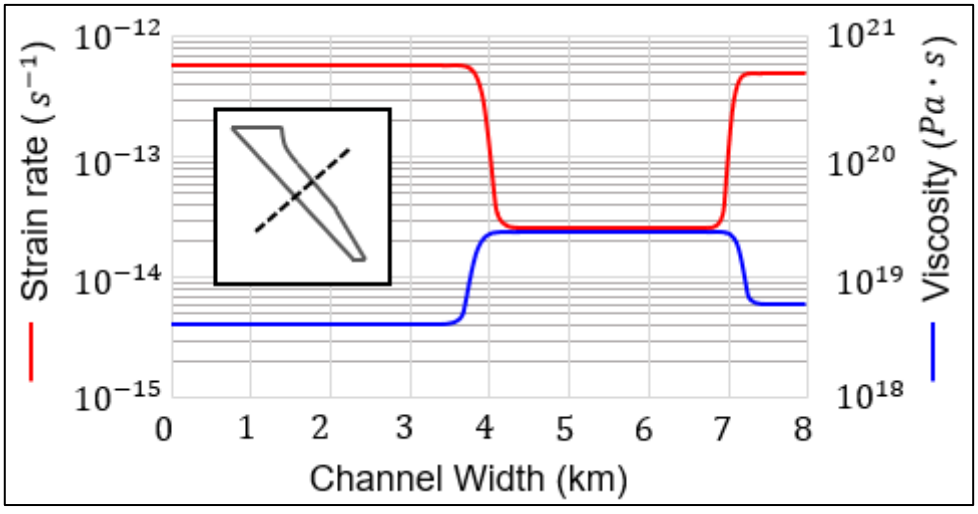

Figure 2-7: Calculated strain rate and effective viscosity for a cross-section across the subduction channel (dashed black line) as calculated using the reference model. Channel

width distance starts from the lower left (slab side) to the upper right (continental side).

Boundary conditions and geometry

The boundary conditions that were used for the modeling are shown in Figure 2-1. Two values for the velocity of the downgoing slab (U) were tested, namely 60 and 120 mm/yr, based on the actual velocity vector of the Nazca plate (Angermann et al., 1999) and reconstructions of the velocities of oceanic plates during the Paleozoic (Matthews et al., 2016), respectively. In our models, a velocity $U_{basal} = 0.2U$ was set above the subduction channel to account for the basal accretion. This value was determined based on exhumation rates that have been reported worldwide, which in most cases are a percentage of the velocity of the downgoing slab (Ring et al., 1999). The bottom and the hanging wall of the subduction channel were set to a no-slip condition; this assumption will be discussed in Section 2.4.4.

In order to determine the precise combination of geological parameters under which an ultramafic body will be emplaced in a forearc environment, we examined the dip of the downgoing slab (α), the diameter of the ultramafic body (d), and channel width (w). Each parameter was tested for three different scenarios (Table 1), where the reference model was assumed to represent the present tectonic setting in the study area (REF in Table 1).

Table 2-1: Parameters tested for every simulation. For further details see Figure 2-1. Reference model parameters were chosen according to the present tectonic configuration inferred for the La Cabaña area. Parameter values were chosen according to the following references: subduction angle: Pardo et al. (2003); channel width: Abers et al. (2006); diameter of ultramafic body: this study.

Model #	Subduction angle $\alpha(°)$	Channel width: $w(km)$	Body Diameter: $d(km)$	Rheology
(REF)	30	8	1.5	Weak
(1)	30	8	0.75	Weak
(2)	30	8	3	Weak
(3)	15	8	1.5	Weak
(4)	60	8	1.5	Weak
(5)	30	4	1.5	Weak
(6)	30	12	1.5	Weak
(7)	30	8	1.5	Strong

The FlexPDE v6.5 software for finite element partial differential equations was used to perform the calculations of the velocity and pressure field. Between 4000-5000 triangular elements type and quadratic interpolation were used for each scenario.

2.3.2.3 Modeling results

The modeled velocity field within the subduction channel is shown in Figure 2-8, while the modeled travel-time path for every scenario is illustrated in Figure 2-9. The magnitude of the return flow is primarily controlled by the dip of the downgoing slab (α) and the width of the subduction channel (w). Maximum return-flow velocities were achieved with a wide subduction channel ($w = 12\ km$) and a steep

subduction angle ($\alpha = 60°$), which produced maximum velocities of 36 and 48 mm/yr, respectively. These values are about 40% of the velocity of the downgoing slab, and produce the highest exhumation rates and the lowest interval time of ascent (ITA), which are <3 Myrs with a minimum of 2.2 Ma for $\alpha = 60°$ (Figure 2-9).

On the other hand, low return-flow velocities were obtained with a narrow subduction channel ($w = 4\ km$) and a gentle subduction angle ($\alpha = 15°$), which produced return-flow velocities of 4.9 and 6 mm/yr, respectively. With these parameters, the return flow is not strong enough to transport a dense peridotite block, and hence it sinks deep into the mantle.

When the velocity of the downgoing slab is reduced, the ITA is also significantly reduced. For instance, in the reference model, when $U = 60\ mm/yr$, the simulated ITA is 5 Ma, whereas when $U = 120\ mm/yr$, the simulated ITA is 3.2 Ma (Figure 2-9). The size of the ultramafic block has a minor effect on the ITA. Larger bodies, which are heavier and experience stronger friction, will counteract the vertical component of the return flow, making the ITA slower in the long-term (Figure 2-9). Since the buoyancy of the ultramafic block is directly related to its size and weight, three scenarios can be described: (1) the return flow is strong enough to emplace the rock block to shallow levels (reference model in Figure 2-8); (2) a weak return flow produces very large ITAs ($\alpha = 15°$ in Figure 2-9); and (3) a block diameter that is similar to the width of the subduction channel will cause the block to sink due to its weight and the dragging force of the downgoing slab ($w = 4\ km$ in Figure 2-8).

Regarding the shape of the ultramafic block after the emplacement (red insets in Figure 2-8), a strong rheology controlled by the peridotite flow results in the block being mostly undeformed, thus preserving the block's original circular and slightly elongated shape ("Strong Rheology" in Figure 2-8). More interestingly, a weak rheology for the ultramafic body leads to the elongation of the body in depth (body length ~3 km; "Weak Rheology" in Figure 2-8) and a body width which is the same as that observed in the magnetic inversions (~1.5 km; Figure 2-5c).

The strain rates calculated for the three domains described above were determined at around 10^{-13} to $10^{-14}\ s^{-1}$, and the corresponding channel effective viscosities in these domains were in the range of $10^{19} - 10^{20}\ Pa \cdot s$ (Figure 2-7) in the reference model. Other simulations predicted the same strain rate and viscosity behavior, i.e., the lowest viscosity was obtained near the slab, slightly lower for the hanging wall, and the highest was obtained for the return flow, whereas the opposite trend was observed for the strain rates.

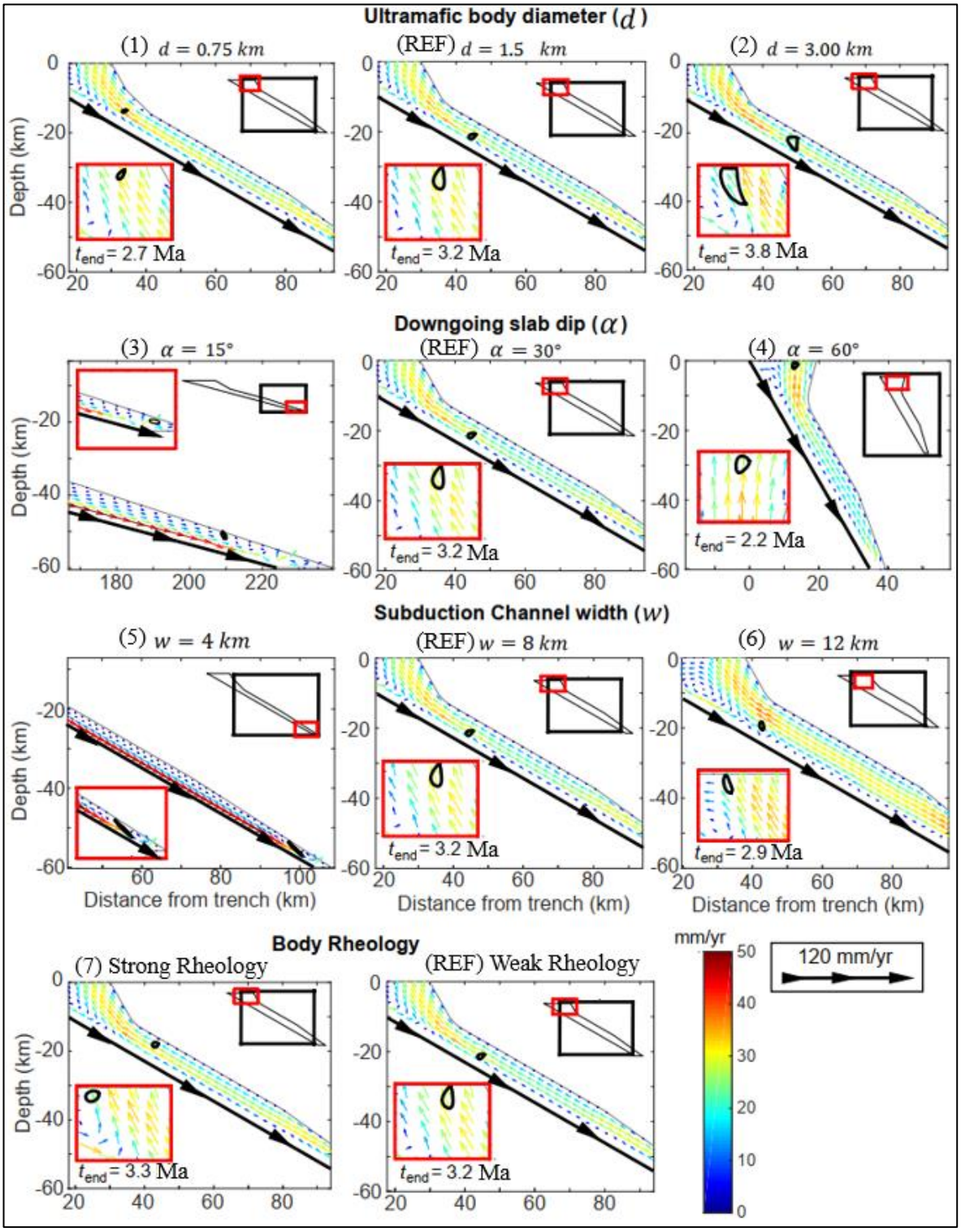
Ultramafic body diameter (d)
(1) d = 0.75 km
(REF) d = 1.5 km
(2) d = 3.00 km
Depth (km)
t_end = 2.7 Ma
t_end = 3.2 Ma
t_end = 3.8 Ma
Downgoing slab dip (α)
(3) α = 15°
(REF) α = 30°
(4) α = 60°
t_end = 3.2 Ma
t_end = 2.2 Ma
Subduction Channel width (w)
(5) w = 4 km
(REF) w = 8 km
(6) w = 12 km
t_end = 3.2 Ma
t_end = 2.9 Ma
Distance from trench (km)
Body Rheology
(7) Strong Rheology
(REF) Weak Rheology
t_end = 3.3 Ma
t_end = 3.2 Ma
mm/yr
120 mm/yr

Figure 2-8: Flow velocity vector solution for $t = 2.2$ Ma for every scenario presented in Table 1. Black circular/ovoidal shapes represent the position of the ultramafic block. The upper-right insets represent the geometry of the subduction channel and show the location of the lower-left inset, which displays the final position of the block. See text for discussion. Also shown is the time required to reach the top of the subduction channel (t_{end}). All the panels have a 1:1 aspect ratio.

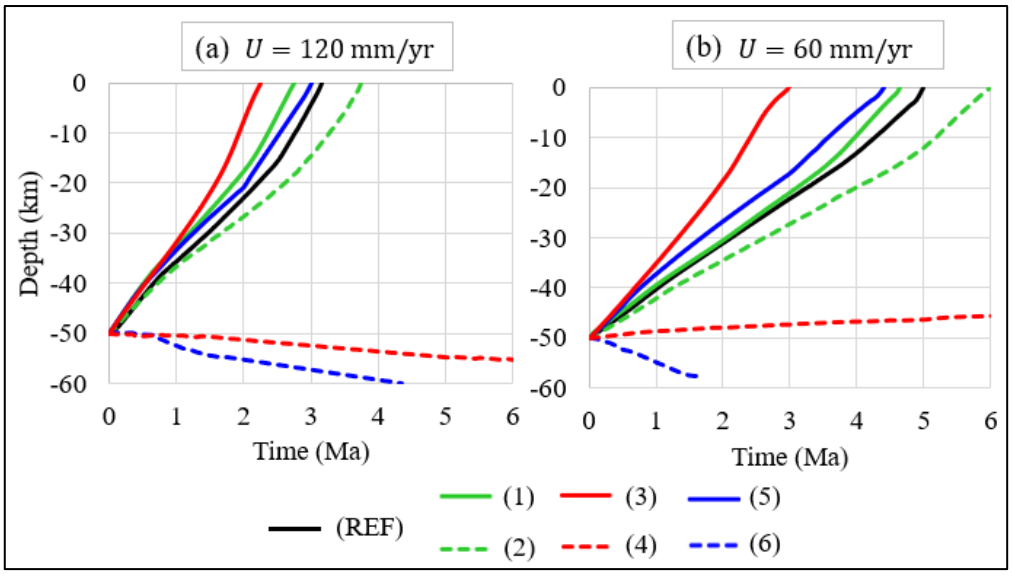

Figure 2-9: Travel-time paths for every simulation for (a) $U = 120\ mm/yr$ and (b) $U = 60\ mm/yr$. Dashed lines represent slower scenarios than the reference model (solid black line) and solid lines represent faster scenarios. Colors represent the same geometrical parameter variation.

2.4 Discussion

Here, the model results are discussed in the geodynamic context of a long-term subduction process at a convergent margin. Our numerical simulations provide some

insights into the tectonic configuration and processes involved in the emplacement of ultramafic rocks in accretionary complexes.

2.4.1 Return flow as an emplacement mechanism

The velocities of the return flow within the subduction channel can vary by up to one order of magnitude depending on the tectonic configuration. The velocities and time span for the emplacement determined here are in good agreement with previously reported data (Shreve & Cloos, 1986; Cloos & Shreve, 1988; Ring et al., 1999, Gerya et al., 2002; Beaumont et al., 2009). In general, exhumation velocity is affected by two factors: (1) plate kinematics and subduction slab geometry; or (2) subduction channel geometry. The former is related to the dip and velocity of the downgoing slab, i.e., steep angles and fast velocities can yield exhumation rates of 20–50 mm/yr. The latter depends on the width of the subduction channel; wide subduction channels facilitate the development of a stronger return flow, yielding exhumation rates of >20 mm/yr. Consequently, we can expect exhumation rates of up to 40% of the convergence velocity.

2.4.2 Relationship between the width of the subduction channel and block dimensions

In our models, we considered a fixed width of the subduction channel; however, this geometrical parameter is strongly dependent on the progressive hydration and serpentinization of the hanging wall and the mantle wedge (Gerya et al., 2002; Angiboust et al., 2012). Thus, the width of the subduction channel can be seen as an

evolving process, from a narrow width (<4 km) in the early stages of the subduction to larger widths (~10 km) for the case of mature subduction systems. It follows that the size of the ultramafic blocks that are exhumed through the subduction channel is directly correlated to the channel width. If the size of the ultramafic body is similar to the width of the channel, it will sink due to the downward flow induced by the motion of the downgoing slab. Hence, during the early stages of subduction, only small lenses of ultramafic rocks can be expected to be exhumed (e.g., Agard et al., 2009; Guillot et al., 2009; Angiboust et al., 2011), mainly due to the geometrical restriction, which also produces a weak return flow. On the other hand, at later subduction stages, blocks or even terranes can be uplifted to shallow levels (e.g., Shreve & Cloos, 1986; Lai et al., 2017) since a wider subduction channel leads to a stronger return flow that is capable of transporting larger blocks.

2.4.3 The effect of serpentinization on the buoyancy force

The effect of serpentinization on the buoyancy force of the ultramafic blocks has been addressed in previous studies (Wang et al., 2019). As the degree of serpentinization increases, the density and strength of the block tend to decrease. Thus, hydration of peridotites is a fundamental process to consider when addressing the emplacement of ultramafic bodies in accretionary complexes. The serpentinization of ultramafic rocks can occur in different tectonic settings, including the mantle wedge, the subduction channel, or during emplacement within the accretionary complex, and where serpentinites can be deformed by fluids derived from slab dehydration or from the surrounding sediments.

This change in rheology can play a key role in the emplacement of ultramafic rocks by reducing the negative buoyancy of peridotites. However, even though low-density serpentinites are more likely to be transported within the subduction channel, the density contrast between the ultramafic body and the subduction channel does not change the return-flow pattern. Rather, the return flow is a buoyancy-driven mechanism and appears to be more influenced by the amount of sediments in the channel (e.g. Shreve & Cloos 1986).

Strength estimates using the power-law flow type define peridotites in the strong domain and as having high effective viscosity ($> 10^{22}\ Pa \cdot s$). On the other hand, serpentinites are represented as a relatively weak rheology ($10^{19} - 10^{20}\ \ Pa \cdot s$). In our models, we tested rheologies for the ultramafic block that are controlled by peridotites and serpentinites, respectively. When serpentinite controls the rheology, most of the deformation is localized there, yielding an elongated shape (Weak Rheology in Figure 2-8). In contrast, when peridotite dominates the rheology, the block will remain almost undeformed (Strong Rheology in Figure 2-8). The weak rheology scenario is supported by the microstructure of La Cabaña ultramafic bodies and the enclosing metasedimentary rocks, in which the mica schist host rocks are highly foliated, to almost the same degree as the schistose serpentinites (Plissart et al., 2019). Nevertheless, the cores of some chromite grains show no evidence of deformation and preserve their magmatic signature (Barra et al., 2014; González-Jiménez et al., 2016). Thus, these grains behave as rigid bodies that rotate in a more ductile matrix (e.g., Satsukawa et al., 2015; González-Jiménez et al., 2016). In this

stress field, deformation is accommodated along grain interfaces (e.g. Hull & Rimmer, 1959), promoting fluid infiltration from the surrounding sedimentary host rocks, altering some chromite grains boundaries (Barra et al., 2014; González-Jiménez et al., 2016)

2.4.4 Subduction channel and the mantle corner flow

The interaction between the subduction channel and the asthenosphere wedge is still unclear. Our simulations were performed assuming a no-slip condition, i.e., no interaction between the channel and wedge. This condition may be correct for long time scales, where the system is locked (inter-seismic period). However, the USGS seismic catalog for intermediate and deep earthquakes (>70 km and Mw>7.0), shows slip displacement ranging from a few meters (2019 Mw 8.0, Peru) to almost 10 meters (2019 Mw 7.5, Ecuador). At a global scale, this seismic catalog shows a mean finite fault slip of 3 meters during the last 20 years. Additionally, a rough estimate of the total number of seismic events for intermediate and deep earthquakes, along convergent plate margins (~ 55,000 km; Lallemand, 1999) for the last 40 years of data, gives 1 event per 30 years for a convergent segment of 500 km.

The occurrences of intermediate and deep earthquakes may suggest an interaction between the subduction channel and the asthenosphere wedge when the system is open (co-seismic period) at geological times scales (hundreds of earthquakes during several Ma), allowing mass transport between these two domains. Within this context, mass transfer could be an important process, mainly because the

asthenosphere is a potential source of ultramafic rocks, serpentinized mantle and hydration processes (Stern, 2002).

Our simulations do not address the interaction between the subduction channel and the asthenosphere wedge. However, the first numerical studies by Davies & Stevenson (1992), and a later numerical study by Lin (2014), provide some insights about the interaction between the asthenosphere wedge and the subduction channel, where hot isotherms (>1000 °C) tend to be shallower in the wedge corner. Remarkably, flow field solutions obtained by Lin (2014) indicate that differential pressure gradients are directed towards the return flow in the subduction channel, opposing the motion of the downgoing slab. In the scenario investigated in the present study, we propose that mantle corner flow is the driving force for the incorporation of ultramafic blocks into the return flow in the subduction channel, when large earthquakes allow mass transport between the subduction channel and partially melt upper mantle rocks.

2.4.5 The tectonic emplacement of the La Cabaña ultramafic block

The origin of La Cabaña ultramafic bodies is still a matter of debate. A possible origin that is associated with an intra-arc model has been proposed by several researchers (Barra et al., 1998; González-Jiménez et al., 2014; Romero et al., 2017, 2019; Plissart et al., 2019). This model is supported by several observations, such as the presence of volcanic massive sulfide (VMS) mineralization near La Cabaña, which has been interpreted as being related to a magmatic body in an oceanic

position (Collao et al., 1990). This model is further supported by an island-arc geochemical signature that has been determined for metavolcanic rocks, chromitites, and serpentinized peridotites (Barra et al., 1998; González-Jiménez et al., 2014).

Additionally, the presence of ultramafic bodies and the tectonic configuration of the Western and Eastern Series have been extensively discussed for several years. Hervé et al. (1988) interpreted these ultramafic rocks as fragments of an ophiolite sequence that was obducted onto the western margin of Gondwana during the Paleozoic. More recently, Romero et al. (2019) proposed that the La Cabaña area and most of the Western Series north of the Mocha-Villarica fault zone (MVFZ; Figure 2-2) were emplaced within an old NW-oriented accretionary prism associated with a NW-oriented Carboniferous magmatic arc. Evidence of this accretionary prism is also recorded in Argentina (Chachil plutonic complex; Sillitoe, 1977). In both cases described, they were tectonically controlled by the dextral motion of the MVFZ and later covered by extensive Andean volcanism (Mpodozis & Ramos, 1989). In both contrasting scenarios, the development of a subduction channel is a feasible process given the fact that the ultramafic rocks experienced burial to large depths where humite minerals formed in serpentinites (450 °C<T<650 °C and 15 kbar<P<26 kbar; González-Jiménez et al., 2017).

After burial (during which the La Cabaña ultramafic block reached depths of ~60 km), the hot ultramafic bodies were in contact with the metasedimentary host rocks within the subduction channel. We suggest that, during this time (ca. 285 Ma, Höfer

et al., 2001; Romero et al., 2017) or shortly after, the bodies were incorporated into the return flow by corner flow at the bottom of the subduction channel. Our simulations suggest that the time spent in the subduction channel was between 2–4 Ma, depending on the velocity and dip of the downgoing slab and the geometry of the subduction channel. All of the available petrological and geochemical data, and the results obtained here (i.e., dimensions of the ultramafic blocks and results of the numerical simulations), allow us to define a tectonic setting during the emplacement of the La Cabaña ultramafic bodies involving a rather steep subduction angle, a fast downgoing slab velocity (>60 mm/yr), and a wide (8–12 km) subduction channel. These values imply that the emplacement of these ultramafic blocks occurred under a relatively mature subduction system.

The rapid exhumation rate that is suggested by our simulations (20–50 mm/yr) is in good agreement with the preservation of humite minerals in the La Cabaña area (González-Jiménez et al., 2017) and the exhumation time of <40 Ma estimated by Romero et al. (2018)

2.5 Conclusions

In this contribution, we present numerical simulations of the subduction channel to explain the emplacement mechanism of partially serpentinized peridotites from the Coastal Cordillera of south-central Chile by using a slow viscous approach of the Stokes equations. The dimensions of the largest peridotite body in the La Cabaña area (Centinela Bajo Norte; Figure 2-2) were constrained by performing an UAV-

based airborne magnetic survey and subsequent inversion. The RTP magnetic map showed anomalies of >500 nT surrounded by a non-magnetized (mica schist) host rock. The inversion of the magnetic susceptibility agrees well with our in-situ measurements of magnetic susceptibility and with the magnetic susceptibilities of serpentinites reported worldwide. The ERT method confirmed vertical contacts between the serpentinized peridotite and the mica schist host rocks identified as medium-resistivity (<400 Ωm) and high-resistivity (>1000 Ωm) areas, respectively. Our numerical simulations show fast exhumation rates for peridotite blocks within the subduction channel, which can reach rates of up to 40% of the velocity of the downgoing slab and are achieved with steep subduction angles and a wide subduction channel. In contrast, slow exhumation rates or the sinking of blocks are recorded for a low slab angle and a narrow subduction channel. It follows that geometrical restrictions, i.e., the size and density of the ultramafic body, are important parameters that control the emplacement of these blocks, with larger blocks requiring relatively strong return flows achieved by a large subduction channel and steep subduction angles.

Furthermore, the serpentinization of mantle peridotites appears to be an essential process to reduce the negative buoyancy force of the block, allowing it to enter the return flow and reach the upper crust. The return flow is produced by corner flow in the subduction channel and promotes the exhumation of metasediments and serpentinized peridotites.

Overall, our models indicate that the Centinela Bajo ultramafic body in the La Cabaña area was emplaced in a mature subduction system characterized by a steep subduction angle (~60°) and a wide subduction channel (8–12 km), which resulted in fast exhumation rates (20–50 mm/yr). Our results also show that the size of an ultramafic block within an accretionary prism can be used to infer the paleotectonic setting during its emplacement within the accretionary prism

2.6 Acknowledgments

Financial Support was provided by the Iniciativa Científica Milenio (ICM) grant, “Millennium Nucleus for Metal Tracing along Subduction”. We also wish to thank GFDas SpA and DICTUC for providing the equipment for the geophysical campaigns; we especially wish to thank Giovanni Menanno for his work with the magnetometers. We are also grateful to Pablo Iturrieta for his useful tips and discussion regarding the numerical modeling. Last, but by no means least, we would like to thank Jose María González-Jiménez for his enthusiasm and early invitation to be involved in this research problem. Archive data of this study is still underway and planned to be available at Pangaea data repository, temporarily copy of the data is uploaded in the supporting information.

REFERENCES

Abers, G. A., Keken, P. E. Van, Kneller, E. A., Ferris, A., Stachnik, J. C. (2006). The thermal structure of subduction zones constrained by seismic imaging: Implications for slab dehydration and wedge flow. Earth and Planetary Science Letters, 241(3-4), 387–397. https://doi.org/10.1016/j.epsl.2005.11.055

Agard, P., Yamato, P., Jolivet, L., Burov, E. (2008). Exhumation of oceanic blueschists and eclogites in subduction zones: Timing and mechanisms. Earth Science Reviews, 92, 53-79. https://doi.org/10.1016/j.earscirev.2008.11.002

Aguirre, L., Hervé, F., Godoy, E. (1972). Distribution of Metamorphic facies in Chile, an outline. Kristalinikum, 9, 7–19.

Anderson, D.L. (1989). Theory of the Earth. Blackwell Scientific Publications, Boston, MA. ISBN 0865423350.

Angermann, D., Klotz, J., Reigber, C. (1999). Space-geodetic estimation of the Nazca-South America Euler vector. Earth and Planetary Science Letters, 171(3), 329–334. https://doi.org/10.1016/S0012-821X(99)00173-9

Angiboust, S., Wolf, S., Burov, E., Agard, P., Yamato, P. (2012). Effect of fluid circulation on subduction interface tectonic processes: Insights from thermo-mechanical numerical modelling. Earth and Planetary Science Letters, 357–358, 238–248. https://doi.org/10.1016/j.epsl.2012.09.012

Barra, F., Rabbia, O., Alfaro, G., Miller, H., Höfer, C., Kraus, S. (1998). Serpentinitas y cromititas de La Cabaña, Cordillera de la Costa, Chile central. Revista Geológica de Chile, 25, 29–44.

Barra, F., Gervilla, F., Hernández, E., Reich, M., Padrón-Navarta, J. A., González-Jiménez, J. M. (2014). Alteration patterns of chromian spinels from La Cabaña peridotite, south-central Chile. Mineralogy and Petrology, 108(6), 819–836. https://doi.org/10.1007/s00710-014-0335-5

Beaumont, C., Jamieson, R. A., Butler, J. P., Warren, C. J. (2009). Crustal structure: A key constraint on the mechanism of ultra-high-pressure rock exhumation. Earth and Planetary Science Letters, 287(1–2), 116–129. https://doi.org/10.1016/j.epsl.2009.08.001

Bonnet, G., Agard, P., Angiboust, S., Monié, P., Jentzer, M., Omrani, J., et al. (2018). Tectonic slicing and mixing processes along the subduction interface: The Sistan example (Eastern Iran). Lithos, 311, 269–287. https://doi.org/10.1016/j.lithos.2018.04.016

Cattabgriga, L. (1961). Su un problema al contorno relativo al sistema di equazioni di Stokes. Rend Sem Mat Univ. Padova, 31, 308-340.

Cloos, M., Shreve, R. L. (1988). Subduction-channel model of prism accretion, melange formation, sediment subduction, and subduction erosion at convergent plate margins: 1. Background and description. Pure and Applied Geophysics PAGEOPH, 128(3–4), 455–500. https://doi.org/10.1007/BF00874548

Collao, S., Alfaro, G., Hayashi, K. (1990). Banded Iron Formation and Massive Sulfide Orebodies, South-Central Chile: Geologic and Isotopic Aspects, Stratabound Ore Deposits in the Andes, 209-219. Berlin: Springer.

Cooperdock, E. H. G., Raia, N. H., Barnes, J. D., Stockli, D. F., Schwarzenbach, E. M. (2018). Tectonic origin of serpentinites on Syros, Greece: Geochemical signatures of abyssal origin preserved in a HP / LT subduction complex. Lithos, 296–299, 352–364. https://doi.org/10.1016/j.lithos.2017.10.020

Cuvelier, C., Segal, A., Steenhoven, A. A. (1986). Finite Element Methods and Navier-Stokes Equations. In Mathematics and its Applications. D. Reidel, Dordrecht, Boston, Lancaster, Tokyo.

Daniel, A. J., Kusznir, N. J., Styles, P. (2001). Thermal and dynamic modeling of deep subduction of a spreading center: Implications for the fate of the subducted Chile Rise, southern Chile. Journal of Geophysical Research: Solid Earth, 106(B3), 4293–4304. https://doi.org/10.1029/1998jb900028

Davies, J. H., Stevenson, D. J. (1992). Physical model of source region of subduction zone volcanics. Journal of Geophysical Research, 97(B2), 2037–2070. https://doi.org/10.1029/91JB02571

Dentith, M. and Mudge, S.T. (2014). Geophysics for the Mineral Exploration Geoscientist (2nd). Cambridge University Press.

Ernst, W. G. (1999). Metamorphism, partial preservation, and exhumation of ultrahigh-pressure belts. The Island Arc, 8(October 1998), 125–153.

Ernst, W. G. (2006). Preservation/exhumation of ultrahigh-pressure subduction complexes. Lithos, 92(3–4), 321–335. https://doi.org/10.1016/j.lithos.2006.03.049

Frost, R. B., Frost, C. D. (2013). Essentials of Igneous and Metamorphic Petrology. New York: Cambridge University Press.

Frutos, J., Alfaro, G. (1987). Metallogenic and tectonic characteristics of the paleozoic ophiolitic belt of southern Chile coastal Cordillera. Geologische Rundschau, 76, 343–356.

Gerya, T. V., Stockhert, B., Perchuk, A. L. (2002). Exhumation of high-pressure metamorphic rocks in a subduction channel: A numerical simulation. Tectonics, 21(6), 6-1-6–19. https://doi.org/10.1029/2002TC001406

Gerya, T. V, Perchuk, L. L., Reenen, D. D. Van, Smit, C. A. (2000). Two-dimensional numerical modeling of pressure ± temperature-time paths for the exhumation of some granulite facies terrains in the Precambrian. Journal of Geodynamics, 30, 17–35.

Glodny, J., Lohrmann, J., Echtler, H., Gräfe, K., Seifert, W., Collao, S., Figueroa, O. (2005). Internal dynamics of a paleoaccretionary wedge: Insights from combined isotope tectonochronology and sandbox modelling of the South-Central Chilean forearc. Earth and Planetary Science Letters, 231(1–2), 23–39. https://doi.org/10.1016/j.epsl.2004.12.014

Glodny, J., Echtler, H., Collao, S., Ardiles, M., Burón, P., Figueroa, O. (2008). Differential Late Paleozoic active margin evolution in South-Central Chile (37°S-40°S) - the Lanalhue Fault Zone. Journal of South American Earth Sciences, 26(4), 397–411. https://doi.org/10.1016/j.jsames.2008.06.001

Godoy, E. (1979). Metabasitas del basamento metamórfico. Congeso Geológico Chileno, Actas, 133–144.

González-Bonorino, F. (1971). Metamorphism of the crystalline basement of central Chile. Journal of Petrology, 12, 149–175.

González-Jiménez, J. M., Barra, F., Walker, R. J., Reich, M., Gervilla, F. (2014). Geodynamic implications of ophiolitic chromitites in the la Cabaña ultramafic bodies, Central Chile. International Geology Review, 56(12), 1466–1483. https://doi.org/10.1080/00206814.2014.947334

González-Jiménez, J. M., Barra, F., Garrido, L. N. F., Reich, M., Satsukawa, T., Romero, R., et al. (2016). A secondary precious and base metal mineralization in chromitites linked to the development of a Paleozoic accretionary complex in Central Chile. Ore Geology Reviews, 78, 14–40. https://doi.org/10.1016/j.oregeorev.2016.02.017

González-Jiménez, J. M., Plissart, G., Garrido, L. N., Padrón-Navarta, J. A., Aiglsperger, T., Romero, R., et al. (2017). Titanian clinohumite and chondrodite in antigorite serpentinites from Central Chile: evidence for deep and cold subduction. European Journal of Mineralogy, 29(6), 959–970. https://doi.org/10.1127/ejm/2017/0029-2668

Guillot, S., Hattori, K., Agard, P., Schwartz, S., Vidal, O. (2009). Exhumation processes in oceanic and continental subduction contexts: a review. In: Lallemand, S., Funiciello F. (eds.). “Subduction Zone Geodynamics”. Berlin: Springer-Verlag.

Hansen, R. O., Miyazaki, Y. (1984). Continuation of potential fields between arbitrary surfaces using equivalent source distributions. Geophysics, 49(6), 787–795. https://doi.org/10.1190/1.1826973

Hervé, F. (1988). Late paleozoic subduction and accretion in southern Chile: Episodes, 11, 183–188.

Hervé, F., Godoy, E., Del Campo, M., Ojeda, J. (1976). Las metabasitas del basamento metamórfico de Chile Central y Austal. I Congreso Geológico Chileno, Actas, 175–187.

Hilairet, N., Reynard, B., Wang, Y., Daniel, I., Merkel, S., Nishiyama, N., Sylvain, P. (2007). High-Pressure Creep of Serpentinite Interseismic Deformation, and Initiation of Subduction. Science, 318, 1910–1914.

Höfer, C., Kraus, S., Miller, H., Alfaro, G., Barra, F. (2001). Chromite-bearing serpentinite bodies within an arc-backarc metamorphic complex near La Cabaña, south Chilean Coastal Cordillera. Journal of South American Earth Sciences, 14(1), 113–126. https://doi.org/10.1016/S0895-9811(01)00011-6

Hole, M. J., Saunders, A. D., Marriner, G. F., Tarney, J., Hole, M. J., Saunders, A. D., et al. (1984). Subduction of pelagic sediments: implications for the origin of Ce-anomalous basalts from the Mariana Islands Subduction of pelagic sediments: implications for the origin Ce-anomalous basalts from the Mariana Islands. Journal of Geological Society of London, 141, 453–472. https://doi.org/10.1144/gsjgs.141.3.0453

Hull, D, Rimmer, D. E. (1959). The growth of grain-boundary voids under stress. Philosophical Magazine, 4, 673–687.

Hyndman, R. D., Peacock, S. M. (2003). Serpentinization of the forearc mantle. Earth and Planetary Science Letters, 212, 417-432. https://doi.org/10.1016/S0012-821X(03)00263-2

Kellogg, O.D. (1953). Foundations of Potential Theory. New York. Dover Publications.

Karato, S. I., Jung, H. (2003). Effects of pressure on high-temperature dislocation creep in olivine. Philosophical Magazine, 83(3), 401–414. https://doi.org/10.1080/0141861021000025829

Lai, S. C., Qin, J. F., Long, X. P., Li, Y. F., Ju, Y. J., Zhu, R. Z., et al. (2017). Neoproterozoic gabbro–granite association from the Micangshan area, northern Yangtze Block: Implication for crustal growth in an active continental margin. Geological Journal, 53(6), 2471–2486. https://doi.org/10.1002/gj.3082

Lallemand, S. (1999). La Subduction Oceanique. Newark, N.J.: Gordon and Breach.

Li, Y., Oldenburg, D. W. (1996). 3-D inversion of magnetic data. Geophysics, 61(2), 394–408. https://doi.org/10.1190/1.1443968

Lin, S.-C. (2014). Three-dimensional mantle circulations and lateral slab deformation in the southern Chilean subduction zone. Journal of Geophysical Research: Solid Earth, 119, 3879–3896. https://doi.org/10.1002/2013JB010864.Received

Matthews, K. J., Maloney, K. T., Zahirovic, S., Williams, S. E., Seton, M., Müller, R. D. (2016). Global plate boundary evolution and kinematics since the late Paleozoic. Global and Planetary Change, 146, 226–250. https://doi.org/10.1016/j.gloplacha.2016.10.002

Melnick, D., Echtler, H. (2006). Inversion of forearc basins in South-Central Chile caused by rapid glacial age trench fill. Geology, 34(9), 709–712.

Mpodozis, C., Ramos, V. A. (1989). The Andes of Chile and Argentina, in: Geology of the Andes and its Relation to Hydrocarbon and Mineral Resources. Earth Sciencies Series, 11, 59–90.

Pardo, M., Monfret, T., Vera, E., Eisenberg, A., Yáñez, G., Triep, E. (2003). Cambio en la subducción de la placa de Nazca, de plana a inclinada, bajo Chile central y Argentina: Datos Sismológicos preliminares. Presented at X Congreso Geológico Chileno.

Peacock, S.M. (1996). Thermal and petrologic structure of subduction zones, in Subduction: *Top to Bottom*. Geophysical Monograph Series, 96, 119-133.

Pilkington, M., Boulanger, O. (2017). Potential field continuation between arbitrary surfaces — Comparing methods. Geophysics, 82(3), J9–J25. https://doi.org/10.1190/geo2016-0210.1

Plissart, G., González-Jiménez, J. M., Garrido, L. N. F., Colás, V., Berger, J., Monnier, C., et al. (2019). Tectono-metamorphic evolution of subduction channel serpentinites from South-Central Chile. Lithos, 336–337, 221–241. https://doi.org/10.1016/j.lithos.2019.03.023

Ranalli, G. (1995). Rheology of the Earth (2nd ed.). New York: Chapman and Hall.

Ring, U., Brandon, M. T., Willett, S. D., Gordon, S. (1999). Exhumation processes: Normal Faulting, Ductile Flow and Erosion. Geological Society, London, Special Publications, 154, 1–27. https://doi.org/10.1144/GSL.SP.1999.154.01.01

Romero, R., González-jiménez, J. M., Barra, F., Leisen, M., Garrido, L. N., Talavera, C., et al. (2018). Timing the tectonic mingling of ultramafic rocks and metasediments in the

southern section of the coastal accretionary complex of central Chile. International Geology Review, 60(16), 2031–2045. https://doi.org/10.1080/00206814.2017.1402377

Romero, R., Barra, F., Leisen, M., Salazar, E., González-Jiménez, J. M., Reich, M. (2019). Sedimentary provenance of the Late Paleozoic metamorphic basement, south-central Chile: Implications for the evolution of the western margin of Gondwana. International Geology Review, 60, 1-16. https://doi.org/10.1080/00206814.2019.1627589

Satsukawa, T., Piazolo, S., González-Jiménez, J. M., Colás, V., Griffin, W. L., O'Reilly, S. Y., et al. (2015). Fluid-present deformation aids chemical modification of chromite: Insights from chromites from Golyamo Kamenyane, SE Bulgaria. Lithos, 228–229, 78–89. https://doi.org/10.1016/j.lithos.2015.04.020

Schubert, G. (2015). Treatise on Geophysics. Elsevier Science.

Sharma, S., Verma, G. K. (2015). Inversion of Electrical Resistivity Data: A Review. World Academy of Science, Engineering and Technology, International Journal of Environmental, Chemical, Ecological, Geological and Geophysical Engineering, 9(4), 400–406.

Shea, W. T., Kronenberg, A. K. (1992). Rheology and deformation mechanisms of an isotropic mica schist. Journal of Geophysical Research, 97(B11), 15201. https://doi.org/10.1029/92jb00620

Shreve, R. L., Cloos, M. (1986). Dynamics of sediment subduction, melange formation, and prism accretion. Journal of Geophysical Research, 91(B10), 10229. https://doi.org/10.1029/jb091ib10p10229

Sillitoe, R. (1977). Permo-Carboniferous, upper Cretaceous and Miocene porphyry copper type mineralization in the Argentinian Andes. Economic Geology, 72, 99–103.
Stern, R. J. (2002). Subduction zones. Reviews of Geophysics, 40(2), 1012. https://doi.org/10.1029/2001RG000108

Stesky, R. M., Brace, W. F. (1973). Electrical conducticity of serpentinized rocks to 6 Kilobars. Journal of Geophysical Research, 78, 7614–7621.

Telford, W. M., Sheriff, R. E. (1990). Applied Geophysics 2nd Edition. Cambridge: Cambridge University Press.

Turcotte, D., Schubert, G. (2014). Geodynamics: Applications of Continuum Physics to Geological Problems (3rd ed.). Hoboken, N.J.: John Wiley.

von Huene, R. Scholl, D.W. (1991). Observations at convergent margins concerning sediment subduction, subduction erosion, and the growth of continental crust. Reviews of Geophysics, 29, 279-316.

Wang, Y., Zhang, L. F., Li, Z. H., Li, Q. Y., Bader, T. (2019). The Exhumation of Subducted Oceanic-Derived Eclogites: Insights from Phase Equilibrium and Thermomechanical Modeling. Tectonics, 1764–1797. https://doi.org/10.1029/2018TC005349

White, J. C., Beamish, D. (2014). A lithological assessment of the resistivity data acquired during the airborne geophysical survey of Anglesey, North Wales. Proceedings of the Geologists' Association, 125(2), 170–181. https://doi.org/10.1016/j.pgeola.2014.01.003

Willner. (2005). Pressure-temperature evolution of a late palaeozoic paired metamorphic belt in north-central Chile (34°-35° 30' S). Journal of Petrology, 46, 1805–1833.

Willner, A. P., Thomson, S. N., Kröner, A., Wartho, J. A., Wijbrans, J. R., Hervé, F. (2005). Time markers for the evolution and exhumation history of a Late Palaeozoic paired metamorphic belt in North-Central Chile (34°-35°30′S). Journal of Petrology, 46(9), 1835–1858. https://doi.org/10.1093/petrology/egi036

Yañez, G., Ugalde, H., Vargas, J. A. (2017). Topographic correction of magnetic data on rugged topography with application to Rió Blanco-Los Bronces and El Teniente porphyry copper districts, Southern Andes, Chile. Exploration Geophysics, 49(4), 595–607. https://doi.org/10.1071/EG17016

Yáñez, G., Cembrano, J. (2004). Role of viscous plate coupling in the late Tertiary Andean tectonics. Journal of Geophysical Research, 109(B2), 1–21. https://doi.org/10.1029/2003JB002494

A P P E N D I X

APPENDIX A: MAGNETIC METHOD THEORY AND INVERSION

A.1 Theory, magnetization in rocks

Magnetic anomalies among the Earth are caused by several sources, for this geophysical method the main scope is to measure and understand how geological sources produce these anomalies. Magnetization in rocks depend on two main features: the Earth's magnetic field and the kind of magnetization.

The strength of the Earth's magnetic field, which is associated with the Earth's core, is calculated using spherical harmonic analysis of the Laplace's equation and is called the International Geomagnetic Reference Field (IGRF) (Blakely, 1995). The IGRF is a vector field and can be described through three parameters for a given area: the total magnetic intensity (TMI), inclination (I) and declination (D), the spatial correlation is displayed in Figure A-1.

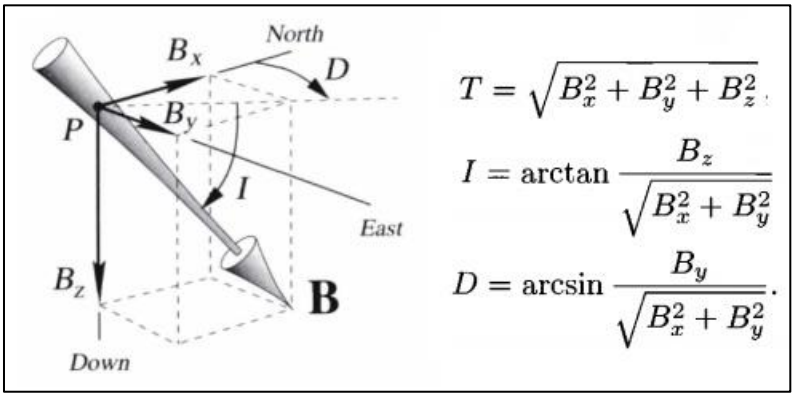

Figure A-1: Representation of the three components of an external field (B) in the cartesian coordinate system, including the total magnetic intensity, inclination and declination of the vector B (Modified from Blakely, 1995).

Rocks can acquire a component of magnetization in the presence of the Earth's magnetic field. This component will depend exclusively on the kind of magnetization that a certain rock has and the components of the IGRF.

The magnetic properties of a certain material are determined by the interaction of the electron spins and how they react to an external field. They can be classified into three distinct types of magnetism: diamagnetism, paramagnetism, ferromagnetism, which are reflected in the magnetic susceptibility of the material κ. Another type of magnetization is the remanent, which is associated to a thermoremanet magnetization, acquiring the Earth's magnetic field of a certain time, used for paleomagnetic studies. Ferromagnetism is millions of times stronger than the other kinds of magnetization (Dentith and Mudge, 2014) and will be further explained here.

Ferrimagnetism can be understood as a series of dipoles within a material or rock. Without an external field, they are aligned randomly acquiring their intrinsic magnetism, being diamagnetic (negative) or paramagnetic (positive) with very low amplitude. In the presence of the Earth's magnetic field, the dipoles align depending on the TMI, inclination and declination of the area, leading to a net magnetism of the material as a whole by induction (Dentith and Mudge, 2014). The induction magnitude correlates with the magnetic susceptibility of the material expressed as:

$$\boldsymbol{M_i} = \kappa \boldsymbol{H}$$

Where κ is a proportionality constant called magnetic susceptibility. $\boldsymbol{H}$ is an external magnetic field and $\boldsymbol{M_i}$ the induced magnetization of a certain material.

In a practical way, κ represent the complex link between atomic and macroscopic properties of the magnetic material. The magnetic susceptibility is generated by ferromagnetic materials and they include three kind of ferromagnetic materials: ferromagnetism, antiferromagnetism and ferrimagnetism. Ferromagnetism property is when the atomic moments within a body are aligned parallel to the external field ($\kappa > 0$). Antiferromagnetism is when the atomic moments are aligned antiparallel and cancel one another ($\kappa \approx 0$). Ferrimagnetism is similar to antiferromagnetism, but the atomic moments do not cancel each other ($\kappa < 0$) (Blakely, 1995).

In this sense, rocks with abundant ferromagnetism minerals, generate the largest induced and remanent magnetization that generate magnetic anomalies, depending on the geometry and magnetization, their amplitudes can vary from a few nT to 1000 nT.

A.2 Magnetic anomaly of a sphere

To understand how magnetic anomalies are present in geology, first a general background on how the TMI, inclination and declination determine the nature of a magnetic anomaly. Later, for a given TMI, inclination and declination, the magnetization (assuming for this example induced magnetization only) and the observation distance will be explored to see how they affect to the amplitude and wavelength of the magnetic anomaly.

For testing purposes, the magnetic field of an induced sphere is used (Blakely, 1995):

$$M = \kappa H \overbrace{\frac{4}{3}\pi a^3}^{Volume} \frac{\partial^2}{\partial \alpha^2}\frac{1}{r}$$

Where κ is the magnetic susceptibility, H the external field's magnitude (in this case the TMI), a the sphere's radius, r the distance relative to an observation point and α the direction of magnetization (related to the inclination and declination of the IGRF). Here we assume that $a = 50m$ and the sphere is buried $-100m$ from the surface level set at 0 meters.

Through calculations of the Earth's magnetic field, the TMI varies from 65,000 nT in the magnetic poles to 20,000 nT in the equator near South America, this will only determine the amplitude of the magnetic anomaly of a certain area. The declination also has no effect in the shape of the anomaly, but it rotates clockwise or counterclockwise depending on the north's direction. The inclination varies from 0° in the magnetic equator (near the geographic) to -90° and 90° around the geomagnetic poles, located near the geographic south and north pole respectively, this parameter has a high impact on the shape of the magnetic anomaly as seen in Figure A-2.

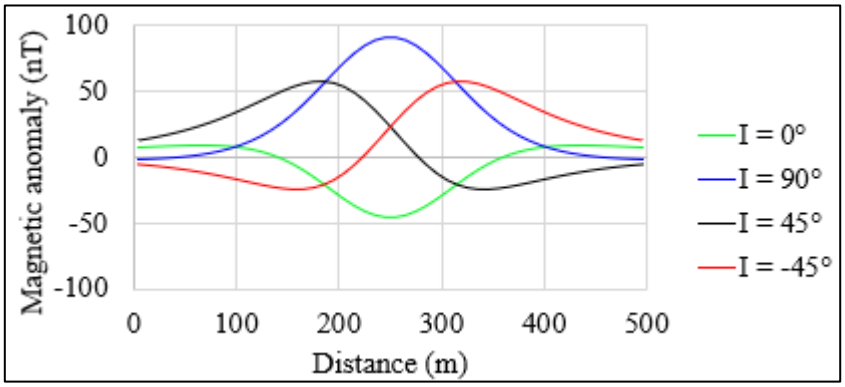

Figure A-2: Polarity of the magnetic field of a sphere with a=50m buried -100m from the surface for different inclinations I. Data is calculated with TMI=20,000 nT, D=0°, κ=0.1 SI at surface level.

For the north or south pole $(90°, -90°)$ the anomaly is positive and monopolar (blue profile in Figure A-2), meanwhile in the magnetic equator is negative and monopolar (green profile in Figure A-2). In contrast, for the rest of the world, magnetic anomalies are dipolar. For the south geographic hemisphere (near Chile), there are negative inclinations and the shape is similar to the red profile in Figure A-2 Opposite effect is generated in the north hemisphere (black profile in Figure A-2).

The magnetic susceptibility will change the magnetic anomaly's amplitude as seen in Figure A-3.

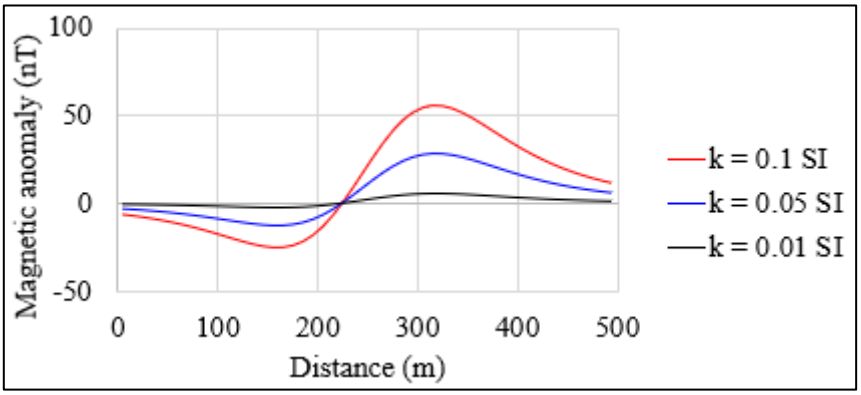

Figure A-3: Amplitude of the magnetic field of a sphere with a=50m buried -100m from the surface for different magnetic susceptibility κ. Data is calculated with TMI=20,000 nT, D=0°, I=-45° at surface level.

For high magnetic susceptibility (high iron content) the magnetic anomaly has higher amplitude, meanwhile low iron content generates lower magnitudes.

The last parameter to explore is the observation distance, which is displayed in Figure A-4.

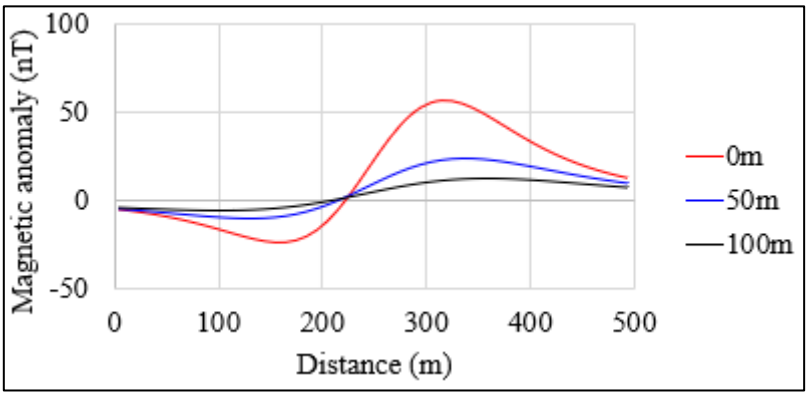

Figure A-4: Decay of the magnetic field by distance of a a sphere with $a = 50m$ buried $-100m$ from the surface for different observation points. Data is calculated with $TMI = 20{,}000\ nT$, $D = 0°$, $I = -45°$ and $\kappa = 0.1\ SI$

For larger distance to the source, the magnetic field widens its wavelength and lowers its amplitude. The decay of the amplitude is related to $1/r^3$ associated with the theorical magnetic field given for the sphere (double derivative of 1/r gives a decay of $1/r^3$). So, when the observation point is near the source, the amplitude is higher and the wavelength is shorter, the opposite holds for a far observation point.

A.3 Inversion procedure and further results

The data inversion is carried out using the software MAG3D (developed by the University of British Columbia-Geophysical Inversion Facility's – UBC GIF; Li and Oldenburg, 1996).

The input data for the inversion are: (1) the previously corrected and continued data to an arbitrary surface parallel to the topography with a 200m of clearance altitude. (2) The topography file for every data point. (3) The mesh parameters for the 3D geometry. The first two are already available while the third is generated using the software's manual.

The mesh generation is done considering a core mesh beneath the data with the same horizontal resolution (50m) and 3 additional rows of larger padding cells on the sides to avoid noisy artifacts in the inversion around the boundaries. The following criteria is also applied in depth, where the depth resolution is halved (25m) and there is also padding cells at the bottom of the model. The mesh resolution and padding cells are schematized in Figure A-5.

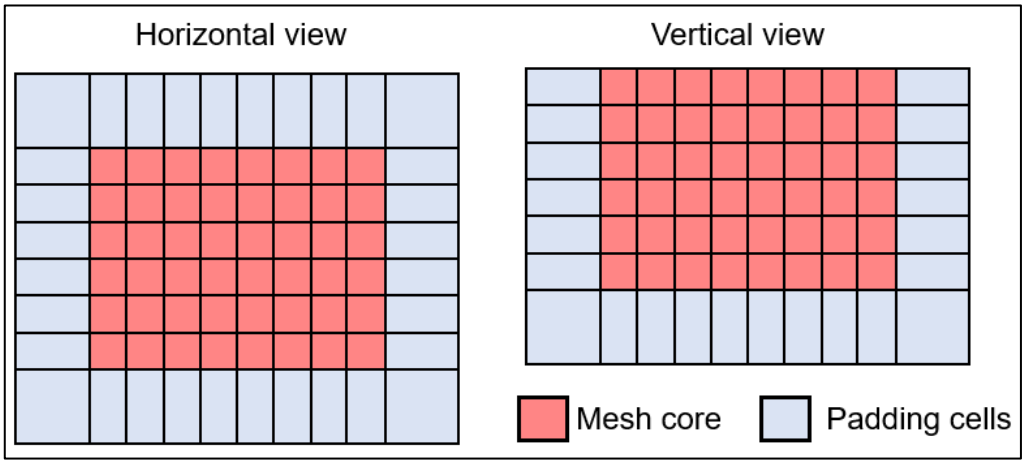

Figure A-5: Schematic model of the mesh core and padding cells.

With the 3 input files done, several parameters for the inversions are needed: (1) depth weighting, (2) reference model and (3) susceptibility bounds. The first one was set to $\beta = 0; z_0 = 0$ which represent a cubic decay of the magnetic anomaly in depth, this approach is used to avoid that the inverted susceptibility is only located near the surface. The second one was set to 0.001 SI which is the mean value for the magnetic susceptibility of the host rocks, used to guide the inversion objective function to a smooth solution around this value. The last one is the most important for our case study because it represents the geology domains producing the magnetic anomaly. In this manner, we tested 2 scenarios for the magnetic susceptibility bounds: (1) no bounds and (2) bounded with in-situ measurements of this parameter (minimum 0.001 SI and maximum 0.15 SI).

Since the inversion is carried out with a continuum change of the magnetic susceptibility. It was necessary to discretize the inversion to recognize without ambiguity the geometry of the magnetized body. In order to do so, we used the

bounded inversion and we assigned 3 magnetic susceptibility values: 0.001 SI (non-magnetized host rocks), 0.03 SI (mildly magnetized) and 0.09 SI (high magnetized). These values were tested for several scenarios and were chosen considering the minimum misfit with the observed data set.

For comparison purposes, three inverted figures will be shown for every section: (1) unbounded, (2) bounded and (3) discrete with the same color scale. But first, the reduction to the pole anomaly map with the location of every section is displayed in Figure A-6. The reduction to the pole stands for the procedure in which a dipolar anomaly (with known inclination and declination) is converted to a monopolar anomaly with inclination 90° and declination 0° (see Figure A-2) using the Fourier transform (Telford and Sheriff, 1990)

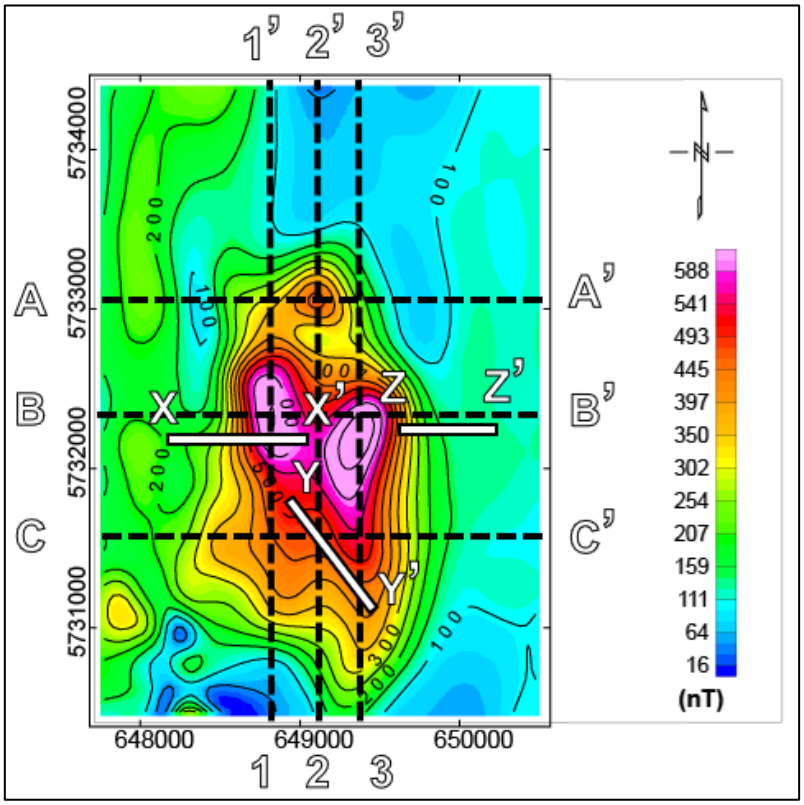

Figure A-6: Reduction to the magnetic pole anomaly after data reduction and continuation. Sections 1, 2 and 3 represent NS magnetic inversions and A, B and C EW magnetic inversions. Sections X, Y and Z are the ERT survey location. Contour every 50 nT.

Sections A, B and C are presented in Figure A-7, A-8 and A-9, corresponding to the EW sections. Meanwhile, Sections 1, 2 and 3 are presented in Figure A-10, A-11 and A-12, corresponding to the NS sections. Overall, the magnetized body is successfully mapped with this method. This kilometer size body is from 2 to 3 kilometers long and 1 to 1.5 km wide, the deepest depth reached is about 1.5 km from the surface level. Also, the magnetic susceptibility inverted is in good

agreement with surface measurements, bounds applied to the inversion procedure and serpentinites reported worldwide.

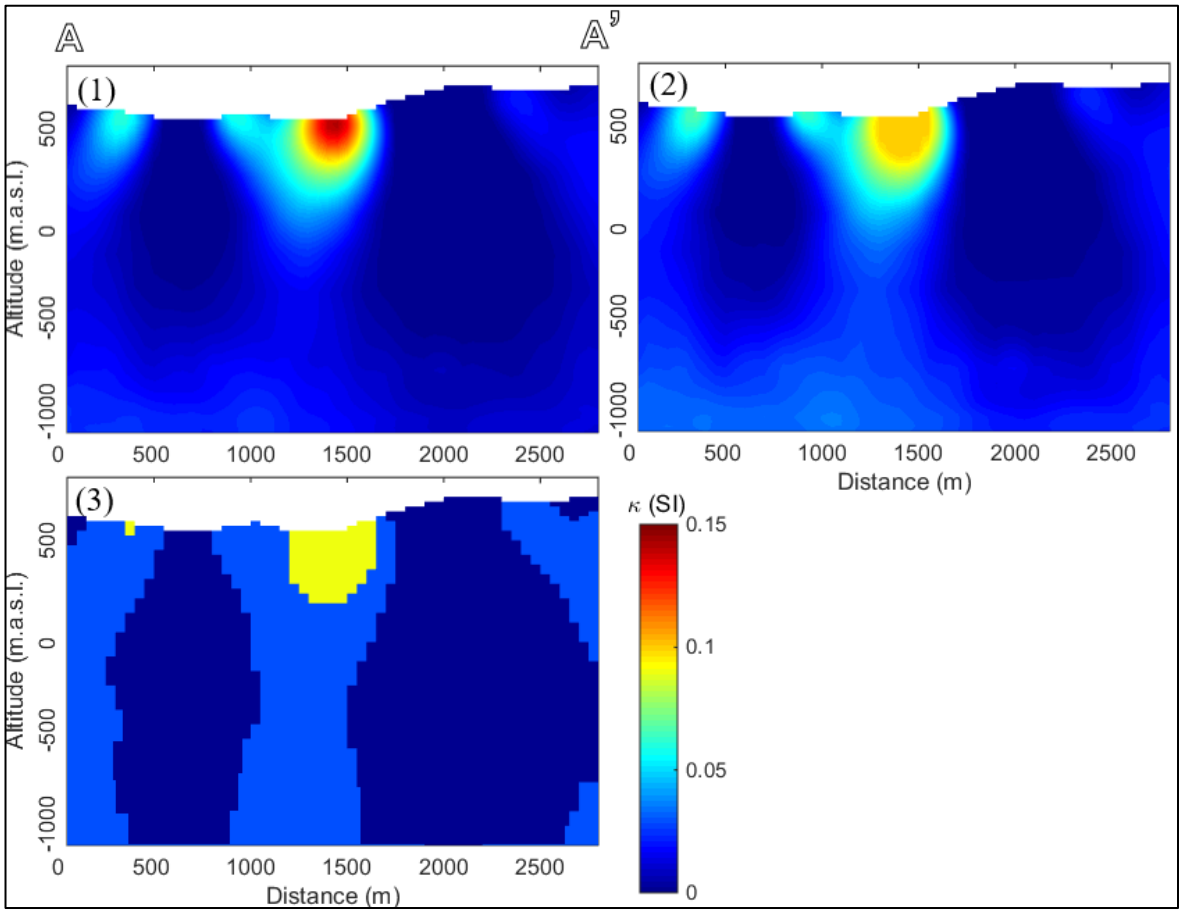

Figure A-7: Inverted magnetic susceptibility of section A-A' (see Figure A-6). (1) Unbounded, (2) bounded and (3) discrete, all the figures have the same color map and scale 1:1.

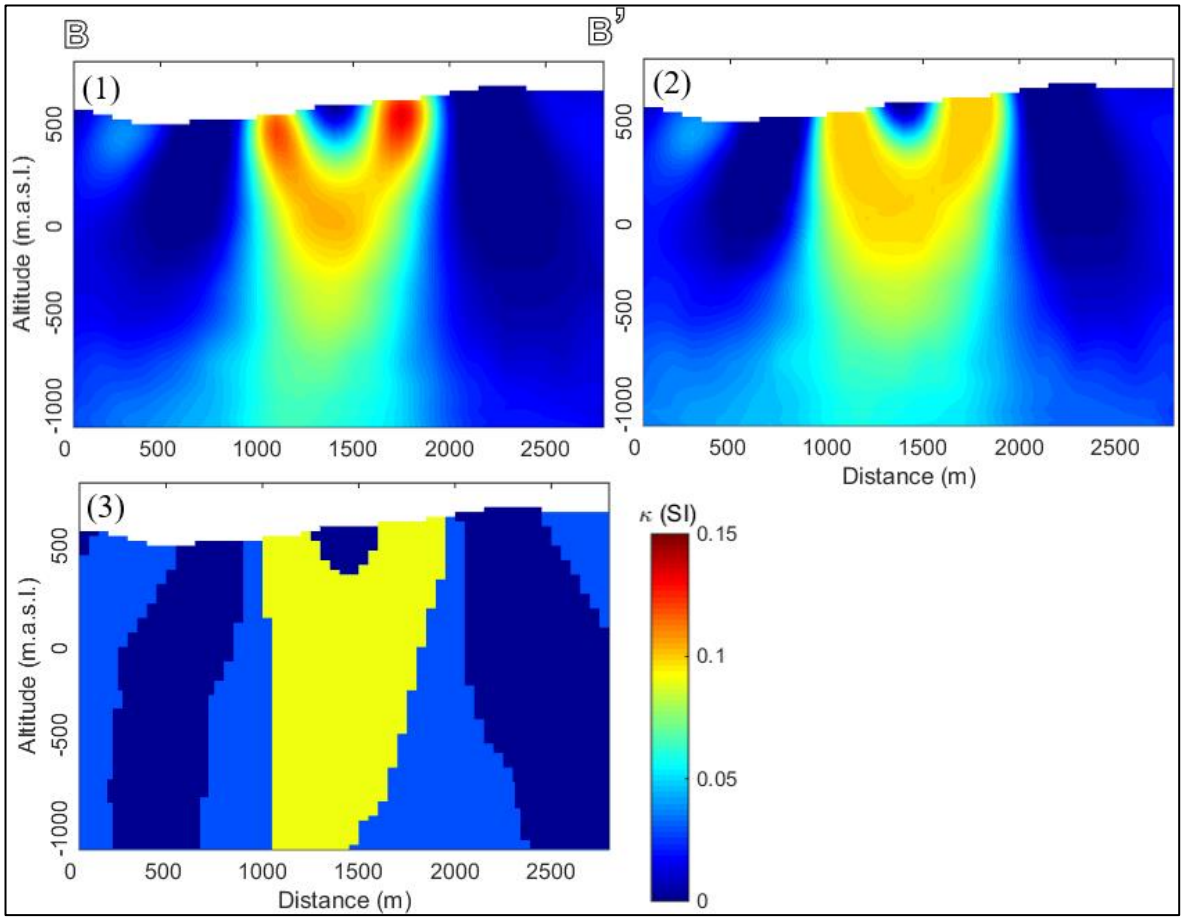

Figure A-8: Inverted magnetic susceptibility of section B-B' (see Figure A-6). (1) Unbounded, (2) bounded and (3) discrete, all the figures have the same color map and scale 1:1.

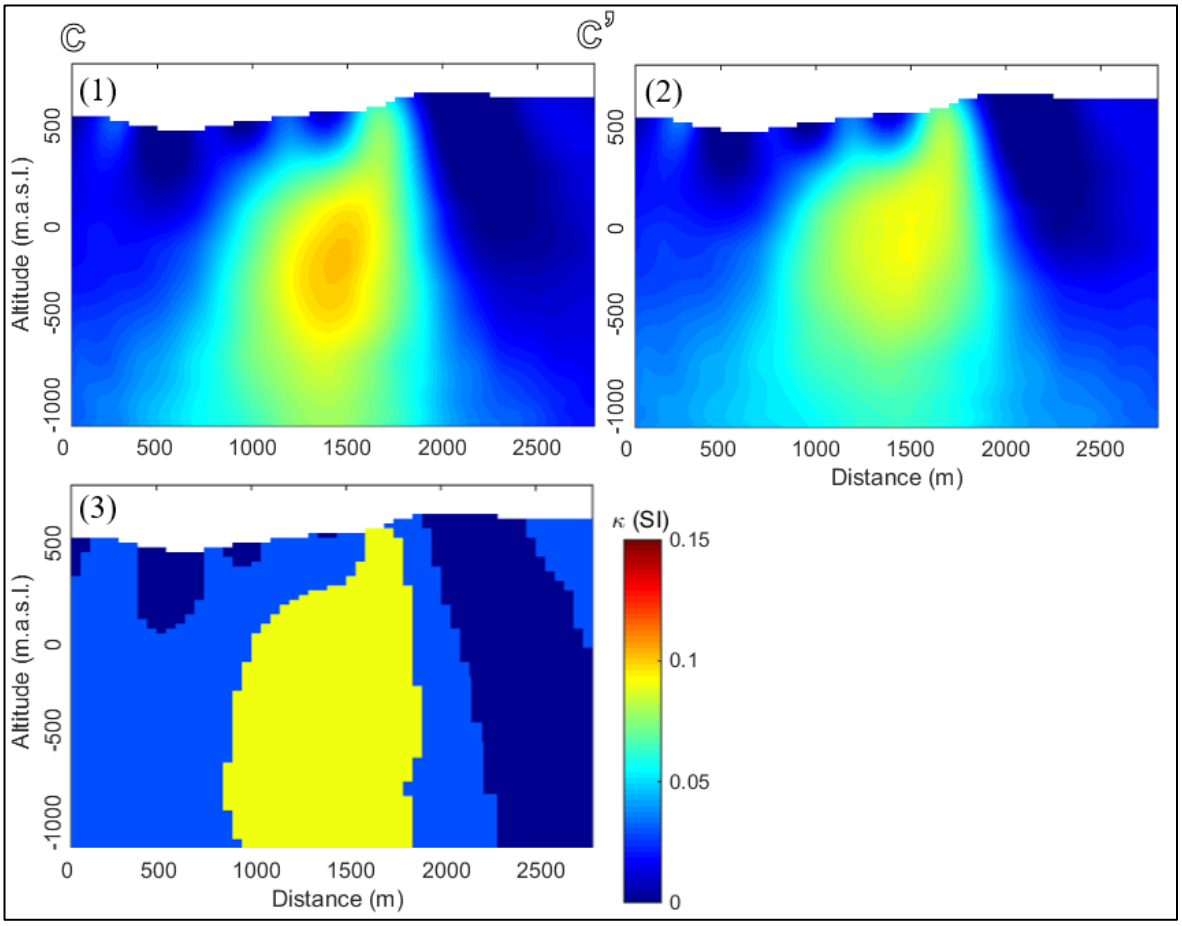

Figure A-9: Inverted magnetic susceptibility of section C-C' (see Figure A-6). (1) Unbounded, (2) bounded and (3) discrete, all the figures have the same color map and scale 1:1.

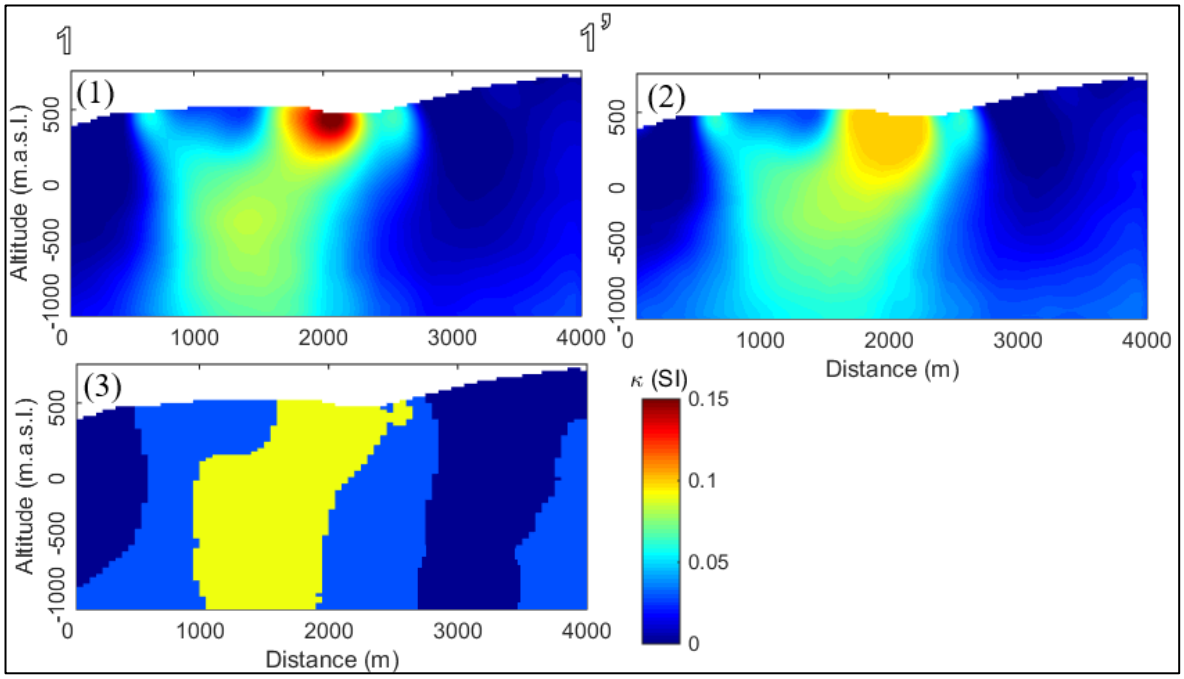

Figure A.10: Inverted magnetic susceptibility of section 1-1' (see Figure A-6). (1) Unbounded, (2) bounded and (3) discrete, all the figures have the same color map and scale 1:1.

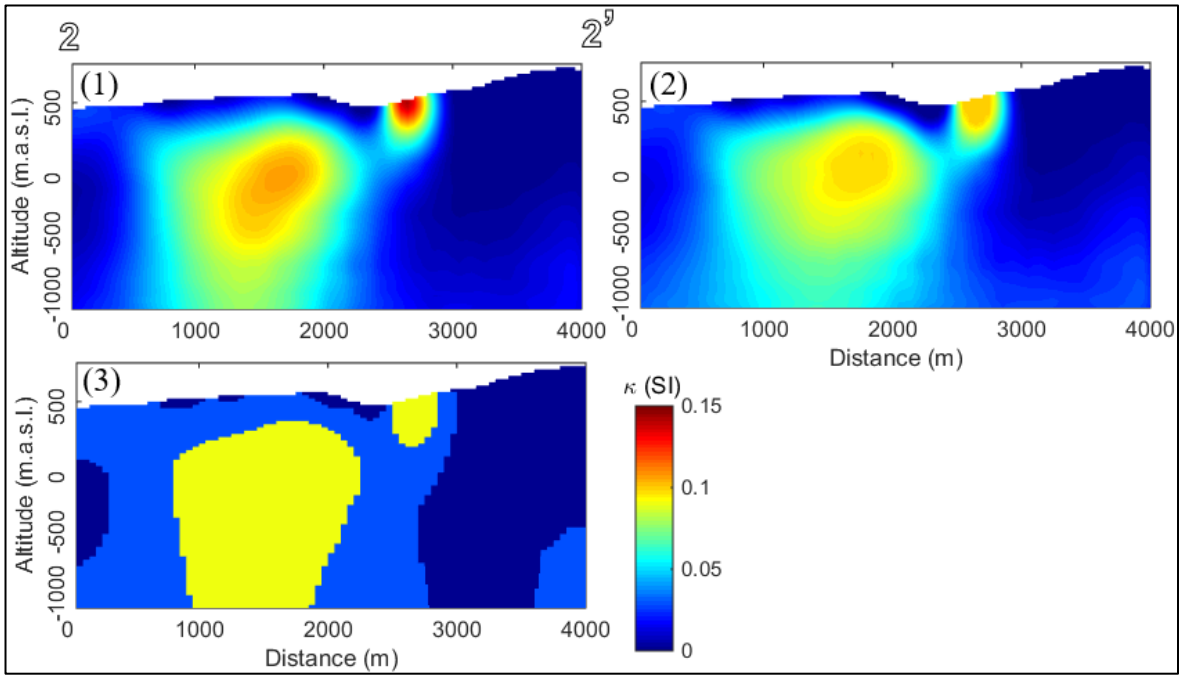

Figure A.11: Inverted magnetic susceptibility of section 2-2' (see Figure A-6). (1) Unbounded, (2) bounded and (3) discrete, all the figures have the same color map and scale 1:1

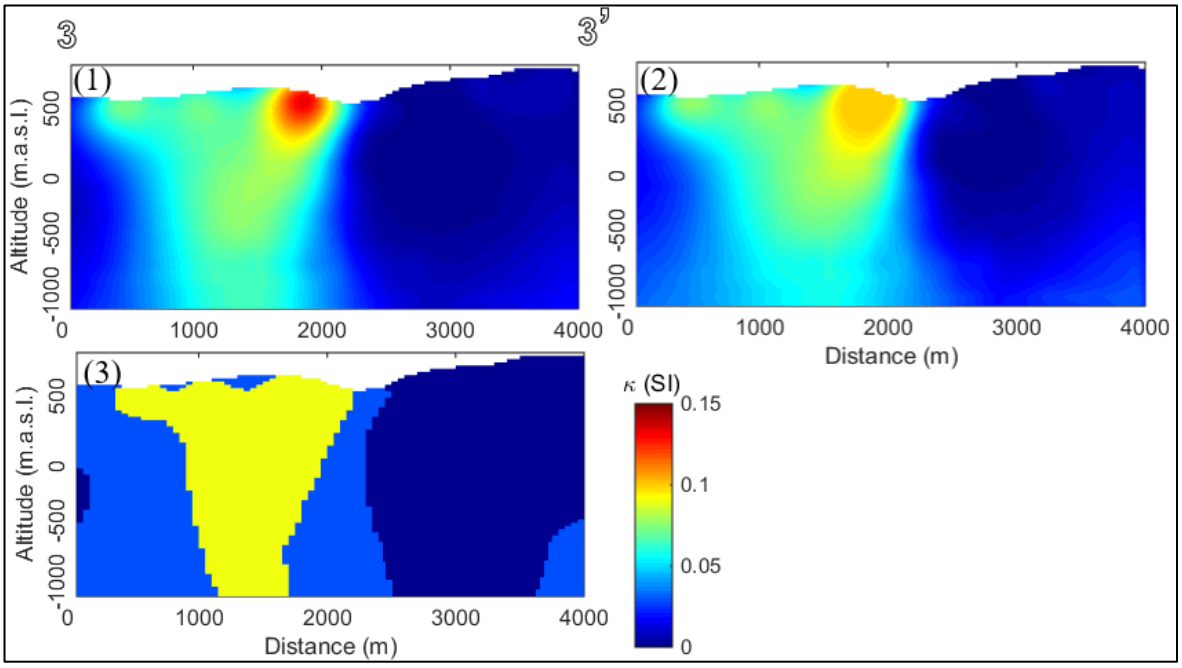

Figure A.12: Inverted magnetic susceptibility of section 3-3' (see Figure A-6). (1) Unbounded, (2) bounded and (3) discrete, all the figures have the same color map and scale 1:1.

APPENDIX B: CONTINUATION OF POTENTIAL DATA THROUGH A MAGNETIZED DIPOLE LAYER

Magnetic data measured with variable observation distance from the source generate distorted data. A good example is found in Appendix A.2 where in Figure A-4 show how the observation distance change the amplitude and wavelength of the magnetic anomaly. Thus, if we do not control this parameter, we can measure data with different observation distance along the same profile.

In particular, geophysical experiments performed in this thesis, UAV airborne magnetic data was acquired along 2 flat barometric altitudes, having a variable observation distance for every profile. In order to reduce the topographic distortion, continuation algorithms are necessary to calculate the magnetic anomaly with a common distance parallel to the topography.

There are two classic approach to achieve this: (1) based on potential field and (2) through the calculation of an equivalent dipole layer. The first one is a direct process from an input surface to a desired one. In contrast, the second one requires an indirect calculation which is the equivalent dipole layer in order to obtain the anomaly to an arbitrary surface.

According to Pilkington and Boulanger (2017), the most accurate one, but not the most efficient, is the algorithm proposed by Hansen and Miyazaki (1984) based on the calculation of an equivalent dipole layer.

In this appendix, the theory of the algorithm proposed by Hansen and Miyazaki (1984) will be described, explaining the iterative method and it will be tested with synthetic data. Finally, the algorithm will be used on the acquired data at La Cabaña test site.

B.1 Theory

For a given potential data denoted as $\psi(\alpha,\beta,\gamma)$ where (α,β,γ) are the spatial coordinates and the altitude is given by $\gamma(\alpha,\beta)$. Thus, for every pair of coordinates (α,β) the altitude $\gamma(\alpha,\beta)$ and the potential data $\psi(\alpha,\beta,\gamma(\alpha,\beta))$ is known. This surface data set is denoted as the surface E.

The equivalent dipole layer requires the calculation of a surface D of dipoles with coordinates (ξ,η,ζ) where also the altitude is known and given by $\zeta(\xi,\eta)$. The position of this surface will be chosen efficiently to minimize most of the calculations, but in theory it can be placed below the surface E only if there are no sources between D and E.

For the particular case of magnetic data (for gravimetric the reader is referred to Hansen and Miyazaki, 1984). The magnetization of the dipole layer, denoted as $\vec{\mu}$ forming the surface D generates a magnetic field ϕ calculated as a magnetized shell (Kellogg, 1929):

$$\phi(x,y,z) = \frac{1}{2\pi}\iint_{D}\frac{\vec{\mu}(\xi,\eta)\cdot\vec{r}}{r^3}\,dS$$

Where: $\vec{r} = (x-\xi, y-\eta, z-\zeta)$ and $r = |\,\vec{r}\,|$ from an observation point (x,y,z) which is the desired continued surface C.

This expression, first obtained by Kellogg (1929) and further developed by Hansen and Miyazaki (1984), represent the magnetic field for a double density dipole distribution $\vec{\mu}$ along the surface D.

In order to perform the continuation algorithm, first we need to find $\vec{\mu}$ that satisfy:

$$\phi(\alpha, \beta, \gamma) = \psi(\alpha, \beta, \gamma)$$

Which vanishes at infinity

$$\lim_{\gamma \to \infty} \phi(\alpha, \beta, \gamma) = 0$$

Finally, the potential field calculated ϕ must satisfy the Laplace equation over the surface D (Kellog, 1929):

$$\nabla^2 \phi = 0$$

These three conditions pose a Dirichlet problem in which the existence and uniqueness is achieved over the surface D where is able to find a minimum for the Dirichlet integral over this area (Kellogg, 1929).

For potential data, the last two conditions are always satisfied, where the first is reordered as:

$$\frac{1}{2\pi} \iint_D \frac{\vec{\mu}(\xi, \eta) \cdot \vec{r}}{r^3} dS = \psi(\alpha, \beta)$$

This equation is a Fredholm integral equation of first kind for $\vec{\mu}$. The above equation has complexes existence and uniqueness conditions, which can be greatly simplified by correctly choosing the position and decomposing the dipole surface D.

The dipole surface can be decomposed with a magnitude and a direction for every dipole:

$$\vec{\mu}(\xi,\eta) = \mu(\xi,\eta)\vec{v}(\xi,\eta)$$

Where $\vec{v}(\xi,\eta)$ is the orientation for every dipole in D.

In this scenario, the magnetization magnitude $\mu(\xi,\eta)$ is a scalar field and the only variable if we previously choose the dipole orientation. In this manner, the surface D is placed exactly below the surface E ($(\alpha,\beta) = (\xi,\eta)$). However, the continued surface C must be placed between D and E (Figure B-1) and the magnetization vector must be normal $\vec{n}$ to the surface D for every dipole.

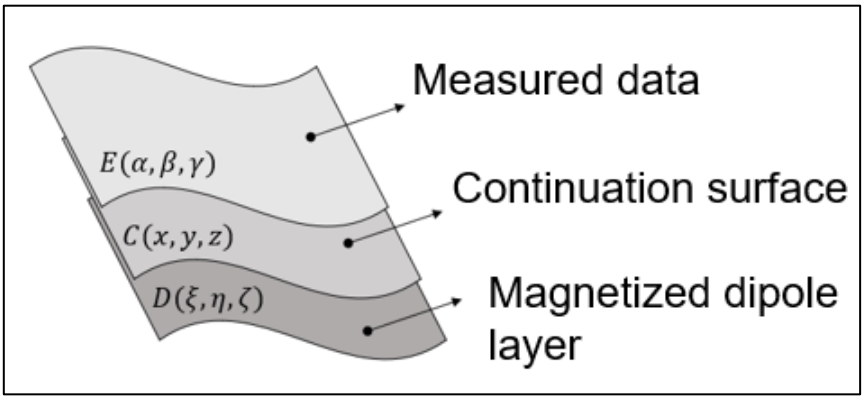

Figure B-1: Schematic positions of the surfaces E, C, D for optimum conditions to perform the continuation algorithm of Hansen and Miyazaki (1984).

Rewriting the integral equation with this decomposition:

$$\frac{1}{2\pi}\iint_D \frac{\mu(\xi,\eta)\vec{v}(\xi,\eta)\cdot\vec{r}}{r^3}\,dS = \frac{1}{2\pi}\iint_D \frac{\mu(\xi,\eta)\vec{v}(\xi,\eta)\cdot\vec{r}}{r^3}\frac{d\xi d\eta}{n_\zeta(\xi,\eta)}$$

Where $n_\zeta(\xi,\eta)$ is the direction cosine along a normal direction of D (Kellogg, 1929)

$$n_\zeta(\xi,\eta) = \left[1 + \left(\frac{\partial\zeta}{\partial\xi}\right)^2 + \left(\frac{\partial\zeta}{\partial\eta}\right)^2\right]^{-1/2}$$

For a discrete data set equally spaced δ as an array

$$\frac{1}{2\pi}\sum_j\sum_i \frac{\mu(\xi_i,\eta_j)\vec{v}(\xi_i,\eta_j)\cdot\vec{r}}{r^3}\,\frac{\delta^2}{n_\zeta(\xi_i,\eta_j)}$$

For every cell in the array, the magnetization and the direction of the dipole is assumed constant. In this array configuration, the dipole layer is approximated as a surface of cells with known parameters of position (ξ,η), altitude $\zeta(\xi,\eta)$ and direction $\vec{v}(\xi,\eta)$. Under this approximation, the later expression is:

$$\frac{1}{2\pi}\sum_j\sum_i \mu(\xi_i,\eta_j)\underbrace{\int_{\eta_j-\delta}^{\eta_j+\delta}\int_{\xi_i-\delta}^{\xi_i+\delta}\frac{\vec{v}(\xi_i,\eta_j)\cdot\vec{r}}{r^3}\frac{d\xi d\eta}{n_\zeta(\xi,\eta)}}_{I(\xi_i,\eta_j)}$$

Where the integral $I(\xi_i,\eta_j)$ is exactly solved by Hansen and Miyazaki (1984), where the calculation is simplified by choosing $\vec{v}(\xi_i,\eta_j) = \vec{n}(\xi_i,\eta_j)$.

For the exact expression of the integral, first we define the following parameters:

$$\Delta x_i = x - \xi_i$$

$$\Delta y_j = y - \eta_j$$

$$\Delta z_{ij} = z - \zeta(\xi_i,\eta_j)$$

$$\Delta\xi_i = \xi - \xi_i$$

$$\Delta\eta_j = \eta - \eta_j$$

$$a_{ij} = \frac{\partial\zeta}{\partial\xi}(\xi_i,\eta_j)$$

$$b_{ij} = \frac{\partial \zeta}{\partial \eta}(\xi_i, \eta_j)$$

Derivatives terms a_{ij}, b_{ij} are calculated using splines for the altitude data ζ. Finally,

$$I(\xi_i, \eta_j)$$

$$= arctan\left\{\frac{\left(1 + a_{ij}^2 + b_{ij}^2\right)(\Delta x_i - \Delta\xi_i)(\Delta y_j - \Delta\eta_j)}{\Delta z_{ij} - a_{ij}\Delta x_i - b_{ij}\Delta y_j} + b_{ij}(\Delta x_i - \Delta\xi_i) + a_{ij}(\Delta y_j - \Delta\eta_j)}{\left[(\Delta x_i - \Delta\xi_i)^2 + \left(\Delta y_j - \Delta\eta_j\right)^2 + \left(\Delta z_{ij} - a_{ij}\Delta x_i - b_{ij}\Delta y_j\right)^2\right]^{1/2}}\right\}\Bigg|_{\Delta\xi_i=-\delta/2}^{\Delta\xi_i=\delta/2}\Bigg|_{\Delta\eta_j=-\delta/2}^{\Delta\eta_j=\delta/2}$$

The only variable is the magnetization magnitude μ, which is obtained by solving the following iterative procedure:

$$\frac{1}{2\pi}\sum_j\sum_i \mu(\alpha_i, \beta_j) * I(\alpha_i, \beta_j) = \psi(\alpha, \beta)$$

Or in an array form:

$$I\vec{\mu} = \vec{\psi}$$

Where I have $(n * m) \times (n * m)$ dimensions and is the geometric factor of the algorithm. $\vec{\mu}$ is the unknown variable of $(n * m) \times 1$ the vector of magnitude magnetization of every dipole. $\vec{\psi}$ $(n * m) \times 1$ the vector data set.

The iterations are performed using the Gauss-Seidel method for $\vec{\mu}$ for lineal problems, so for the k iterations we have:

$$L_*\vec{\mu}^{k+1} = \vec{\psi} - U\vec{\mu}^k$$

Where L_* and U are the strict triangular matrix and upper triangular matrix of I respectively. The iteration stops until a certain convergence for $\vec{\mu}$ is achieved.

Once $\mu(\xi,\eta)$ is found, we can calculate the magnetic field for an arbitrary surface above D, being the continued surface C. In our case, we will choose the topography surface with a clearance altitude h_0. In which h_0 is the common distance above the topography, minimizing the topographic distortion due to high topographic reliefs in the area.

B.2 Algorithm validation

The algorithm was implemented in MATLAB routines, requiring three input grids: (1) observed data, (2) altitude of the data and (3) topography.

Before using the algorithm on real data, it will be validated through synthetic examples with known topography and magnetic field everywhere. The synthetic data was generated using the MAG3D code of the University of British Columbia (UBC). The topography was chosen simulating a symmetric depression, which have a maximum altitude difference of 250 meters (Figure B-2).

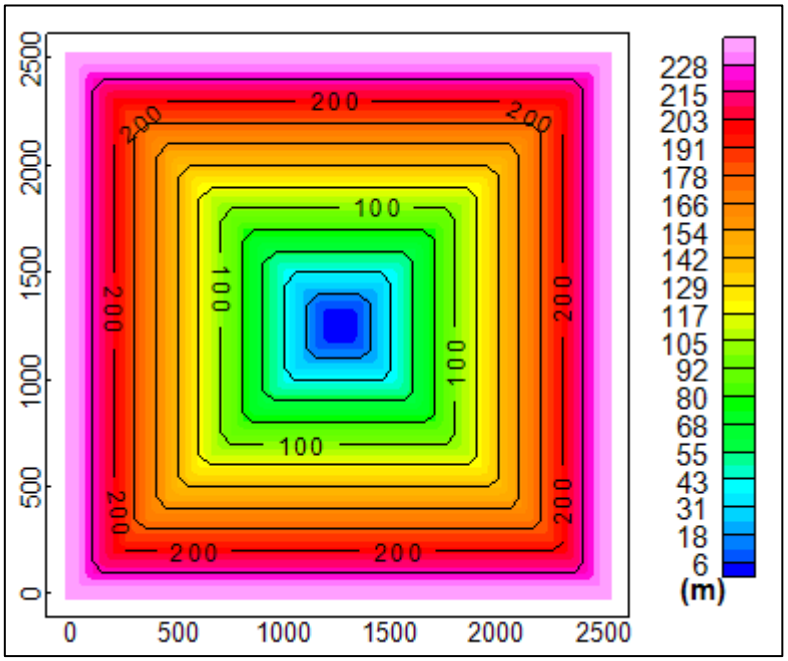

Figure B-2: Topography used for the synthetic data set as an input for MAG3D code. Contours every 20 meters.

To simplify the examples, we considered a magnetized cube (400m x 400m x 400m) buried 100m from the surface level. The magnetic susceptibility was constant (0.1 SI) and the surrounding is no magnetized. IGRF parameters used were TMI = 20.000 nT, I = -45° and D = 0°. We will consider a flat topography and after we will include high topography reliefs shown before (Figure B-2).

B.2.1 Flat topography case

Using the geometry and parameters noted before, synthetic data is generated with the MAG3D code at a barometric altitude of 200m from a flat surface at 0m. The first step is to check if the model correctly reproduced the anomaly at this altitude

and using the same dipole layer magnetization computed, calculate the anomaly for different altitudes which are also compared with synthetic data.

The first step is achieved with absolute errors in the order of 10^{-3} nT, defined as $(\psi(\alpha,\beta) - \phi(\alpha,\beta))$. Both anomaly maps are shown in Figure B-3 and the error histogram is shown in Figure B-4.

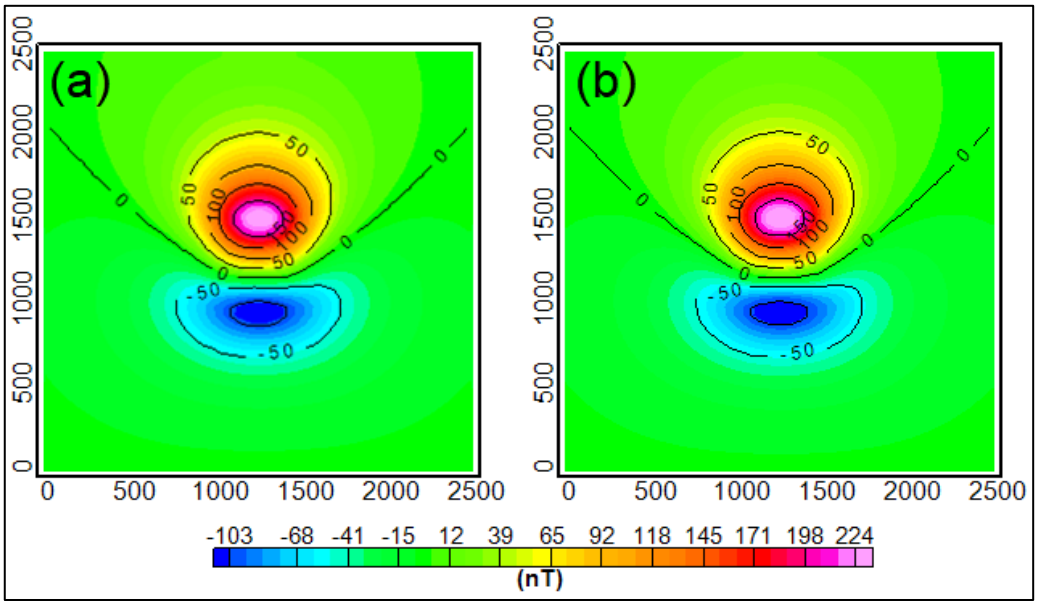

Figure B-3: (a) Synthetic data from MAG3D, (b) Computed data from the dipole layer magnetization. Both data set were calculated at 200m above the topography (unit in meters). Contour levels every 50 nT.

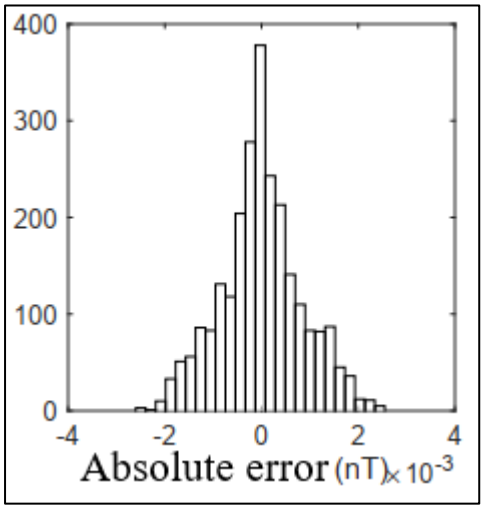

Figure B-4: Absolute error histogram for the flat topography case at 200m above the surface.

From the computed dipole layer magnetization, we perform 4 continuations at different altitudes: 100m, 150m, 250m and 300m. We will compare the data sets obtained along a profile cutting the anomaly's maximum. Continuations at 150m and 250m are resumed in Figure B-5, meanwhile continuations at 100m and 300m in Figure B-6, both figures also include the absolute error histogram comparing the calculation data from the dipole layer magnetization and the synthetic data from MAG3D.

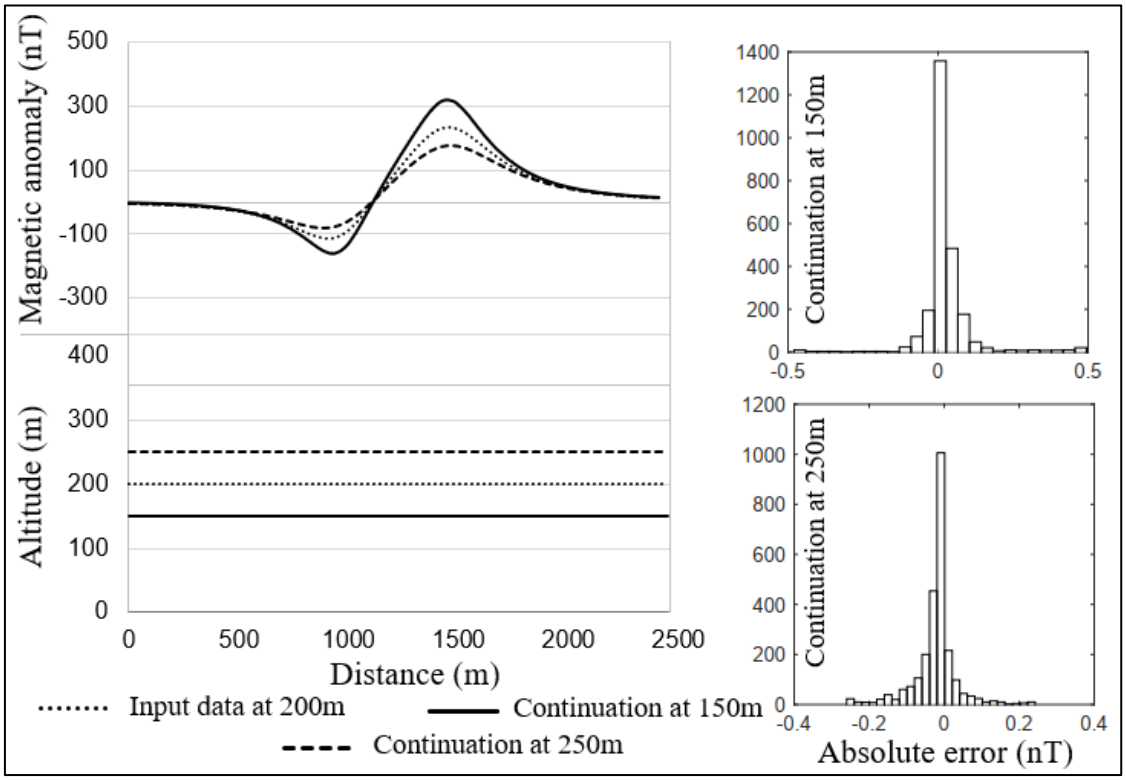

Figure B-5: Comparison between continuations at 150m, 250m and the input data at 200m. Detailed errors are shown in the histograms.

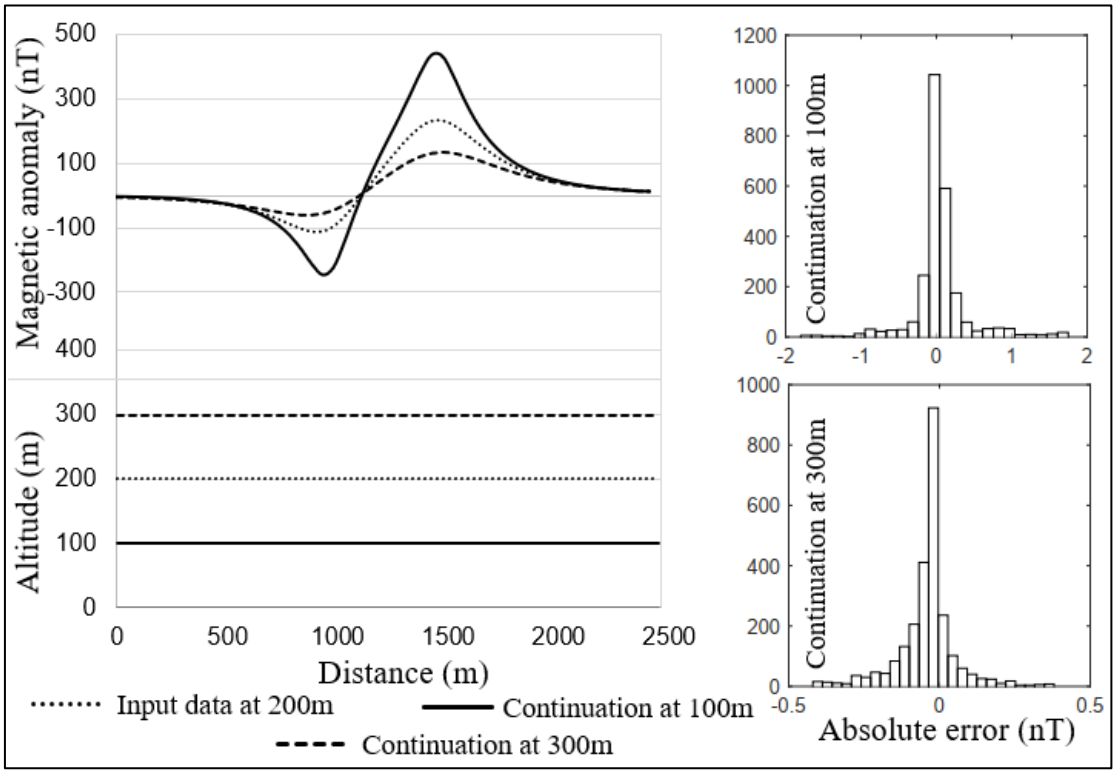

Figure B-6: Comparison between continuations at 100m, 300m and the input data at 200m. Detailed errors are shown in the histograms.

B.2.2 Variable topography case

Using the synthetic topography (Figure B-2) and the same geometric and parameters noted at the beginning. The input data is calculated with MAG3D code at a barometric altitude of 340m above the surface. With the potential data, barometric altitude and the topography, the dipole layer magnetization is computed. With the dipole layer we procced to compare computed data with the synthetic data (Figure B-7). Absolute errors are shown in Figure B-8.

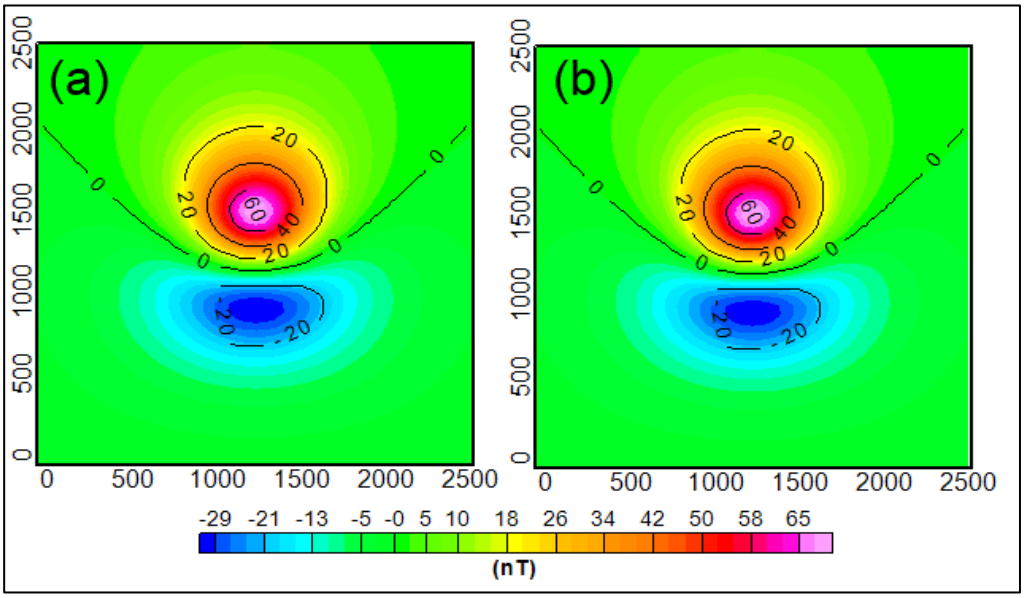

Figure B-7: (a) Synthetic data from MAG3D, (b) Computed data from the dipole layer magnetization. Both data set were calculated at a barometric altitude of 340m (unit in meters). Contour levels every 50 nT.

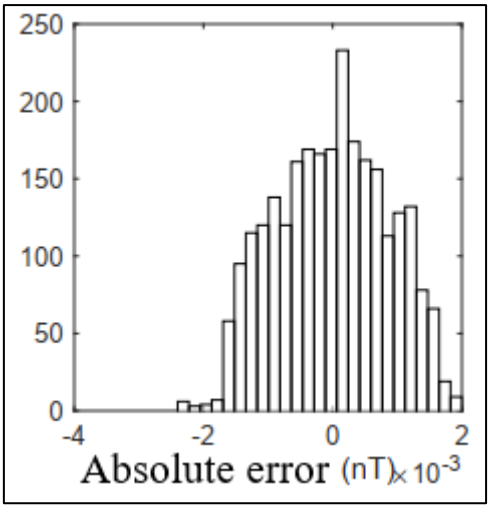

Figure B-8: Absolute error histogram for the variable topography case at 340m barometric altitude.

After this first step, we test several altitudes: 2 barometric and 4 with a clearance altitude above the topography. The first 2 barometric continuations (upward and

downward continuations) are shown in Figure B-9 for barometric altitudes of 240m and 440m.

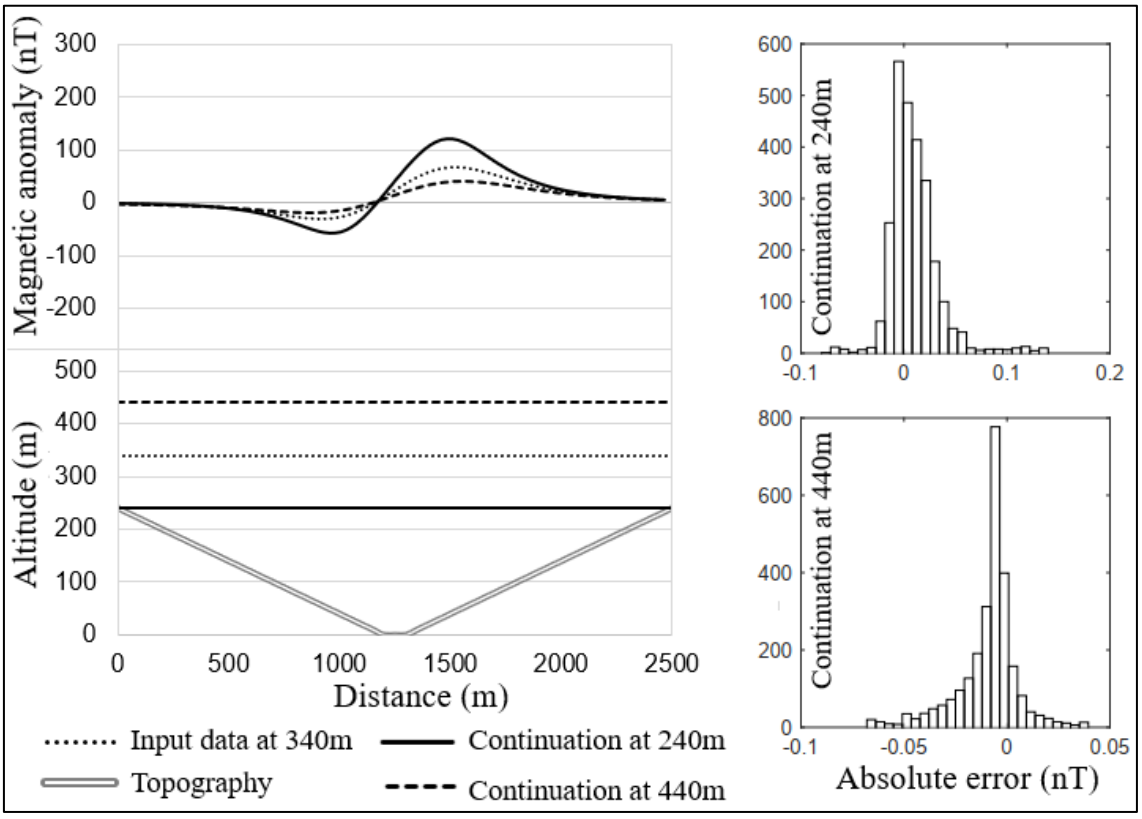

Figure B-9: Comparison between continued and synthetic data for barometric altitudes of 240m and 440m with their absolute error histograms.

Now we test the most important cases, which are continued to an arbitrary surface with clearance altitudes of 200m, 100m, 50m and 25m. The first two are shown in Figure B-10 with an anomaly map for the case of a clearance altitude of 100m (Figure B-11). The last two are shown in Figure B-12. All the continuations were performed with the same dipole layer magnetization computed in the first step.

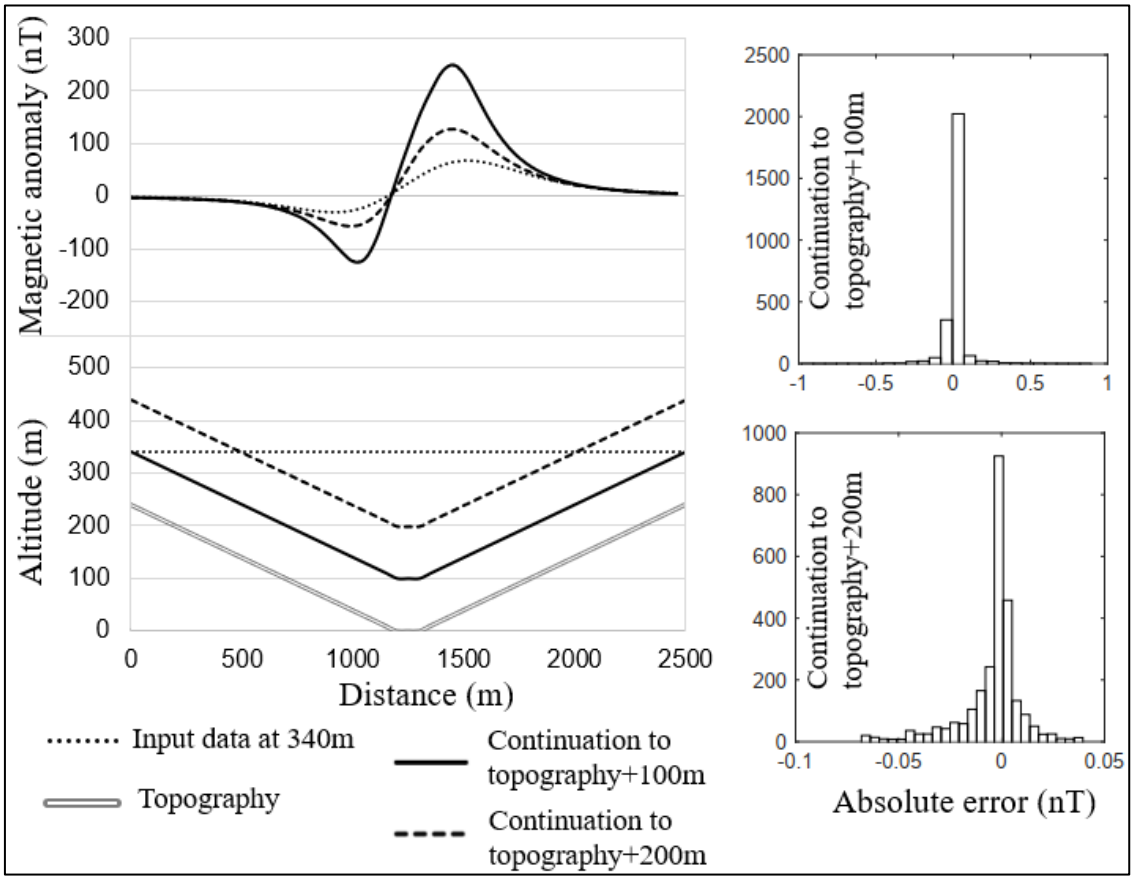

Figure B-10: Comparison between continued and synthetic data for clearance altitudes of 200m and 100m with their absolute error histograms.

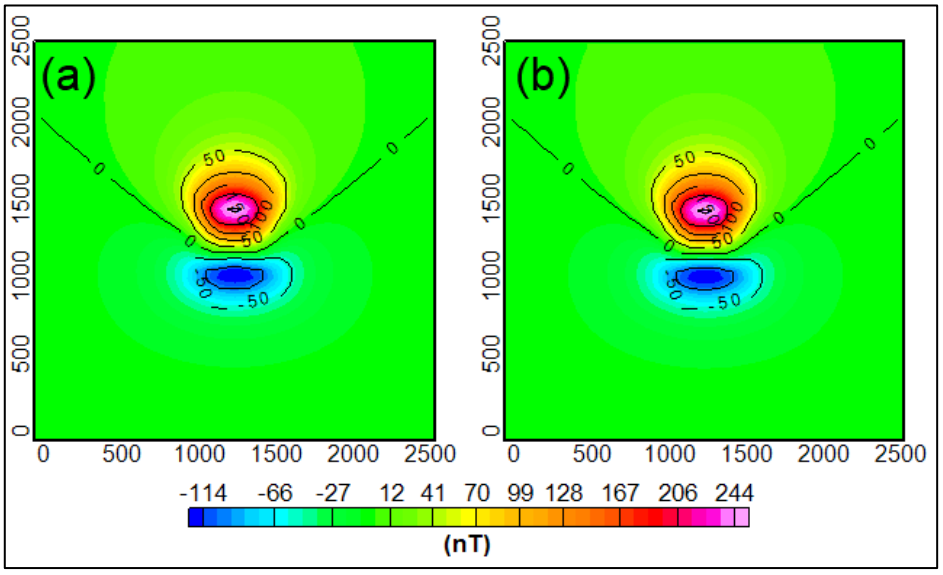

Figure B-11: (a) Synthetic data from MAG3D, (b) Computed data from the dipole layer magnetization. Both data set were calculated at clearance altitude of 100m (unit in meters). Contour levels every 25 nT.

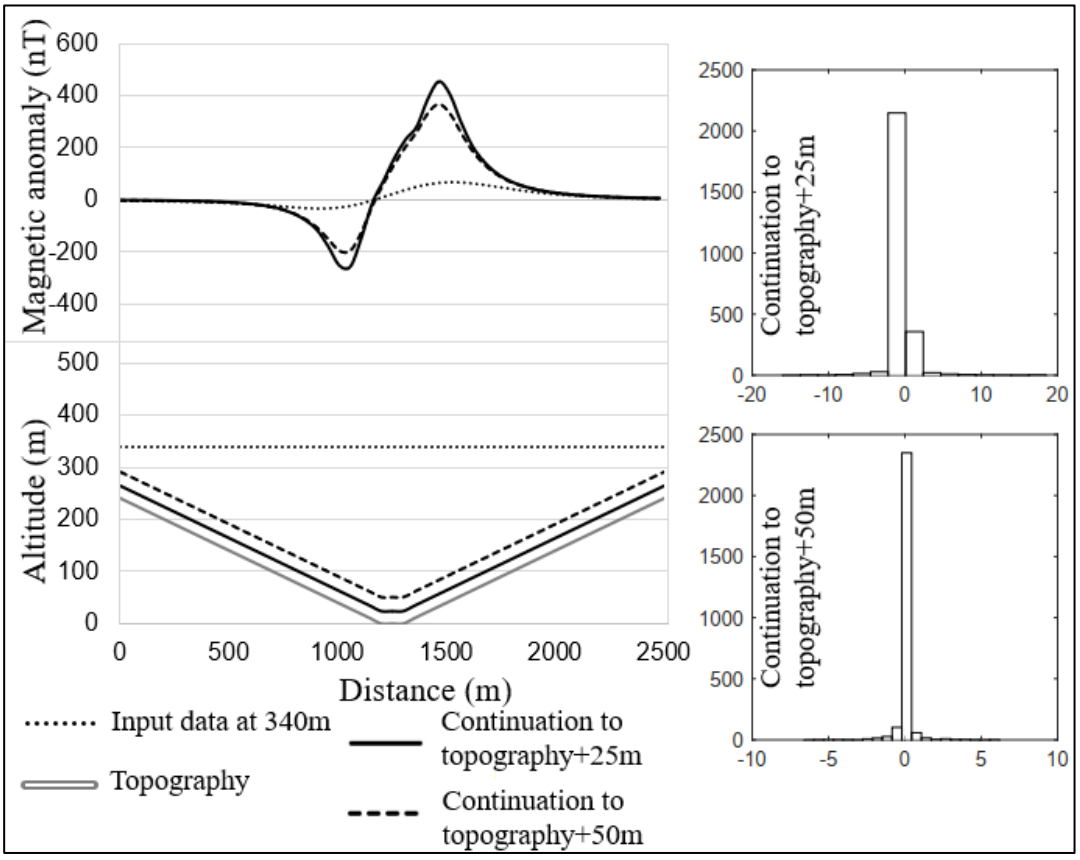

Figure B-12: Comparison between continued and synthetic data for clearance altitudes of 50m and 25m with their absolute error histograms.

All these tests show how robust the algorithm is for high topographic reliefs (> 300m). The maximum errors are ~ 10% with a mean error of ~ 1% for the most demanding continuation (clearance altitude of 25m). All the rest of the continuations showed errors below 1%.

Remarkably, this algorithm also reproduces the wavelength of the anomaly and the magnitude. Downward continuations are stable and shortens the wavelength. In contrast, upward continuation widens the wavelengths while decreasing the

amplitude. Finally, we correctly validated the continuation algorithm of Hansen and Miyazaki (1984) and will be applied for the data set obtained in this thesis.

B.3 Continuation of La Cabaña magnetic survey

Using the corrected measured magnetic data in La Cabaña (Figure B-13), the algorithm is applied to calculate the magnetized dipole layer of the main anomaly found (black square in Figure B-13).

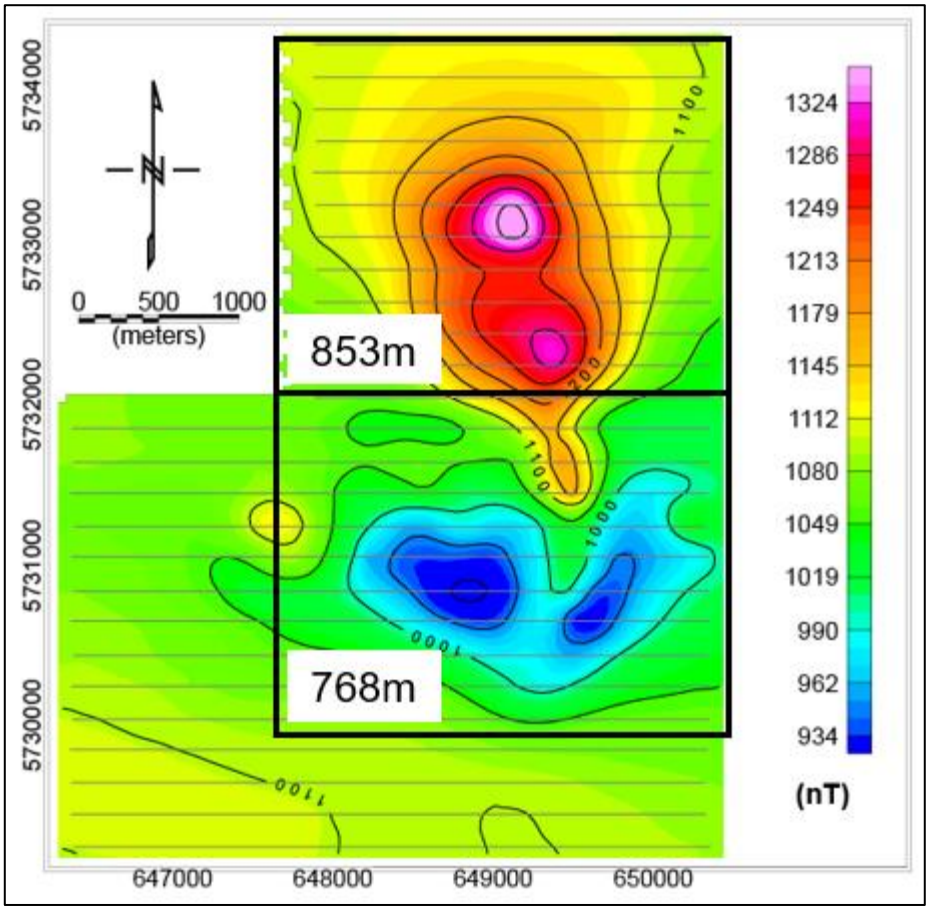

Figure B-13: Total magnetic intensity map from La Cabaña ultramafic bodies acquired via UAV airborne magnetic survey. Gray lines show the flights of the UAV system. Contour

levels every 50 nT. In black square is the data set used for the continuation and the associated altitude of the UAV system.

It is important to note that the flights of the UAV system were set to flat barometric altitudes, producing distortion of the data by the topography. In specific, two barometric altitudes were flown of 853m and 768m (see Figure B-13 for both sub-data sets with different altitudes).

After the calculation of the magnetized dipole layer using both sub-data sets, the continuation is set to an arbitrary surface parallel to the topography plus 200m, the new anomaly map is shown in Figure B-14.

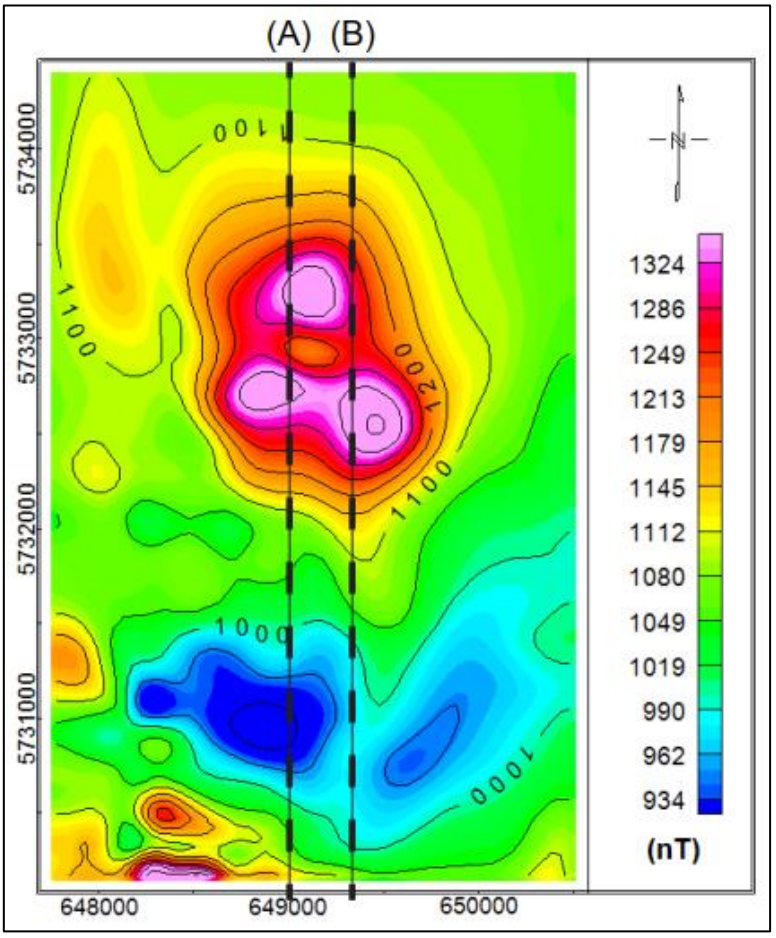

Figure B.14: Corrected total magnetic intensity map after the continuation to an arbitrary surface parallel to the topography plus 200m. Contours every 50 nT. (A), (B) are two test profiles to show how the anomaly changed after the continuation.

In addition, topography channel, flight altitude and continuation altitude along with the anomaly profile before and after the continuation are displayed in Figure B-15 and B-16 for the profiles (A) and (B). This corrected data is used for the inversions which are explained in Appendix D.1.

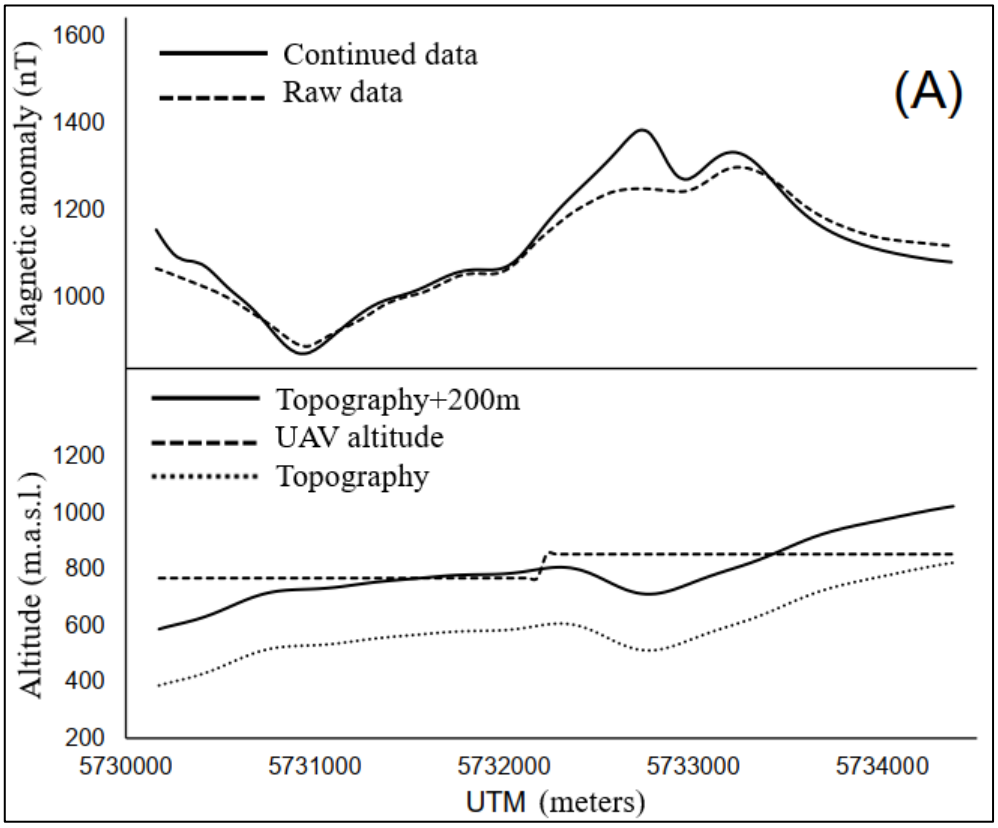

Figure B-15: Comparison along profile (A) of the continued data against the measured in La Cabaña area through UAV. Topography channel and altitude channels are also shown.

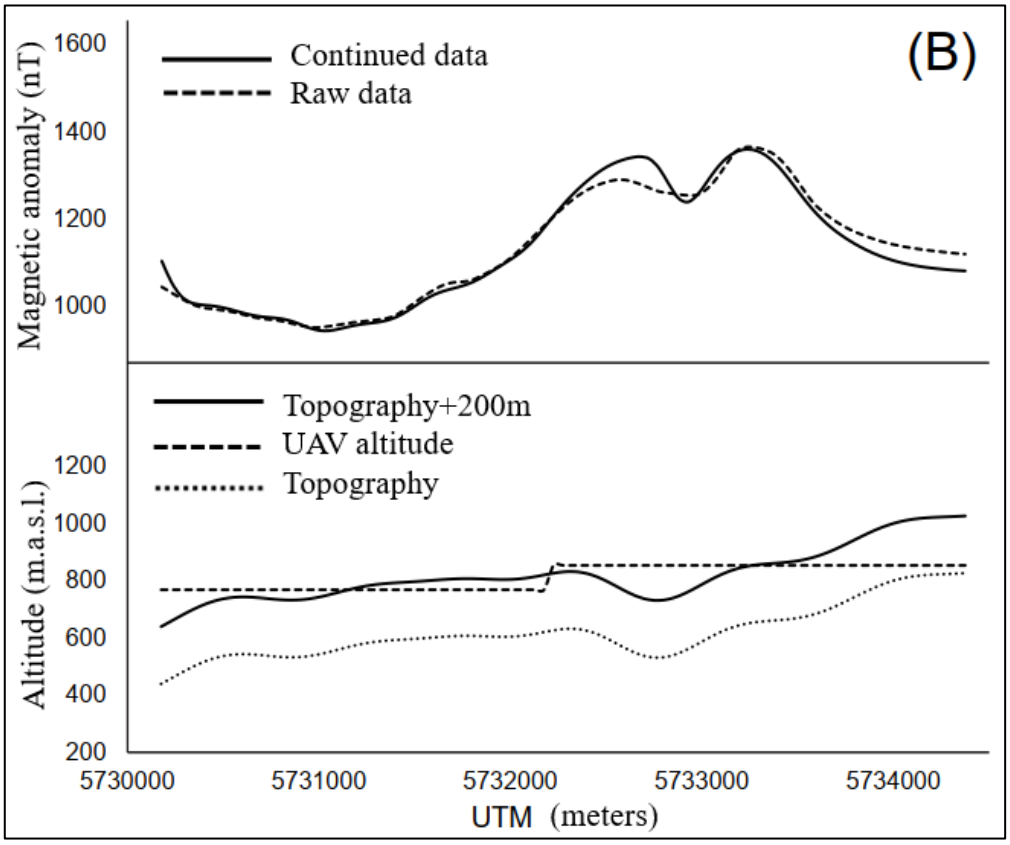

Figure B-16: Comparison along profile (B) of the continued data against the measured in La Cabaña area through UAV. Topography channel and altitude channels are also shown.

APPENDIX C: ELECTRIC RESISTIVITY TOMOGRAPHY THEORY AND INVERSION

This geophysical method employs an artificial source of current, which is introduced into the ground through point electrodes and also measuring the potential in other electrodes in an array setup. The theory presented here is extracted from Telford and Sheriff (1990) where further explanations are available.

C.1 Potentials in homogeneous media

Considering a continuous current flow in a homogeneous medium where displacement of currents is neglected. The current density $\boldsymbol{J}$ and the electric field $\boldsymbol{E}$ are related through the Ohm's law:

$$\boldsymbol{J} = \sigma \boldsymbol{E}$$

Where σ is the conductivity of the medium and represent the geological domains to be mapped. In geophysical applications the term resistivity is commonly used, which is $\rho = 1/\sigma$.

The electric field is the gradient of a scalar potential because $\boldsymbol{E}$ is a conservative vector field.

$$\boldsymbol{E} = -\nabla V$$

Thus,

$$\boldsymbol{J} = -\sigma \nabla V$$

Moreover, regions with finite conductivity (appropriate assumption in geophysical applications), charge does not accumulate to any extent during current flow. Mathematically this is represented as:

$$\nabla \cdot \boldsymbol{J} = 0$$

Using the last two equations we have:

$$\nabla \cdot \left(\frac{1}{\rho}\nabla V\right) = \nabla\left(\frac{1}{\rho}\right) \cdot \nabla V + \frac{1}{\rho}\nabla^2 V = 0$$

If we work in a homogeneous media ($\rho = \text{constant}$), we have the Laplace's equation for the scalar potential:

$$\nabla^2 V = 0$$

However, the earth cannot be represented as a one region with constant resistivity. In order to assess this, we divide the earth into several regions with homogeneous media to discretize the earth heterogeneities. In this scenario, we must set boundary conditions between the layers to ensure continuity in electric fields and potentials.

$$E_{x\,i} = E_{x\,+1}$$

$$\frac{E_{z\,i}}{\rho_i} = \frac{E_{z\,i+1}}{\rho_{i+1}}$$

$$V_i = V_{i+1}$$

C.2 Four electrode setups at surface

When the distance between two current electrodes is finite, the potential at any nearby point will be affected by both current input electrodes. Figure C-1 show a schematic position of the current and measuring electrodes.

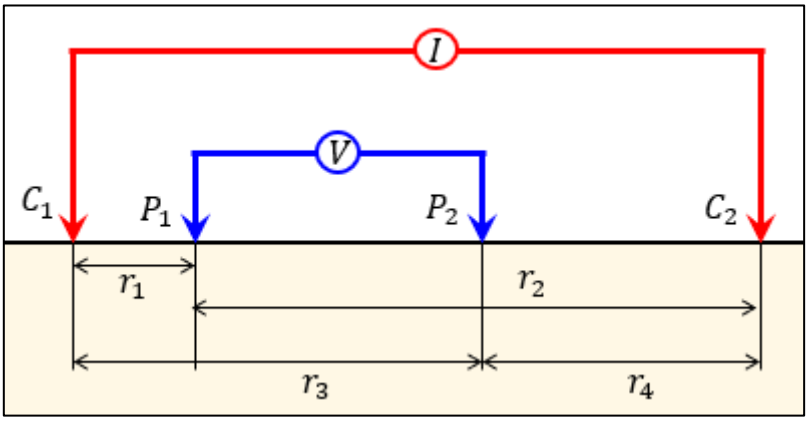

Figure C-1.: Schematic positions of the current electrodes (denoted as C) and measuring electrodes (denoted as P), modified from Telford and Sheriff (1990).

In this case, the potential due to C_1 at P_1 is

$$V_1 = -\frac{A_2}{r_1}\,; A_1 = -\frac{I\rho}{2\pi}$$

In contrast, the potential at P_1 due to C_2 is $V_2 = -\frac{A_2}{r_2}\,; A_2 = \frac{I\rho}{2\pi} = -A_1$

Adding both potentials give us:

$$V_1 + V_2 = \frac{I\rho}{2\pi}\left(\frac{1}{r_1} - \frac{1}{r_2}\right)$$

By introducing the potential at P_2 we finally calculate the difference between the potential V_1 and V_2 which are measured in field campaigns along with the current I and the distances r.

$$\Delta V = \frac{I\rho}{2\pi}\left\{\left(\frac{1}{r_1} - \frac{1}{r_2}\right) - \left(\frac{1}{r_3} - \frac{1}{r_4}\right)\right\} = \frac{I\rho}{2\pi}G$$

Where G is a geometry parameter depending on the positions of $C_{1,2}$ and $P_{1,2}$.This arrangement corresponds to the four electrodes setup commonly used in

geophysical fieldwork. Several setups can be made by changing the position of C, P, the one used in this thesis will be explained in the following subchapter.

A synthetic example of the current flow for a homogeneous media is shown in Figure C-2 with an array similar to the Figure C-1.

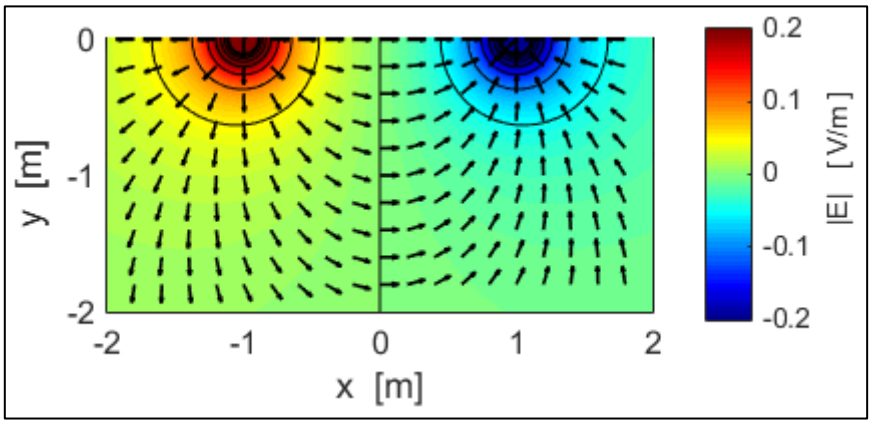

Figure C-2: Electric field section due to two input currents at $x = -1$ and $x = 1$ in a homogeneous media of $\rho = 100\ \Omega m$. Contours every 0.05 V/m.

C.3 Apparent resistivity and electrode configuration

In order to understand the geology beneath the surface level, during fieldwork we can measure ΔV and I. Also, we can setup the electrode geometry $r_{1,2,3,4}$, thus the only unknown parameter is the resistivity ρ. This parameter can be obtained by the following expression:

$$\rho = \frac{2\pi\ \Delta V}{I\ G}$$

If the ground is homogeneous (like in Figure C-2), this resistivity will be constant for any current and electrode arrangement and is equal to the measured and calculated by the expression above.

However, if the ground is inhomogeneous and the electrode configuration is switched G will change in every point. This results in a different value of ρ for each measurement which is linked to a specific value of G. This measured quantity is known as the apparent resistivity ρ_a. In general, the real resistivity of a geological domain ρ is slightly different from the ρ_a measured. To recover the real resistivity ρ it is necessary to invert the data set measured ρ_a.

The electrode configuration used in this thesis is called the dipole-dipole array (Figure C-3). This array places the two current electrodes closely spaced as well as the measuring ones. In this case the apparent resistivity is

$$\rho = \frac{2\pi\, n^3 l\, \Delta V}{I}$$

Where n is the total number of electrodes used in the array and is the spacing between electrodes.

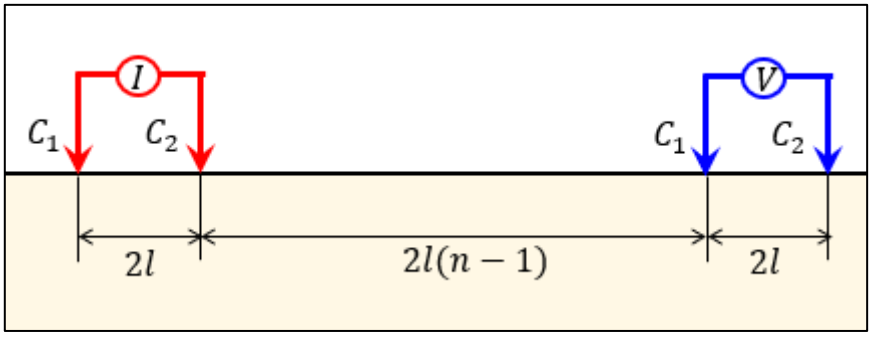

Figure C-3.: Schematic positions of the current electrodes (denoted as C) and measuring electrodes (denoted as P) for the dipole-dipole array. n is the number of electrodes in the array. Modified from Telford and Sheriff (1990).

C.4 Inversion procedure and further results

In order to understand the contact between the different domains, the ERT method provides enough resolution to acknowledge this geometry. Moreover, potential-field methods are not the most suitable methodology for this task, so the ERT allow us to provide a more detailed mapping to correctly account these possible structures.

The input data for the inversion are: (1) resistance data for every quadripole, (2) position and topography for every electrode used. The first one was acquired during fieldwork with the instrument ABEM Terrameter LS2 with 48 electrode array and up to 20m dipole spacing, where the profiles done are shown in Figure A.6. Profiles X and Y were done with a 20m spacing while profile Z was done with a 12m dipole spacing due to geometric restrictions in the area. During the measurement, we used 4 stacking for each quadripole in all the profiles and a threshold of 10% standard deviation for the profile X and 100% for the Y and Z to reduce very noisy data. We used a dipole-dipole configuration, since this array has the best resolution for vertical structures and a good horizontal and depth coverage than other arrays (Sharma and Verma, 2015).

The 2D inversion of the processed data were performed with the software ZondRes2D. The inverse problem for ERT data is a nonlinear inverse problem. Thus, we tested several initial solutions to confirm that we were not in a local minimum of the solution. This was done by setting 4 constants initial resistivities: 10 ($\Omega - m$), 200 ($\Omega - m$), 1000 ($\Omega - m$) and 10000 ($\Omega - m$), confirming that for the three profiles, the solution was the same. Also, since there are not in-situ

resistivity measurements, we set the search resistivities between 10 and 10000 ($\Omega - m$) which will be checked later with other studies in the paper and not in this section. For comparison purposes, we will show the input data (pseudosection) along with the calculated pseudosection associated with inverted data set with the lowest misfit achieved. After this first comparison, a second one will be shown to compare different inversion methods (Focused and Occam), to confirm if the geometry is generated by geological sources rather than artifacts generated by the inversion.

The input pseudosections, with their respective calculated pseudosection from the inversions are displayed in Figures C-4, C-5 and C-6 for the profiles X, Y and Z respectively.

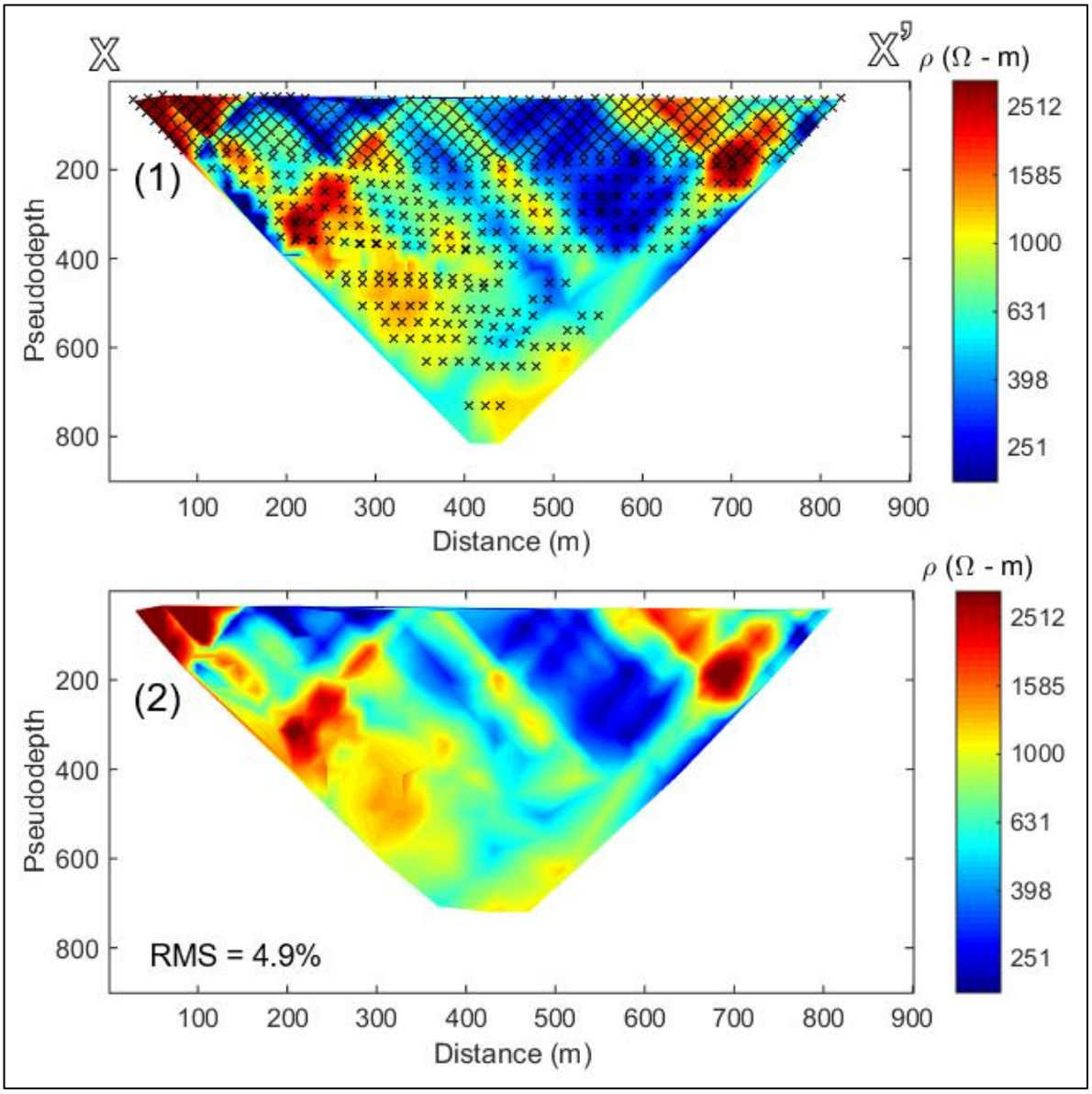

Figure C-4: Resistivity pseudosections of profile X-X' (1) Field apparent resistivity data, crosses represent every data point measured, (2) calculated apparent resistivity data from the inversion with the associated misfit (RMS).

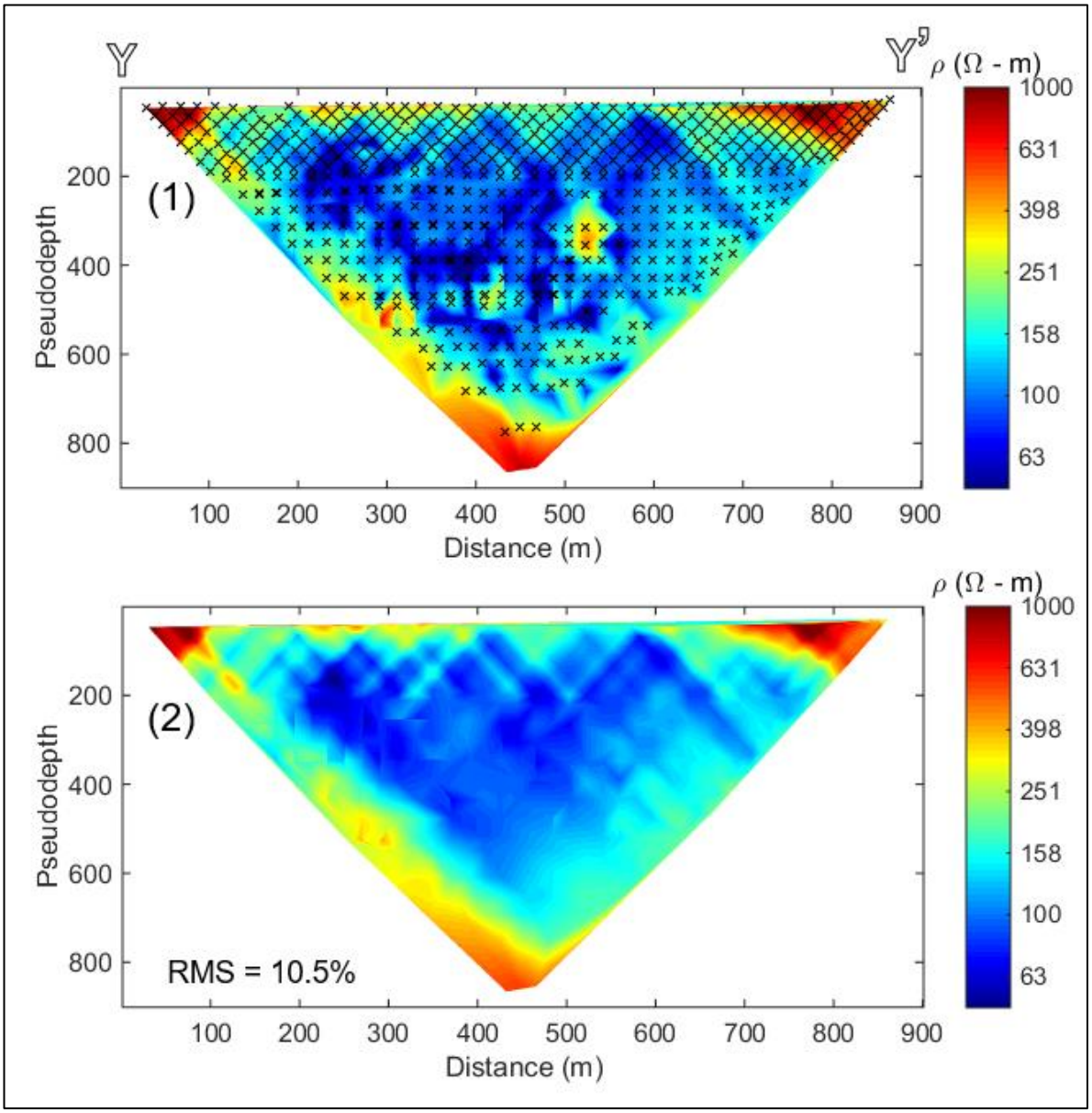

Figure C-5: Resistivity pseudosections of profile Y-Y' (1) Field apparent resistivity data, crosses represent every data point measured, (2) calculated apparent resistivity data from the inversion with the associated misfit (RMS).

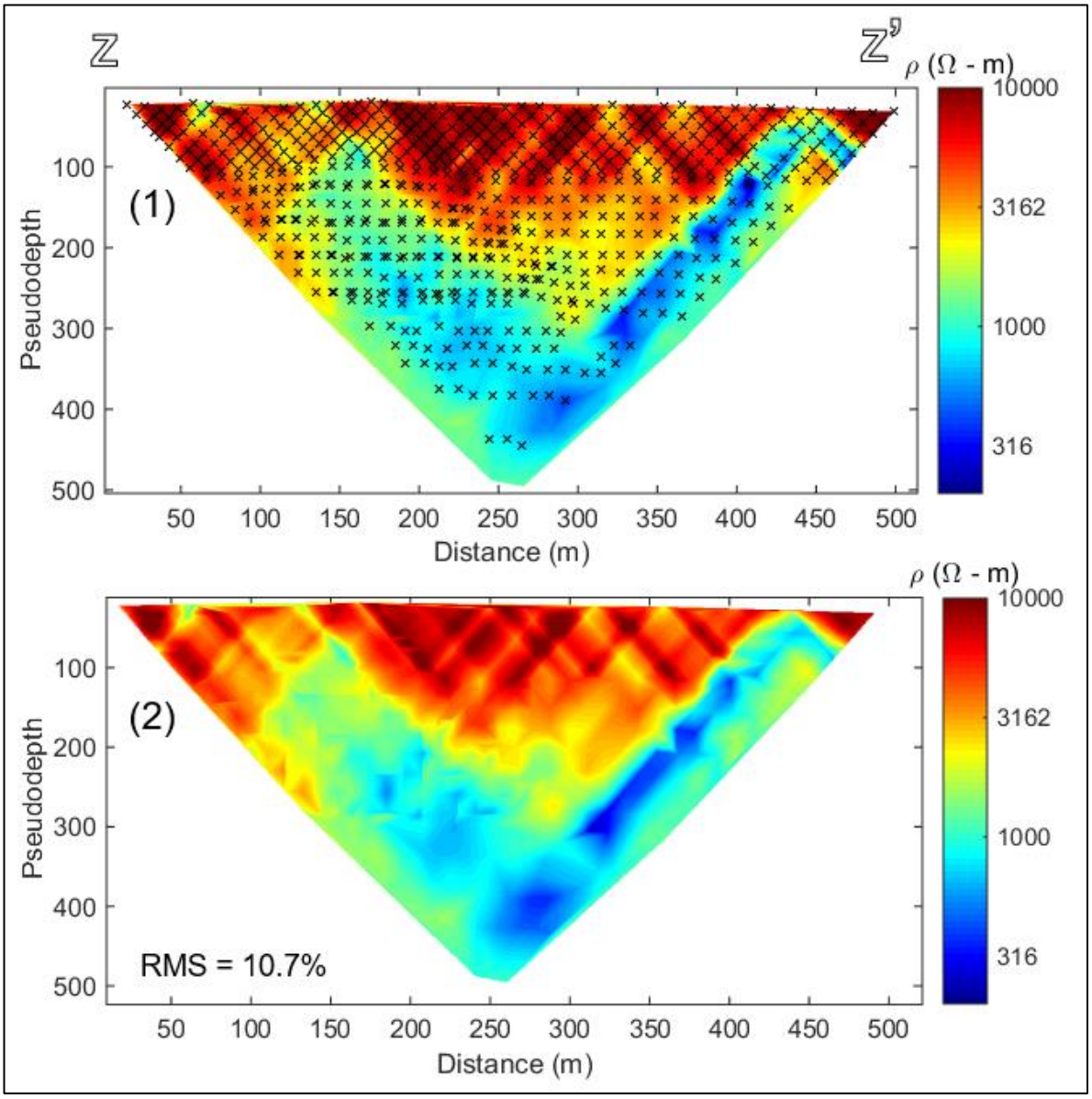

Figure C-6: Resistivity pseudosections of profile Z-Z' (1) Field apparent resistivity data, crosses represent every data point measured, (2) calculated apparent resistivity data from the inversion with the associated misfit (RMS).

Now we proceed to compare different inversion methods, which are shown in Figures C-7, C-8 and C-9.

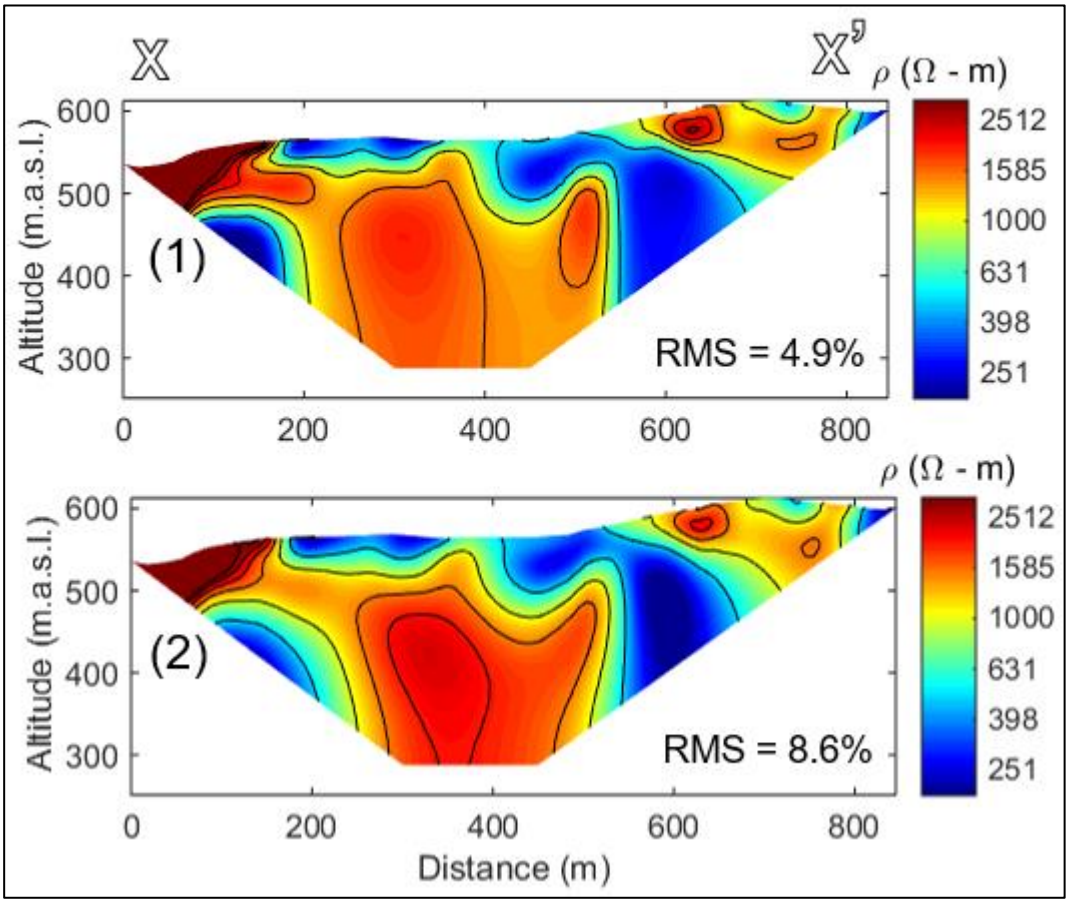

Figure C-7: Inverted resistivity data of profile X-X' with different inversion methods. (1) Focused and (2) Occam. Both inversions have the same color bar, scale 1:1 and contours every 500 $\Omega - m$.

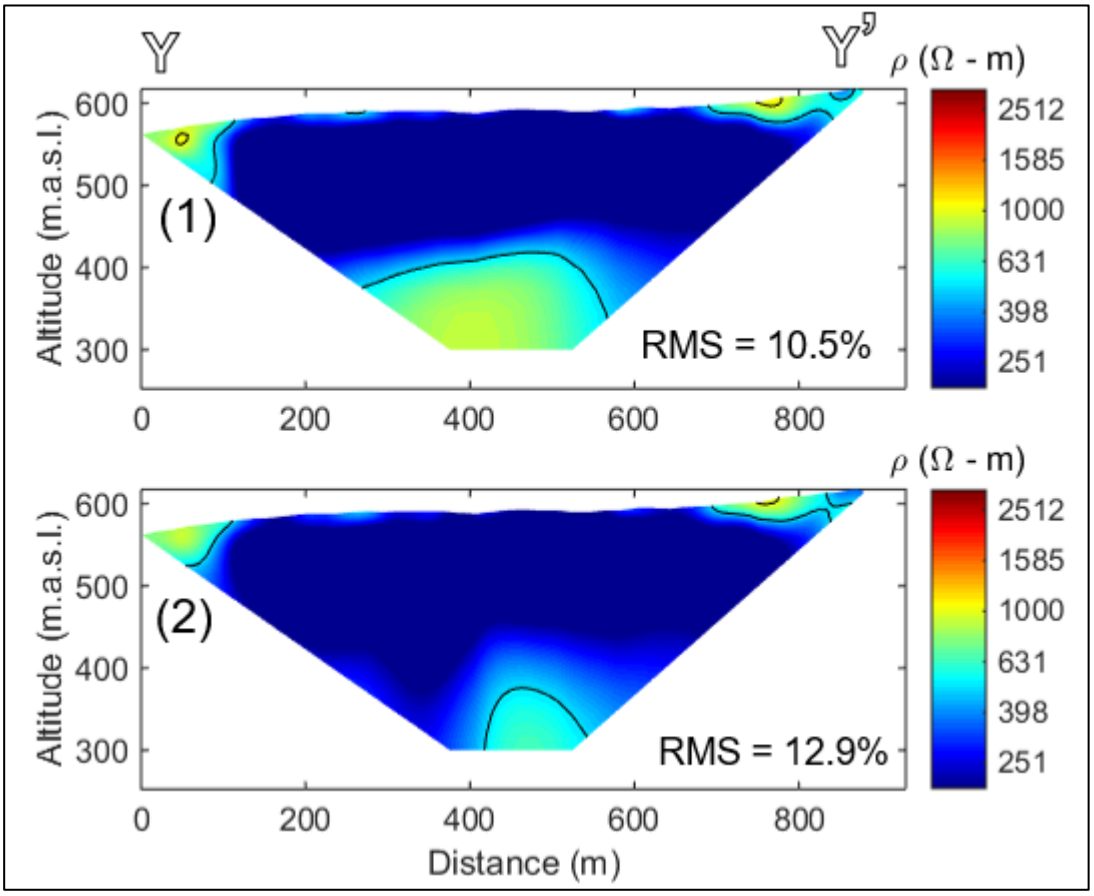

Figure C-8: Inverted resistivity data of profile Y-Y' with different inversion methods. (1) Focused and (2) Occam. Both inversions have the same color bar, scale 1:1 and contours every 500 $\Omega - m$.

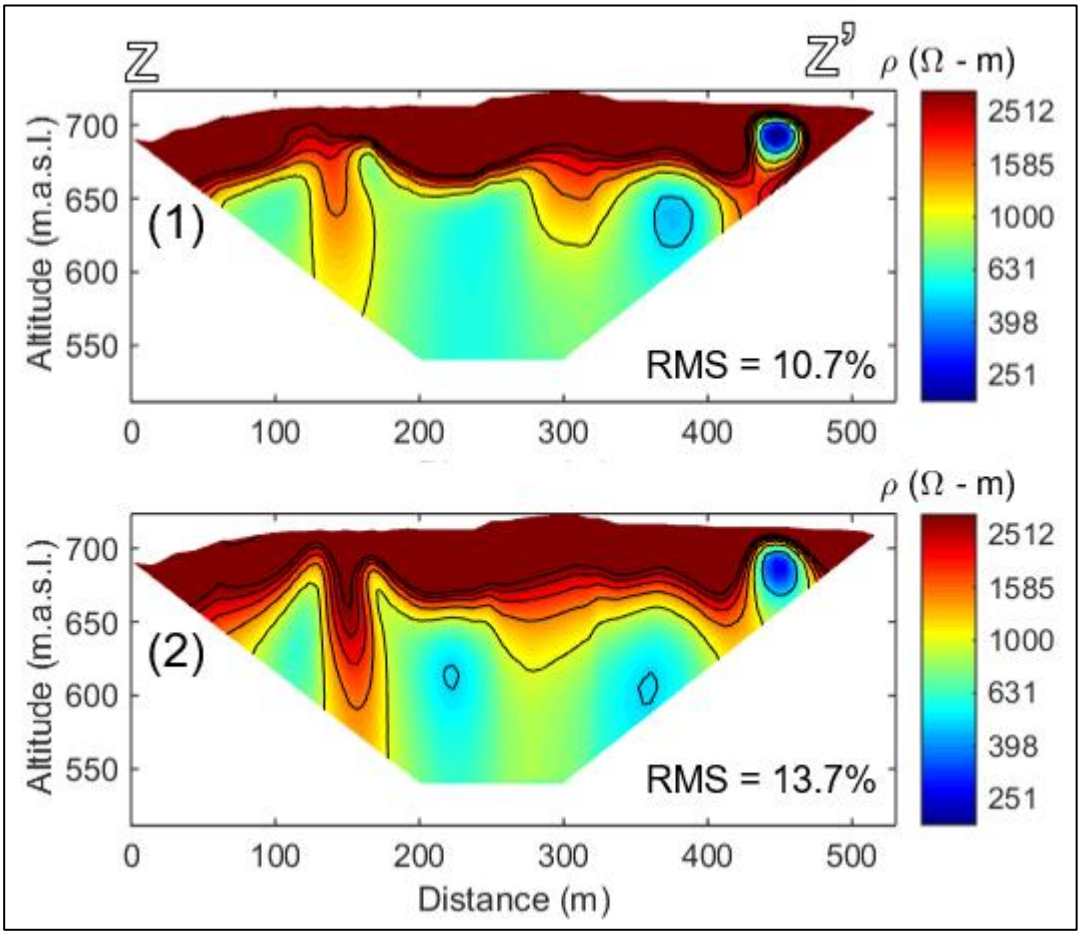

Figure C-9: Inverted resistivity data of profile Z-Z' with different inversion methods. (1) Focused and (2) Occam. Both inversions have the same color bar, scale 1:1 and contours every 500 $\Omega - m$.

Overall, both inversion methods show the same geometries. Since all the inverted ERT data was plotted with the same color scale, providing in this way a direct comparison between them. The most interesting ERT result was the X-X' section (Figure C-7) which cut different geological domains, observed in an abrupt resistivity change from ~200 ($\Omega - m$) to > 1000 ($\Omega - m$). The contact between these two domains is without doubt vertical, which is in good agreement between both

methods. The contact between these two domains is without doubt vertical, which is in good agreement between both methods and remarkably with the magnetic inversion in the same location (see Appendix A.3). This comparison between different geophysical methods allow to confirm that this vertical contact is generated by geological sources and is not an artifact from the magnetic nor ERT inversions parameters or methods.

On the other hand, sections Y-Y' and Z-Z' (Figures C-8 and C-9), seems to be only in one but different geological unit, which are horizontally homogeneous in the resistivity domain. Even when these sections are slightly homogeneous, this is also supported with the magnetic inversions (see Appendix A.3). As mentioned before, these sections mapped different units. According to the magnetic inversion, ERT section Y-Y' (Figure C-8) mapped the southern-most part of the highly magnetized body in the magnetic section 3-3' (in Appendix A.3), which can be linked as a low resistivity domain < 500 ($\Omega - m$). In contrast, ERT section Z-Z' (in Appendix A.3) mapped the low to non-magnetized body seen in the eastern-most part in the magnetic section B-B' (in Appendix A.3), linked to high resistivities > 1000 ($\Omega - m$).

APPENDIX D: NUMERICAL MODELLING AND MORE RESULTS

D.1 Theory of the return flow numerical modelling

In order to understand the long-term deformation, we adopted a slow viscous approach using the Navier-Stokes and the continuity equation, in a general way for an incompressible fluid (ρ = constant):

$$\frac{\partial \boldsymbol{u}}{\partial t} + (\boldsymbol{u} \cdot \nabla)\boldsymbol{u} = -\frac{1}{\rho}\nabla P + \frac{\eta}{\rho}\nabla^2 \boldsymbol{u} + \boldsymbol{f}$$

$$\nabla \cdot (\rho \boldsymbol{u}) = 0$$

Where $\boldsymbol{u}$ is the velocity vector, P the pressure field, $\boldsymbol{f}$ a vector body force, t is the time, ρ is the density and η is the viscosity.

For numerical purposes, we used the dimensionless form of this equation by replacing the following scaling terms:

$$\boldsymbol{u} = \boldsymbol{u}^* \cdot U_o$$

$$P = P^* \cdot \frac{\eta_o U_o}{L_o}$$

$$t = t^* \cdot \frac{L_o}{U_o}$$

$$\nabla = \frac{\nabla^*}{L_o}$$

And a body force using the vector of acceleration within the gravity field:

$$\boldsymbol{f} = g \cdot \hat{g}$$

Thus,

$$\frac{\partial \boldsymbol{u}^*}{\partial t^*} \cdot \frac{U_o}{L_o/U_o} + (\boldsymbol{u}^* \cdot \nabla^*)\boldsymbol{u}^* \cdot \frac{U_o^2}{L_o} = -\frac{1}{\rho}\nabla P^* \cdot \frac{\eta_o U_o}{L_o} + \frac{\eta}{\rho}\nabla^{*2}\boldsymbol{u}^* \cdot \frac{U_o}{L_o^2} + g \cdot \hat{g}$$

Using the dimensionless numbers: the Reynolds number $Re = \frac{\rho U_o L_o}{\eta}$ and Froude number $Fr = \frac{U_o}{\sqrt{g L_o}}$, the equation follows:

$$\frac{\partial \boldsymbol{u}^*}{\partial t^*} + (\boldsymbol{u}^* \cdot \nabla^*)\boldsymbol{u}^* = \frac{1}{Re}(-\nabla P^* + \nabla^{*2}\boldsymbol{u}^*) + \frac{1}{Fr^2}\hat{g}$$

For geological problems, characterized by extremely low Reynolds and Froude numbers, let's say $< 10^{-20}$ and $< 10^{-10}$ respectively, the Navier-Stokes equations reduce to the Stokes equations of motion:

$$\frac{1}{Re}\left(-\nabla P^* + \nabla^{*2}\boldsymbol{u}^*\right) + \frac{1}{Fr^2}\hat{g} = 0$$

$$\nabla \cdot \boldsymbol{u} = 0$$

Where the non-linear term $\frac{\partial \boldsymbol{u}^*}{\partial t^*} + (\boldsymbol{u}^* \cdot \nabla^*)\boldsymbol{u}^*$ can be neglected without losing the main physics of the problem. Making the Stokes equations a linear problem. Nevertheless, they deserve special attention and numerical treatment to correctly perform the calculation of the pressure field, which is done by using the Penalty Method (Cuvelier, 1986). This method introduces an artificial compressibility which is a perturbed form of the continuity equation, the existence and regularity of the solution is developed by Cattabriga (1961). This perturbation form uses a penalty multiplier $\varepsilon \to 0$ as follows:

$$\nabla \cdot \boldsymbol{u} = \varepsilon(\nabla \cdot (\nabla P))$$

Where the right side of the last equation is an iteration correction for the pressure (e.g. Gerya et al., 2000). The penalty multiplier ε must be sufficiently small to

ensure accurate calculations. In practice, this is an empirical coefficient estimated at $\sim 10^{-7}$ for our case.

D.2 Scaling parameters and boundary conditions

The scaling parameters (U_o, L_o, η_o) used in our simulations were consistent with the geological and tectonic setting of the problem. Consequently, the following numbers were adopted

$$U_o = 60 - 120\,\frac{mm}{yr} = 1.09 - 3.08 \cdot 10^{-9}\,\frac{m}{s}$$

$$L_o = 10{,}000\ m = 10\ km$$

$$\eta_o = 10^{19}\ Pa \cdot s$$

Where U_o was chosen using the plate convergence velocities for the actual Nazca plate (Angermann et al., 1999) and oceanic plates during the Paleozoic (Matthews et al., 2016). In this way, the Dirichlet boundary condition for the subducting slab was $U = 1$, making all the velocity field computed stay in the range of $0 < \boldsymbol{u}/U_o < 1$.

Following the next parameter, L_o, was chosen to 10 km to make our dimension numbers stay in the range of $0 < L/L_o < 6$, because the maximum dimension was given by the maximum depth in our models which was 60 km.

The last one, the effective viscosity η_o, was set to $10^{19}\ Pa \cdot s$ which is the mean effective viscosity value for the sediments in subduction channel and the background effective viscosity in the model. This value was estimated by creep flow laws (Ranalli, 1995) and rheology parameters by Shea and Kronenberg (1992),

further details are found in the chapter 2. Thus, the effective viscosities in our simulations were in the range of $0.1 < \eta/\eta_o < 100$, which are one order of magnitude weaker and two order stronger, which are the highest found in the lithosphere. Overall, similar numbers have been used in several numerical simulations (e.g. Yáñez and Cembrano, 2003; Gerya et al., 2002; Daniel et al., 2001).

These scaling parameters were also chosen so the results are not expensive to save in the computer. For instance, by using this approach, a precision of 10 decimals was vastly enough for velocities between $0 < \boldsymbol{u}/U_o < 1$. In contrast, we needed to save up to 100 decimals precision if we wanted to save velocities $< 10^{-9}\, m/s$, making it extremely expensive in practice.

D.3 Further model results

In chapter 2, model results were shown for $U = 120\ mm/yr$ with a weak rheology. However, in the article models with $60\ mm/yr$ were not directly compared against the ones with $U = 120\ mm/yr$. Figure D.1 show this comparison at the same time for both cases.

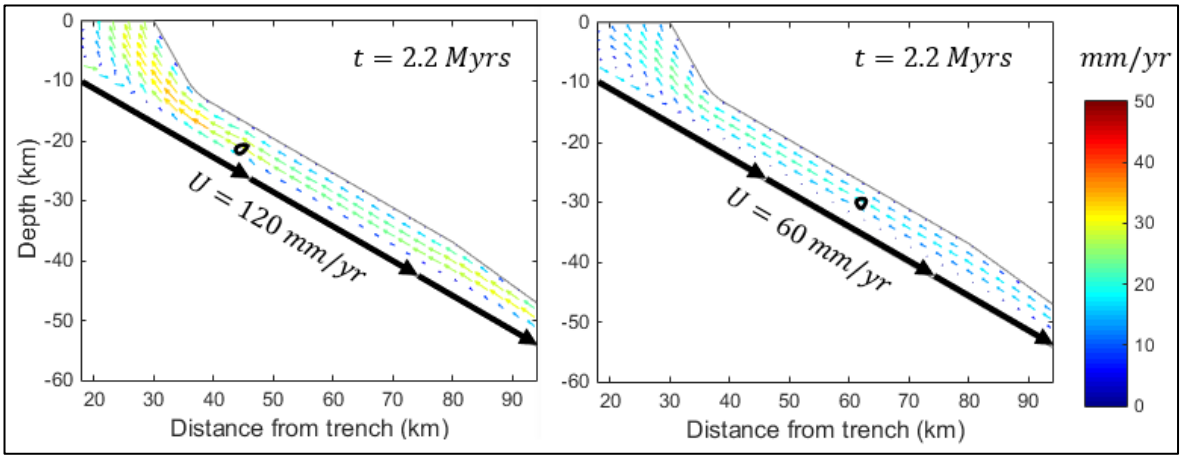

Figure D.1: Comparison between the velocity boundary condition for the same subduction channel width (8 km), down going slab dip (30°) and body diameter (1.5 km). Both panels have the same color bar and taken at $t = 2.2\ Myrs$.

Moreover, all the variations of the subduction channel geometry, down going slab dip and ultramafic body size for $U = 60\ mm/yr$ are shown in Figure D.2 for the same time.

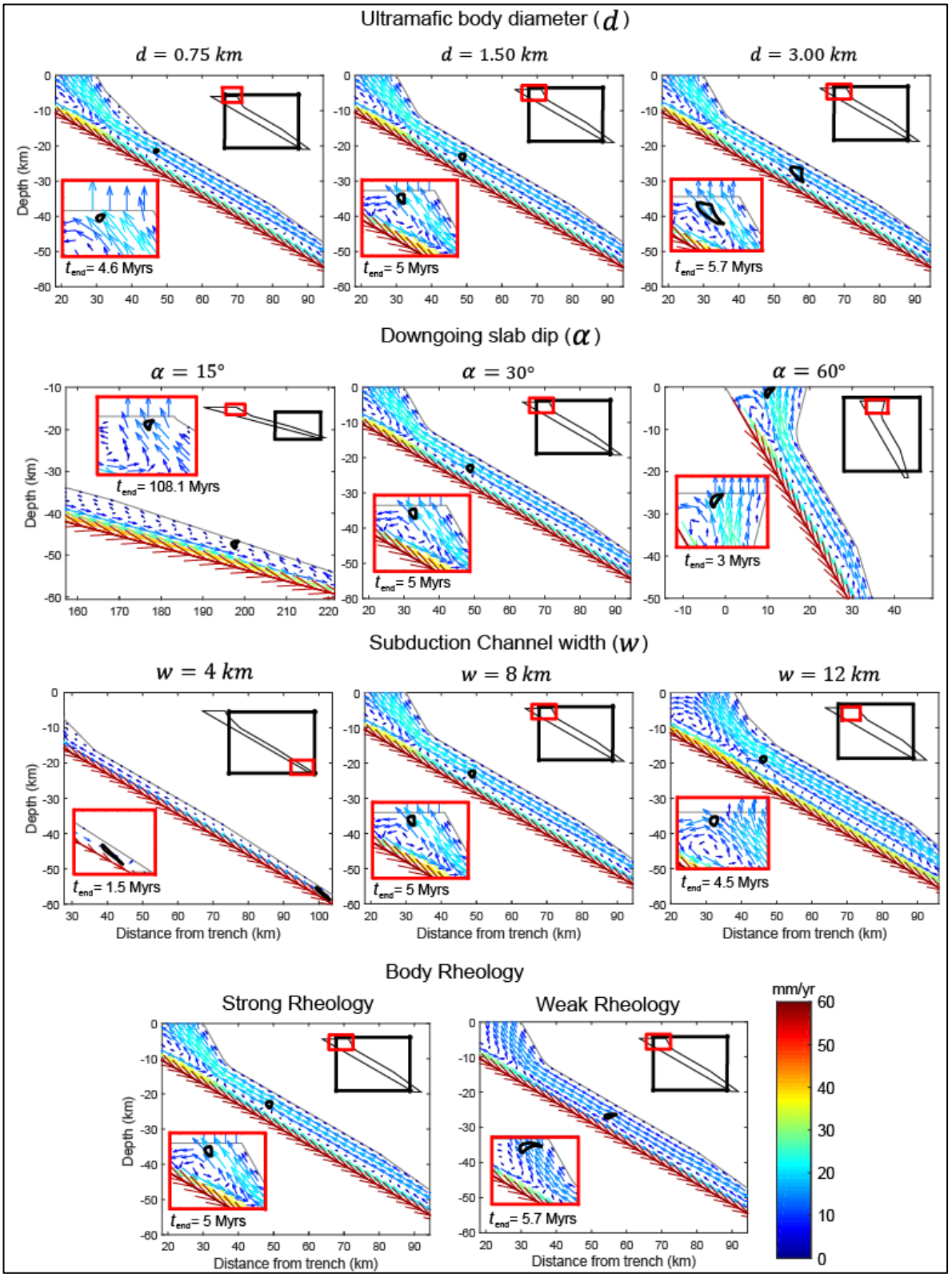
Ultramafic body diameter (d)
$d = 0.75\ km$
$d = 1.50\ km$
$d = 3.00\ km$
t_{end}= 4.6 Myrs
t_{end}= 5 Myrs
t_{end}= 5.7 Myrs
Downgoing slab dip (α)
$\alpha = 15°$
$\alpha = 30°$
$\alpha = 60°$
t_{end}= 108.1 Myrs
t_{end}= 5 Myrs
t_{end}= 3 Myrs
Subduction Channel width (w)
$w = 4\ km$
$w = 8\ km$
$w = 12\ km$
t_{end}= 1.5 Myrs
t_{end}= 5 Myrs
t_{end}= 4.5 Myrs
Depth (km)
Distance from trench (km)
Body Rheology
Strong Rheology
Weak Rheology
t_{end}= 5 Myrs
t_{end}= 5.7 Myrs
mm/yr
60
50
40
30
20
10
0

Figure D.2: Flow velocity vector solution for $t = 5$ Myrs for every scenario presented in Table 2-1 and $U = 120\ mm/yr$. The black closed shape represents the ultramafic body position, while each panel represents the single parameter variation indicated above. Black frame is the zoom of the panel, while the red shows a detail of the final position of the body after the last iteration. Below every red panel is also presented the final time achieved (t_{end}) until reaching the top of the subduction channel. All the panels have the same color bar, arrow scales and aspect 1:1